Chair of Materials Physics

Master's Thesis

Additive Manufacturing of Fe-Si Soft Magnets

Robert Strauss, BSc

May 2023

MONTANUNIVERSITÄT LEOBEN
www.unileoben.ac.at

EIDESSTATTLICHE ERKLÄRUNG

Ich erkläre an Eides statt, dass ich diese Arbeit selbständig verfasst, andere als die angegebenen Quellen und Hilfsmittel nicht benutzt, und mich auch sonst keiner unerlaubten Hilfsmittel bedient habe.

Ich erkläre, dass ich die Richtlinien des Senats der Montanuniversität Leoben zu "Gute wissenschaftliche Praxis" gelesen, verstanden und befolgt habe.

Weiters erkläre ich, dass die elektronische und gedruckte Version der eingereichten wissenschaftlichen Abschlussarbeit formal und inhaltlich identisch sind.

Datum 21.05.2023

Unterschrift Verfasser/in
Robert Strauss

Acknowledgments

Zuallererst möchte ich an dieser Stelle meinen Eltern danken, die mich im Laufe meines Lebens ununterbrochen unterstützten und mir somit den Weg in die von mir von klein auf angestrebte Wissenschaft ermöglichten. Auch wenn der Weg vom ersten Spielzeug-Mikroskop zum Diplomingenieur für mich kein leichter war, durfte ich ihn dank ihnen gehen. Auch meinen Geschwistern möchte ich Dank aussprechen, die meine Entscheidung für ein anspruchsvolles Studium an der Montanuni vielleicht nicht immer hundertprozentig nachvollziehen, aber dennoch – so scheint es mir – verstehen konnten.

Für ihre schier unendliche Geduld, ihr Verständnis und das Mitfiebern bei jeder Prüfung, das Mitfreuen, wenn sie gut ausgegangen sind, aber auch das Mitärgern und anschließend nötige erneute Motivieren, wenn der Lernaufwand manchmal nicht ganz das erwünschte Ergebnis brachte, möchte ich mich bei meiner Damaris bedanken, die es vermag, mir auch aus 1000 km Entfernung noch den richtigen Weg zu weisen.

Ein besonderer Dank gehen auch an Univ.-Prof. Dr. Jürgen Eckert, der mein Interesse für die Additive Fertigung durch seine Expertise und fesselnde Vortragsweise geweckt und mich somit zum Verfassen dieser Arbeit bewegt hat, sowie an Dr. Parthiban Ramasamy für sein Vertrauen in meine Arbeit und sein Gespür für einen Plan B. Weiters möchte ich mich herzlich bei allen Kolleg:innen des Erich Schmid Instituts für Materialwissenschaft der Montanuniversität Leoben für ihre tatkräftige Unterstützung und die vielen dringend notwendigen gemeinsamen Tassen Kaffee zum Start in den Tag bedanken.

Zu guter Letzt möchte ich mich ebenfalls bei allen Kolleg:innen der Abteilung „Materialien für die Mikroelektronik“ der Materials Center Leoben Forschung GmbH bedanken, die mir ein erstes „wissenschaftliches Zuhause“ gaben und scheinbar jederzeit wussten, in welche bis dahin ungeahnte Richtung sich mein Wissens- und Interessenshorizont über die Jahre erweitern würde.

„The greatest teacher, failure is.”

- Yoda

Abstract

Over the past decades, in the never-ending endeavour for improved or even newly invented materials, that comply better under the incessantly increasing performance requirements with the big goal of reducing humanity's carbon footprint, the search for equally augmented manufacturing techniques has often led to the field of additive manufacturing. Even though additive manufacturing oftentimes seemed to have been the answer to difficult-to-manufacture components, as of today, it is not the standard method of choice in most fields of work. The production of soft magnetic components, for instance stator parts of electric motors and generators, is no exception in that regard. On the grounds, that the advantage of mass production still predominates the possibility to do so in a more sustainable way by reducing the amount of material needed to manufacture a certain part with as little accompanying waste as possible. Thus, the aim of this thesis was to show the feasibility to additively produce ferritic soft magnetic samples out of ferrosilicon with varying silicon contents. Furthermore, it could be shown that the produced samples yield adequate mechanical properties, comparable to those of current soft magnetic materials used in electric motors and generators. A consistent distribution of Vickers hardness, which was used as the indicator property for their mechanical performance, throughout the samples could be achieved through a methodical parameter study, while using less starting material due to the employed laser powder bed fusion method instead of the now state of the art multi-step process of rolling, stacking, welding and cutting of soft magnetic metal sheets. The magnetic properties were investigated qualitatively, which, in combination with the mechanical testing data, led to a recommendation for possible future process parameter refinements. Additive manufacturing shows promising potential to reduce the initial amount of material that is needed for production and to simultaneously reduce the weight of the finished parts due to the possibility of producing parts that are optimized not only according to the main mechanical loads, but also to the later present operational magnetic flux. Thus, loosely fitting Sullivan's basic maxim of design 'form follows function': form follows flux.

Kurzfassung

In den vergangenen Jahrzenten, auf der schier endlosen Suche nach besseren, oder gar neu entwickelten Werkstoffen, die den steigenden Leistungsansprüchen und der damit verbundenen großen Herausforderung, den CO_2-Fußabdruck der Menschheit zu minimieren, gerecht werden, wurde umfassend an den dazugehörigen modernen Fertigungstechniken geforscht. Additive Fertigung war häufig die Antwort auf die Frage, mit welcher Methode schwierig herzustellende Bauteile gefertigt werden können. Doch auch heutzutage ist Additive Fertigung in den meisten Bereichen nur in Ausnahmefällen die Fertigungstechnik der Wahl. Die Herstellung von weichmagnetischen Bauteilen, die beispielsweise als Statorteile in Elektromotoren und Generatoren zum Einsatz kommen, ist keine Ausnahme. Noch überwiegen die wirtschaftlichen Vorteile der konventionellen Massenproduktion die Vorteile, das für die Fertigung notwendige Ausgangsmaterial, sowie den anfallenden Müll pro Bauteil auf das absolut Notwendige zu senken. Daher war es das Ziel dieser Arbeit zu zeigen, dass es möglich ist, ferritische, weichmagnetische Ferrosilizium-Proben mit unterschiedlichen Siliziumgehalten additiv zu fertigen. Dabei konnte gezeigt werden, dass die mechanischen Eigenschaften der Proben vergleichbar mit jenen von konventionell gefertigten Bauteilen sind. Weiters konnte durch eine methodische Parameterstudie die homogene Verteilung der Vickershärte, welche als Indikatoreigenschaft für mechanische Eigenschaften gewählt wurde, erzielt werden. Die Reduktion des eingesetzten Ausgangsmaterials wurde durch die Herstellung mittels Pulverbettschmelzen anstatt der herkömmlichen mehrstufigen Fertigung durch Walzen, Stapeln, Verschweißen und Stanzen von weichmagnetischen Blechen realisiert. Die magnetischen Eigenschaften wurden qualitativ untersucht und führten in Kombination mit den Daten der mechanischen Prüfung, zu einer Empfehlung für möglicherweise verbesserte Prozessparameter. Die Bauteilfertigung durch Additive Fertigung ermöglicht es, nicht nur eingesetzte Rohstoffe einzusparen, sondern bietet auch großes Potential im Hinblick auf Leichtbau, da zukünftig weichmagnetische Bauteile nicht bloß auf die mechanische Belastung, sondern auch auf den magnetischen Fluss hin optimiert gestaltet und hergestellt werden könnten. Frei nach Sullivans Designleitsatz „Form folgt der Funktion“ ergäbe sich somit: Form folgt dem Fluss.

Content

Abbreviations

Latin Letters

AM	Additive manufacturing
B	Internal magnetic flux
bcc	body-centered cubic
BD	Building direction
BJ	Binder jetting
BMG	Bulk metallic glass
B_s	Saturation flux density
CAD	Computer aided design
CLI	Command line interface
CNC	Computerized numerical control
d	Hatching distance
d_1, d_2	Vickers imprint diagonal length
DED	Directed energy deposition
E	Energy density
E(B)PBF	Electron beam powder bed fusion
EBSD	Electron backscatter diffraction
EDM	Electrical discharge machining
E_{min}	Energy density for minimum porosity
ESI	Erich Schmid Institute of Materials Science
F	Test force
fcc	face-centered cubic

Fe-Si	Ferrosilicon
H	Externally applied magnetic field
H_c	Magnetic coercivity
hcp	hexagonal close-packed
h_{HV}	Mean Vickers imprint diagonal length
HV0.5	Vickers hardness (0.5 kpf)
IPF-Z	Inverse pole figure z-scheme
LIMI	Light microscope
LPBF	Laser powder bed fusion
LT	Longitudinal
M	Magnetization
m_{dry}	Sample weight (dry)
MEX	Material extrusion
MJ	Material jetting
m_{liq}	Sample weight (in liquid)
M_r	Magnetic remanence
M_s	Magnetic saturation
№	Number
P	Laser power
PBF	Powder bed fusion
PPP	Part process parameter
SEM	Scanning electron microscope
SLH	Sheet lamination
SMC	Soft magnetic composite

STL	Stereolithography
t	Powder layer height
T_C	Curie temperature
T_m	Melting point
T_N	Néel temperature
TV	Transversal
v	Scanning speed
VPP	Vat photopolymerization

Greek Letters

ρ_{bulk}	Bulk density
ρ_{liq}	Liquid density
μ	Permeability
μ_0	Permeability of free space
μ_{Fe}	Permeability of pure iron
Π	Porosity
ρ	Sample density
χ	Susceptibility
θ	Vickers indenter tip angle

1. Introduction

Based on their magnetic behaviour, ferromagnetic materials such as iron, nickel, cobalt (and their alloys) and ferrimagnetic materials such as magnetite can be distinguished as either magnetically soft or hard [1]. Hard magnetic materials or permanent magnets remain magnetized after an applied magnetic field, that led to magnetic saturation, is removed. Soft magnetic materials, however, are easily magnetized and demagnetized by changing the imposed magnetic field. The latter magnets also promptly lose their magnetization as soon as an applied field is removed [2]. These properties make soft magnets ideal for the application in quickly changing magnetic fields, from the generation and conversion to the usage of electric power in generators, transformers, and electric motors, respectively [3]. The reduction of power losses and the subsequent rise of efficiency throughout these processes has been a major and steady engineering and scientific goal for many years and has become even more important with the continuous increase in electrification in many areas of our daily lives. The transition from few, but massive applications – e.g. generators in hydroelectric power plants – to many smaller and decentralized ones – e.g. electric bicycles – also presents itself with accompanying challenges. While some decades ago, the power generation in a western industrialized setting was almost exclusively done by big power plants, as an example, nowadays more and more private homes are equipped with photovoltaic systems that either provide power directly as a so-called isolated operation mode, feed the public power grid or represent a combination of both modalities. In the two decades from 1999 to 2019 the amount of both, grid-connected and isolated operation mode photovoltaic devices in Austria grew by a factor of 774 to 1,694 MW and by a factor of 5.5 to 7.7 MW, respectively [4]. The direct current provided by all these solar cells needs to be converted and transformed by use of photovoltaic inverters. These inverters are an integral part of solar power generation systems and one of the many applications of soft magnets in the field of power generation and conversion. An improvement in efficiency of electric components that require soft magnets to operate may be achieved by addressing as many bottle necks as possible. In the case of solar power systems this is primarily done by thorough research efforts of all semiconductor elements. While the focus on the most

obvious challenge is understandable – be it higher power output per square meter of solar cells or increased load capacity and shorter loading times of electric vehicles batteries – other, accompanying issues often get overlooked. Next to the power production and conversion, as described exemplary with photovoltaic systems, the power consumption, for instance by electric vehicles also increased sharply since their widespread availability. In the years from 2001 to 2021 the amount of officially registered electric cars (excluding hybrid cars) in Austria rose by a factor of 500 from 153 to more than 76,500 cars [5]. The fact that there are several electric motors in every electric vehicle, further increases the pressure in the search for power trains with higher efficiency. One possible solution to achieve this, is to shift from conventionally manufactured and rather bulky components to ones that are geometry-wise optimized with the help of modern simulation software and present magnetic fluxes as well as major mechanical loads in mind. These improved pieces usually are no longer economically manufacturable with regular processes and thus present a potential use case for additive manufacturing (AM), which also offers the possibility to selectively choose magnetically hard or soft directions, that, respectively, require a higher or smaller amount of energy to be (de)magnetized [6].

2. Theoretical Background

Conventionally manufactured soft magnetic materials – oftentimes iron-silicon alloys – have been seemingly brought to their performance limits, e.g. by lowering the grain size down into the range of magnetic domains [6]. Alternatively, a new class of materials, soft magnetic composites (SMC), that are manufactured by powder metallurgy processes, has been introduced. These SMC materials usually consist of ferromagnetic powder particulates with an electrically insulating shell and therefore show inherently small grain sizes. Albeit being a step in the right direction, SMC still show magnetocrystalline anisotropy with certain crystallographic axes requiring applied fields of higher energy to align while also constricting the freedom of design due to the nature of powder metallurgic manufacturing.

2.1. Ferrosilicon

Ferrosilicon (Fe-Si) represents a range of iron-based alloys with varying amounts of the eponymous silicon, as well as potentially other alloying elements, and is oftentimes named “electrical steel” although there is no carbon added due to the deteriorating effect carbides, and oxides in that matter, have on the material’s magnetic behaviour [7]. The contents of the ferrite-stabilizing element Si in these electrical steels may be as high as 6.45 wt% (12.5 at%), yet usually range around 3.3 wt% (6.25 at%), which – as can be seen in the phase diagram (figure 1) – places these alloys in the body-centered cubic (bcc) α-phase and face-centered cubic (fcc) γ-phase, respectively, as well as the so-called “gamma-loop” α-γ two-phase region between the two corresponding phase boundaries of 1.63 wt% and 1.94 wt% Si [8, 9]. Although alloys with higher Si-contents tend to comply more with the desired requirements, such as high magnetic saturation and electrical resistivity, the substantial embrittlement, which is caused by adding Si atoms and the resulting distortion of the surrounding Fe lattice, widely prevented these ferrosilicon steels from being used commercially. Therefore, the occurring micro- and subsequent macro cracking during the rolling processes that are traditionally employed to reach the required individual sheet thicknesses of less than 500 µm highly limited the

use of electrical steels to Si-contents at around 3.3 wt% [10]. However, this challenge of embrittlement, might also be one steppingstone for the use of additive manufacturing in the production of high Si-content ferrosilicon parts, since there are purely thermal loads present during the manufacturing of such components, which may be precisely regulated and adapted to each alloy composition.

Additionally, there has been some research on Fe-Si with even higher Si-contents up to the stochiometric composition of 21.6 wt% (50 at%) Si. These alloys already show, as may be expected due to the high Si content, semiconductor-properties and therefore are not used as ferromagnetic materials but as narrow gap semiconductors in thermoelectric applications or, disregarding its magnetic or electrical properties entirely, as alloying and deoxidizing components in the steel industry. [8, 11]

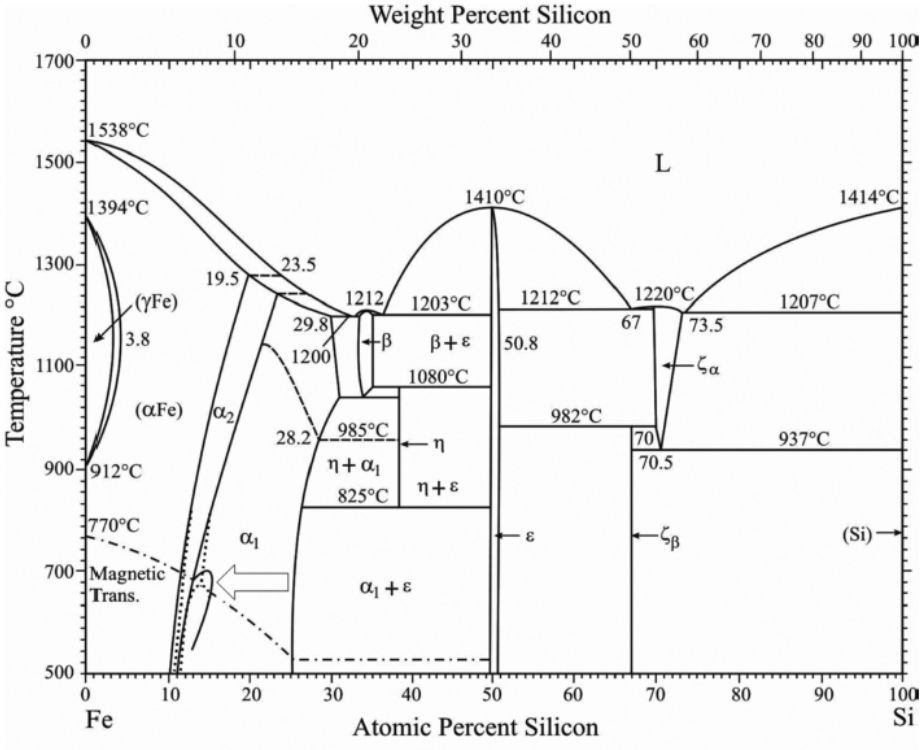

Figure 1: Phase diagram of iron and silicon [8].

2.2. Magnetism

Albeit not understood, the phenomenon of magnetism was already known by the people in Mesopotamia as well as ancient Greece and China and could and still can be found in rock formations that were hit by lightning strikes or in the remnants of iron-rich meteorites. The remarkable property of – depending on the positioning of two such magnets – attraction or repulsion was seen as magical or even as the “material’s soul”. Over time, magnetic materials have been used for millennia in tricks, as navigational devices and finally in energy production and conversion and many more applications of our daily lives. [2]

Fundamentally, five different kinds of magnetism, diamagnetism, (ideal) paramagnetism, ferromagnetism, antiferromagnetism and ferrimagnetism, are to be distinguished in the following sub-chapters. Since they are usually found in modern applications, a brief explanation of these types ought to be sufficient to understand the principals of magnetism. Hurd even described a total of 14 different types and specific subtypes of magnetism in 1982 [12].

2.2.1. Diamagnetism

Diamagnetic materials exhibit opposingly oriented magnetic fields in case they are exposed to external ones. This phenomenon occurs due to the induction of an electrical current, which is caused by the application of an external magnetic field, in the atom’s electron shells and the – according to Lenz’s law – accompanying inversely oriented magnetic field. Therefore, ideal diamagnetism has also been referred to as “noncooperative magnetism”. Copper (Cu) or sodium chloride (NaCl) are examples for diamagnetic solids. [6, 12]

2.2.2. Paramagnetism

Paramagnetic materials consist of atoms or ions with magnetic dipole moments, which are – in the case of ideal paramagnets – randomly oriented, isolated from each other and therefore show no interdependence at “high” thermal energies, i.e. usually at non-cryogenic temperatures. These magnetic moments, also called orientations, align with an imposed field, and thus enhance the magnetic field inside the material. Because of

the energetic non-equilibrium nature of the aligned magnetic moments, the induced magnetic field collapses as soon as the externally imposed one is removed. Examples for paramagnets are magnesium (Mg) or aluminium (Al). [12, 13]

2.2.3. Ferromagnetism

In ferromagnetic materials, magnetic dipoles tend to align locally and consequently create small volumes with the same magnetic orientation (figure 2). These volumes form when magnetic moments align on an atomic scale due to the exchange interaction of neighbouring spins, and are fittingly called magnetic domains, reduce the material's total magnetostatic energy [14]. These domains, usually in the range of about ten nanometers to tens of micrometers, are separated by roughly 10 µm thick domain walls – also called Bloch walls – in which the magnetic orientation incrementally shifts from one domain's to the other's, as can be seen in figure 3.

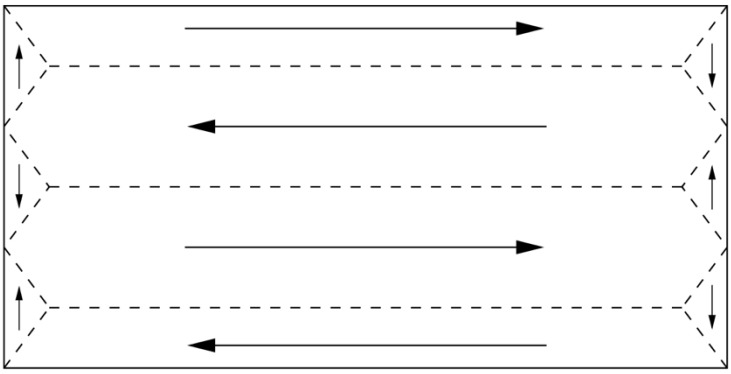

Figure 2: Schematic depiction of magnetic domains and their orientation, as well as domain walls (dashed lines) in a material [6].

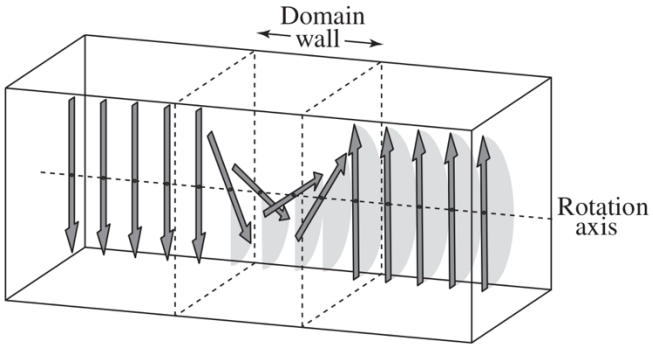

Figure 3: Illustration of two bordering domain fragments and their dividing domain wall. Since the magnetization just needs to be rotated along one axis, this is a so-called twist boundary [6].

Due to these domains being statistically distributed throughout the material, the magnetic dipole moments cancel each other out and therefore ferromagnets seem inherently non-magnetic until an external magnetic field is applied. Yet, although their directions are mostly randomly oriented, there are magnetic easy axes that correspond to certain crystallographic directions – in many cases with small miller indices [15, 16]. The magnetically easy axes for pure bcc iron and hexagonal close-packed (hcp) cobalt, for instance, are the <100> and <0001> directions, respectively are directions in which there is less energy needed to reach magnetic saturation compared to others. Although there is no general correlation between the atomic packing factor along one direction and the ease of magnetization in this specific direction, the simple assumption that, due to the higher number of atoms that need to be affected, close-packed directions are harder to (de)magnetize holds true for bcc iron. This can be seen schematically in figure 4, as its close-packed body diagonals, which correspond to the bcc unit cell's <111> directions, are the magnetically hard axes for Fe. However, this is not the case for fcc nickel, which further demonstrates the complex nature of magnetic properties. [6, 17]

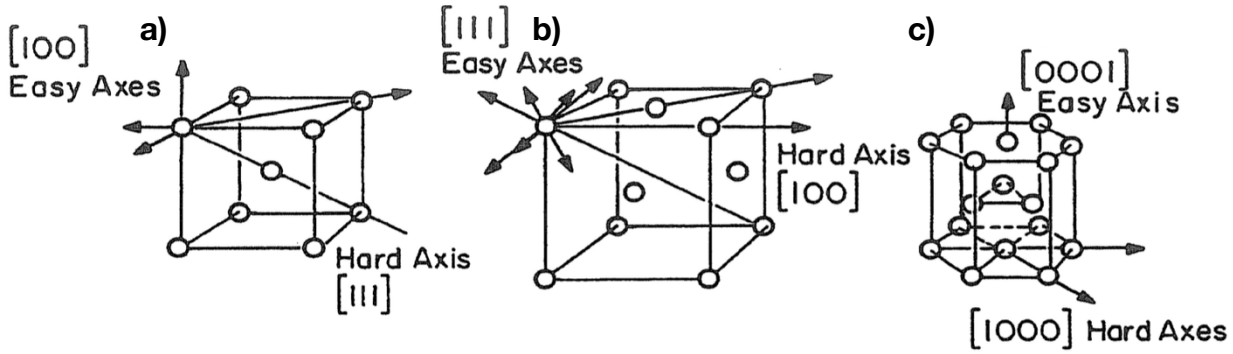

Figure 4: Schematic of magnetically easy and hard axes in **a)** bcc, **b)** fcc and **c)** hcp materials [17].

Thus, an imposed field forces the domains to align accordingly in a stepwise manner: At first, those domains with magnetic orientations and with magnetic easy axis close to the applied field direction start to grow by Bloch wall movement, while differently oriented ones shrink. This process continues as the applied field is increased and results in fully reversible magnetization until the domain walls intersect and get pinned by material imperfections, such as dislocations or grain boundaries. The release from this fixed state requires additional energy, which has to be supplied by an increasing external magnetic

field. As the domain growth process advances, the growing, advantageously directed domains seem to consume adversely oriented ones until one single domain, that points in the external field's direction, is left (figure 5).

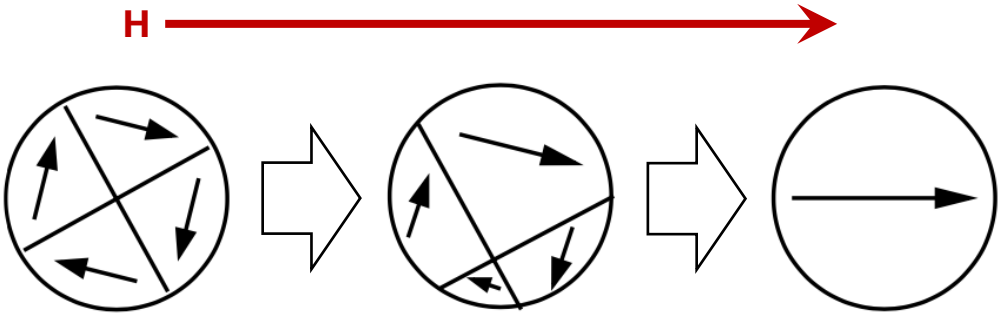

Figure 5: Schematic magnetization process. Domain growth occurs due to the domain wall movement enforced by an external magnetic field [6].

Thus, the material is magnetized and largely stays that way even after the applied field has been removed. Since the movement of Bloch walls requires, compared to the alignment of magnetic dipole moments, the majority of energy in the magnetization process, the magnetization decreases marginally to the point, where forced domain wall movement would again be necessary to demagnetize an already magnetized sample. Alternatively, the required energy may also be provided in the form of heat: Above the so-called Curie temperature (T_C), where the ordering of magnetic dipole moments breaks down, domains cease to exist, and the material becomes paramagnetic until its temperature falls again under this material-specific temperature (e.g. the T_C of iron and cobalt are 770 °C and 1120 °C, respectively [18, 19]). After cooling down, the material's ferromagnetic nature has been restored and its magnetic domains are – as long as there is no external magnetic field imposed – once again randomly oriented [6, 12].

As a consequence of the dimensions of domains and Bloch walls, materials with either larger grain sizes and therefore less grain boundaries, or nanocrystalline materials with grain sizes of less than 100 nm, thus being in the range of magnetic domains, are generally easier to be magnetically cycled [6]. Examples for ferromagnetic materials include cobalt (Co), nickel (Ni) and – of course – iron [17].

2.2.4. Antiferromagnetism

While magnetic dipole moments in ferromagnetic tend to align parallel – also called cooperatively – to each other and thus enhance an applied magnetic field's affects, an inverse process happens in antiferromagnets. Here, neighbouring magnetic moments arrange in an antiparallel, uncooperative, almost chessboard-like way, in which every other magnetic ion is oriented in one and each directly adjacent one is oriented in the opposite direction, which leads to paramagnetic-like behaviour of these materials, i.e. there is no magnetization present and they do not enhance or concentrate external magnetic fields. Analogous to the magnetic properties in ferromagnets, anti-ferromagnetic properties are also temperature dependent. Here, the material-specific temperature, above which the magnetic ordering of dipoles breaks down is called Néel temperature (T_N) or ordering temperature instead of Curie temperature, as is the case in ferromagnets. Below T_N, the different "atomic chessboard-tiles" – also called sublattices – spontaneously arrange in the energetically most efficient way without the effect of externally imposed magnetic fields. [6]

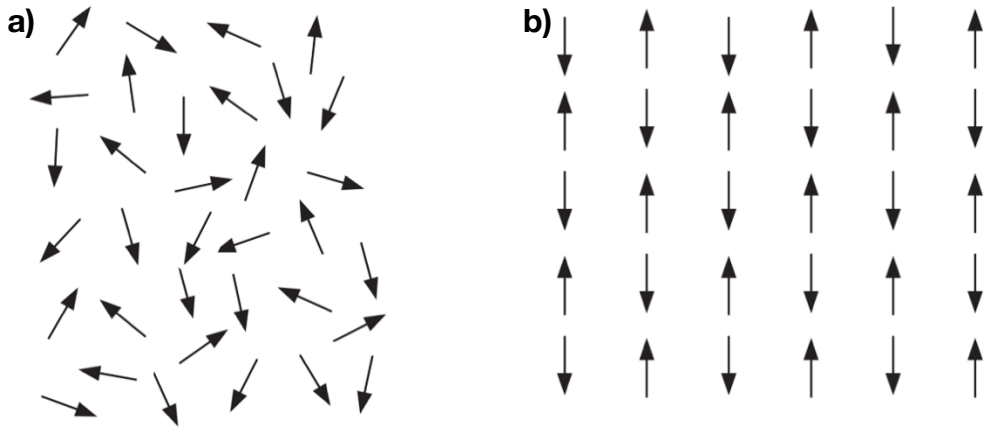

Figure 6: Schematic of an antiferromagnetic material **a)** above and **b)** below its Néel temperature [6].

However, a magnetic field oriented in one of these spontaneously defined orientations enhances this direction's magnetization and thus a net magnetization in this very direction remains after the field has been turned off. Meanwhile, the opposingly oriented magnetization decreases by the amount of the former's increase. Alternatively, if the imposed magnetic field is perpendicular to the magnetization directions, the thusly enforced rotation of magnetic dipole moments creates in turn a molecular magnetic field

which is opposingly oriented to the applied field. In an ideal case, the imposed external and resulting internal fields fully annul each other and therefore the magnetic orientations stay perpendicular to the external field [6]. Examples for antiferromagnetic materials include hematite (α-Fe_2O_3) and cobalt oxide (CoO) with Néel temperatures of -178 °C and 18 °C, respectively [20].

2.2.5. Ferrimagnetism

Somewhat relevant to both, ferromagnets and antiferromagnets, ferrimagnetic materials are magnetized below their Curie temperature – even without any externally applied field present. The antiferromagnetic quality of uncooperative, i.e. antiparallel, ordering of neighbouring magnetic dipole moments of unequal magnitudes, however, leads to a fundamentally different magnetization-demagnetization behaviour than in (anti)ferromagnets: In ferrimagnetic materials, the magnetization in one direction is weaker than the adversely oriented one (figure 7). Thus, both magnetic dipole moments do not fully cancel each other out and therefore these materials show an overall magnetization with one preferred direction [6].

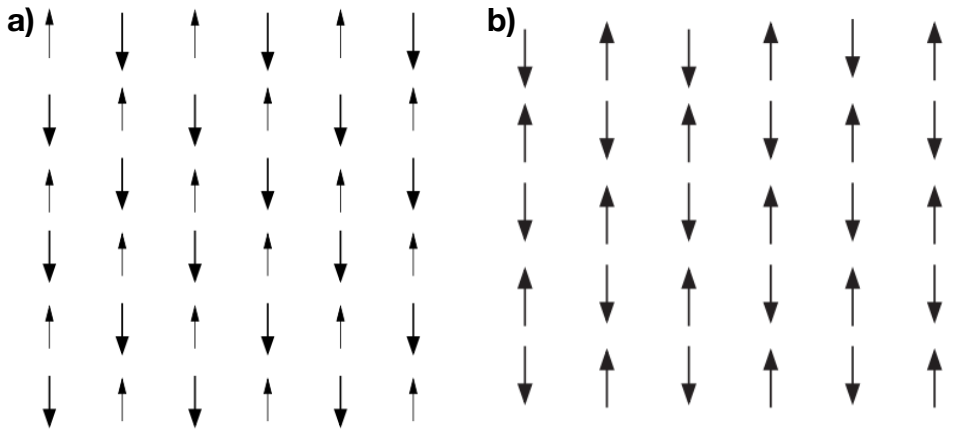

Figure 7: Comparative schematic of a **a)** ferrimagnetic and an **b)** antiferromagnetic material's magnetization behaviour [6].

As ferrimagnets are, as is the case with many antiferromagnets and contrary to ferromagnets, ionic solids, they are electrically insulating magnets. Thus, while it is possible to magnetically cycle ferrimagnets, unwanted eddy currents are suppressed due to their high electric resistance. This specific combination of properties is for instance

exploited in electrical high frequency applications where these eddy currents lead to unwanted energy losses due to heat dissipation. Well known representatives for ferrimagnets are magnetite (Fe_3O_4) or manganese ferrite ($MnFe_2O_4$) and are, in general, made up of iron, oxygen and other metallic elements (Me) in the form of $MeFe_xO_y$ [6, 21]. Due to them consisting of two opposing magnetic dipole moments, ferrimagnets show similarities to antiferromagnets on a microscopic-, as well as ferromagnets on a macroscopic scale with a directionally dependent non-zero net magnetization and a related hysteresis behaviour [6].

2.2.6. Magnetic Hysteresis Behaviour

As previously described, one major feature of ferromagnetic materials is their capability to stay magnetized after an externally applied magnetic field has been removed. This trait, in turn, indicates that, in order to reverse the magnetization's direction as well as to entirely demagnetize a sample, additional energy needs to be provided by a then adversely oriented external magnetic field. Thus, the plotting of a ferromagnetic material's magnetization (M) and following demagnetization as a function of an externally applied magnetic field (H) leads to a hysteresis loop. This prominent curve often serves as a basis for the magnetic characterization of a material due to the fact that its inscribed area represents the dissipated energy that shows as heat during the magnetization and subsequent demagnetization of a certain volume of material. Since – per definition – soft magnetic materials are easier to be magnetized and demagnetized, i.e. magnetically cycled, smaller relative hysteresis loop areas are representative indicators for this class of magnets [1]. These narrow hysteresis loops are notably defined by their small magnetic coercivity (H_c), the magnetic field needed to fully demagnetize a material, and by their remanent magnetization (M_r), the remaining internal magnetization after an external field has been removed. Hard magnetic materials, in contrast, show, as can be seen when comparing the red (hard magnetic) and blue (soft magnetic) magnetization curves (M-H-curve) in figure 8, a characteristically broad hysteresis loop that represents the larger amount of energy needed to change its magnetic field [2].

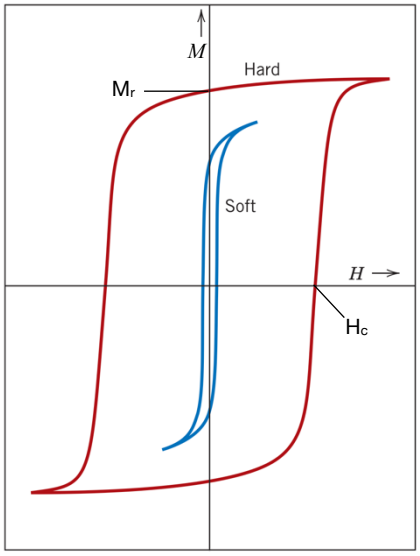

Figure 8: Schematic hysteresis loops of soft (blue) and hard (red) magnetic materials [1].

In addition to the aforementioned parameters, the permeability (μ) – the ability of materials to be permeated by an external magnetic field – and the susceptibility (χ) – an indicator for the intensity of a material's response to magnetic fields – represent further important measures of a material's magnetization. As can be seen in equation 1 and equation 2, respectively, μ (H/m) is the ratio of magnetic induction, i.e. the magnetic flux inside a material (B) and magnetizing field, whereas the dimensionless χ is the ratio of M and H. To set this into perspective, materials with higher permeabilities concentrate higher amounts of magnetic flux inside of them, i.e. they "conduct" magnetic fields better than materials with low μ. [6]

$$\mu = \frac{B}{H} \quad \left[\frac{H}{m}\right] \tag{1}$$

$$\chi = \frac{M}{H} \quad [-] \tag{2}$$

Equation 1 also defines μ as the slope of any given magnetization curve. Since these curves do not show linear dependency for the case of ferro- or ferrimagnetic materials, μ usually is a differential value, and only reaches material-specific values as magnetic saturation is reached. The material's resulting saturation flux density (B_s) represents the flux where all domains are fully aligned with the externally applied field and is ideally relatively high, i.e. larger than 1.2 T, for soft magnetic materials. The relationship between

the three values B, H and M can be expressed, as is shown in equation 3, through the introduction of the magnetic permeability of free space (μ_0), i.e. μ in vacuum, with the value of $4\pi \cdot 10^{-7}$ (N/A^2). [6]

$$B = \mu_0 \cdot (H + M) \quad [T] \tag{3}$$

Due to the material-specific behaviour in external magnetic fields, it is possible – as can be seen in figure 9 – to distinguish the type of magnetism present in a sample as well as its magnetic hardness by observing its respective hysteresis loop and permeability [22].

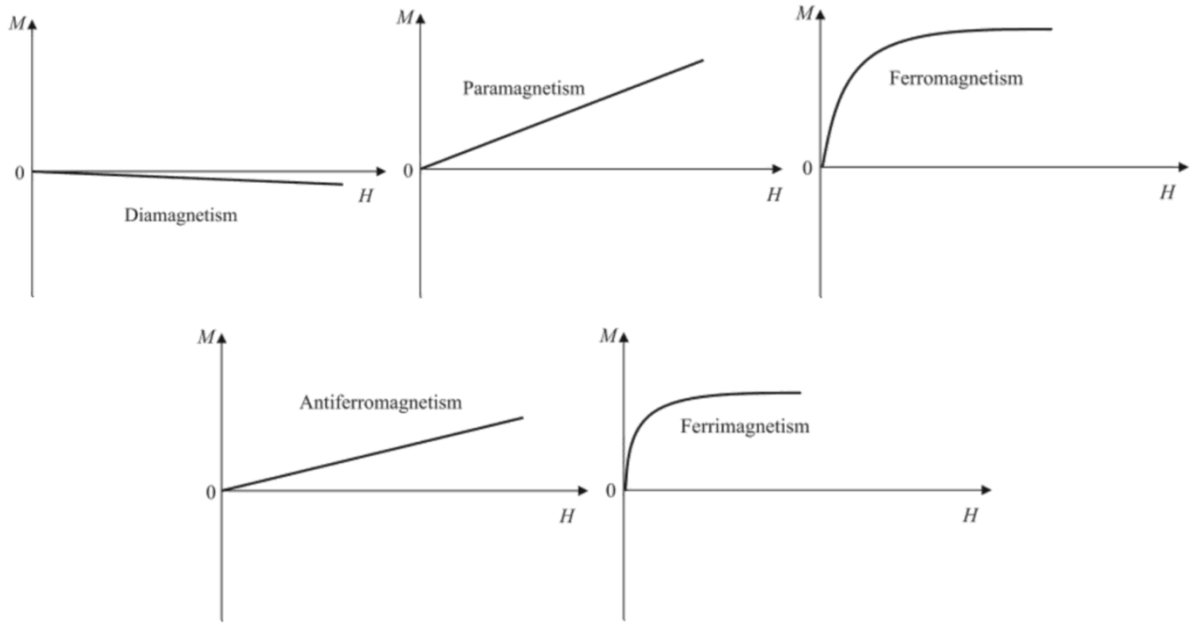

Figure 9: Comparison of the five main types of magnetism's magnetization and applied magnetic field (M-H) diagrams. Pictured are resulting magnetizations due to positive external fields [22].

A short selection of commonly used metals and alloys and their respective coercivities, permeabilities and susceptibilities, sorted by decreasing χ, also expressed by the ratio of each material's μ and the permeability of 99.9 % pure iron (μ_{Fe}), can be found in the following table 1. Since air is a common "magnetic resistance" in many real-life applications, the values for air at normal temperature and pressure, 20 °C and 1 atm, respectively, can also be found in this table.

Table 1: List of metals, their respective permeabilities and susceptibilities.

Material	H_c [A/m]	μ [H/m]	$μ/μ_{Fe}$ [‰]	χ [-]	References
Iron (99.9% pure)	0.8	$4.4•10^{-1}$	1000	$3.5•10^{5}$	[23]
Ferrite (FeSi3.0)	12.0	$5.0•10^{-2}$	114.24	$4.0•10^{4}$	
Steel (Fe0.1C0.1Si0.4Mn)	200.0	$1.4•10^{-3}$	3.14	$1.1•10^{3}$	
Nickel	55.7	$7.5•10^{-4}$	1.71	$6.0•10^{2}$	[24, 25]
Air (20 °C, 1 atm)	-	$4.5•10^{-1}$	0.003	$3.7•10^{-7}$	[24]
Copper	-	$1.3•10^{-6}$	0.003	$-9.6•10^{-6}$	

These material's differing characteristics, e.g. the vastly differing μ values – $μ/μ_{Fe}$ is listed in per thousand (‰) – impressively back the forementioned fact, that different materials may easily be differentiated by their magnetic behaviour.

2.3. Powder Bed Fusion

Powder bed fusion (PBF) is, along with binder jetting (BJ), directed energy deposition (DED), material extrusion (MEX), material jetting (MJ), sheet lamination (SHL) and vat photopolymerization (VPP), one of the seven basic processes in additive manufacturing as defined by the DIN EN ISO/ASTM standard 52900 [26]. While also used with other materials, PBF is mainly used in the field of additive manufacturing of metals with many (industry) end-user friendly machines, specifically made powders and accompanying material-distinct process parameters available on the market [27].

2.3.1. Metal Powders

One of the key parameters in PBF can be attributed to the metal powder's properties such as (apparent) density, particle size distribution, particle form factor, humidity and chemical composition have a major influence on the process and therefore the final product. Some of these parameters are interdependent, since the powder's apparent density depends not only on the chemical composition, but also on the particle's sizes and shapes. Because of their outstanding flowability in comparison with irregularly or acicularly shaped powder particles, spherical particles (figure 10) are generally

considered ideal for any powder bed-based manufacturing process. However, narrow particle size distributions might be adversely influencing the apparent density, since the gaps between individual particles that can only be filled by smaller ones. Commercially available powder's particle sizes are – depending on the manufacturing process – usually in the range of 20 to 63 or 45 to 105 micrometers, respectively [28]. Too high amounts of smaller particles, however, affect the powder's flowability disadvantageously, therefore extended research has already been conducted in this area [29, 30].

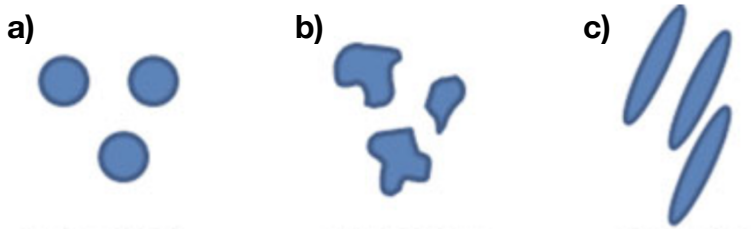

Figure 10: Different powder shapes: **a)** Spherical, **b)** Irregular, **c)** Acicular [28].

In addition to the general form factor, particles might have smaller particles attached to them. These appendices, so-called "satellites", form during the powderization process, when two or more particles are still molten and in stay contact with each other until they are (partially) solidified. For the sake of good flowability, the number of satellites should, in general, be as low as possible [31]. Details of the complex processes happening during the powderization of different materials, however, surpass the scope of this work. Next to the particle shape, humidity also plays a crucial role in the flowability of metal powders. Due to their small sizes and thus large surface areas, particles tend to agglomerate and oxidize quickly. Hence, the limitation of water content in the powder bulk, as well as the build chamber during the manufacturing process is imperative [28].

2.3.2. Preprocessing

As extensive preliminary work needs to be done before any object may be manufactured additively, PBF is no exception. These preprocessing steps may be separated into digital and physical aspects: The former ones include the digital creation of a desired product using computer aided design (CAD) software and a fundamental knowledge of the process, its possibilities and limitations. Additionally, the CAD model needs to be sliced into layers of distinct heights (t), which have to be vectorized and have hatching parameters assigned to them for the AM machine to be able to subsequently create the physical model in a layer-wise fashion. These hatching parameters include most importantly the pattern, the laser is creating during the scanning phase of a specific layer's infill, the hatching distance, i.e. the gap between two neighbouring tracks, and the angle increment, two consecutive layer's hatching inscribe relatively to each other. The latter preprocessing aspects include the AM machine hardware, as well as the material itself, i.e. the powderization and classification of the resulting powders' particle size distribution, particle morphology and chemical composition, any possibly necessary mixing of powders to create alloys and the AM machine's safety equipment. [31, 32]

2.3.3. PBF Manufacturing Process

In this technique, a powerful heat source – usually a laser beam or an electron beam – is moved over a previously carefully spread layer of material powder along a predefined path to locally melt and therefore fuses this track with the adjacent and/or previously molten material. Depending on the heat source used, the process is called laser powder bed fusion (LPBF) or electron beam powder bed fusion (EB-PBF or EPBF), respectively. While in LPBF, the laser beam's position and focus are controlled by a combination of mirrors and optical lenses, the electron beam used in EPBF is regulated by magnetic focusing and deflection lenses. After each scanning step, the next – in the range of tens of micrometers – thin powder layer is applied uniformly and the following layer can be scanned, thus creating the desired product geometry in a layer-by-layer-wise fashion. This fundamental principal defines the height, i.e. the direction in which the powder layers are added, as the building direction (BD). To achieve this, the build chamber, which can be de- and increased in volume by raising or lowering its base plates, also called build

platform, according to the defined layer thickness. Analogous to the build chamber, the feed region, or supply chamber, where neat powder is stored until it is distributed in the build chamber by a so-called recoater, a brush, blade, or roller, is also able to vary its volume via its height. These steps are repeated until the final part has been completed and can be removed from the machine. Any surplus powder, that might not be needed for the even distribution of a layer, is collected in an overflow region – usually a simple container that can easily be accessed from outside the hermetically sealed production chamber for the powder to be retrieved and reused in future productions. An exemplary schematic of the PBF process's main features is shown in figure 11. [31]

Because of their high surface area and the resulting tendency of metal powders to form – especially at high temperatures like in PBF – embrittling oxides, LPBF processes need to be performed – depending on the material – in dry atmospheres and at very low oxygen (O_2) concentrations of a few hundred ppm or less. These low O_2 levels are generally achieved by a combined approach of an applied vacuum and subsequent flushing and filling with inert gas, i.e. argon (Ar), helium (He) or a combination of both. In the case of EPBF, however, the very nature of the process requires a high vacuum for the electron beam to be sufficiently precise, otherwise the electrons would be scattered by any gas atoms present in the build chamber. [31]

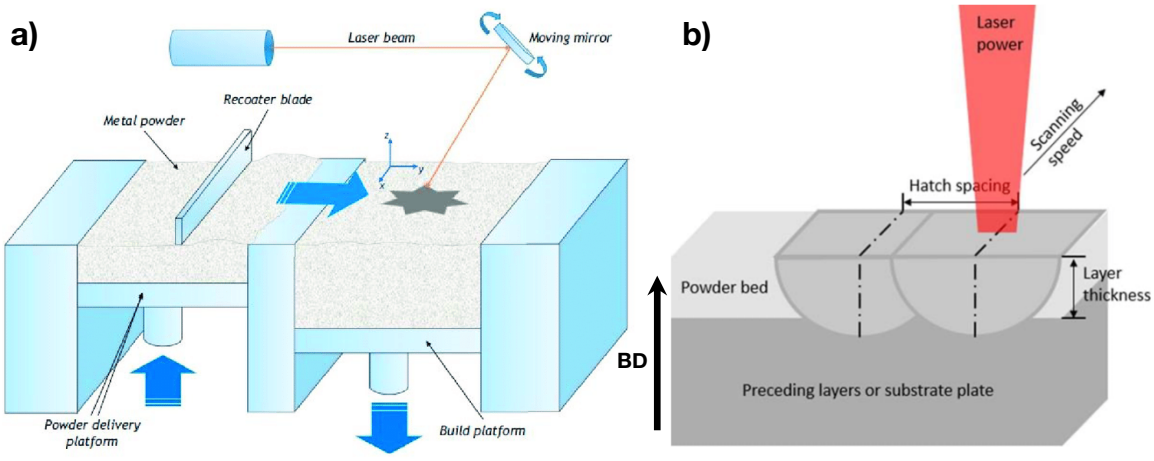

Figure 11: The laser powder bed fusion process **a)** schematically and **b)** in more detail [33, 34].

The scanning strategy plays – in addition to the already mentioned selection of important process parameters – a crucial role in all AM processes. Extensive studies have been undertaken to find the ideal strategy für a specific process-material-combinations, which,

as a common denominator, usually start with a simple stripe or meander hatch pattern as a baseline [35, 36]. Schematically depicted in figure 12 are the four most commonly used scanning strategies: Stripes with and without contour, meander-, and checkerboard-style. To prevent uneven heat distribution and subsequent residual stresses, which may lead to warping or even cracking, due to scanning the same coordinates every other layer in the same way, it is customary to rotate the scanning direction by an incremental angle relative to the previously exposed layer's direction [37]. These incremental angles are usually odd with 45 ° and 67 ° being widely used [35]. Aside from highly ordered scan strategies, an interesting approach to avoid residual stresses in the finishes part is the employment of randomized spot strategies with appropriate boundary conditions in place, which spot-melt every allowed coordinate point with the same probability. However, advanced scan strategies like this are not widely used and usually require – if possible, with the machine at hand – extensive manual programming by the user, since commonly available AM machines generally offer a fixed set of scanning strategies to choose from. Since inertia, associated with the movement of mirrors required for the beam control in LPBF, has to be considered, EPBF offers, in general, a wider range of sensibly implementable scan strategies [38].

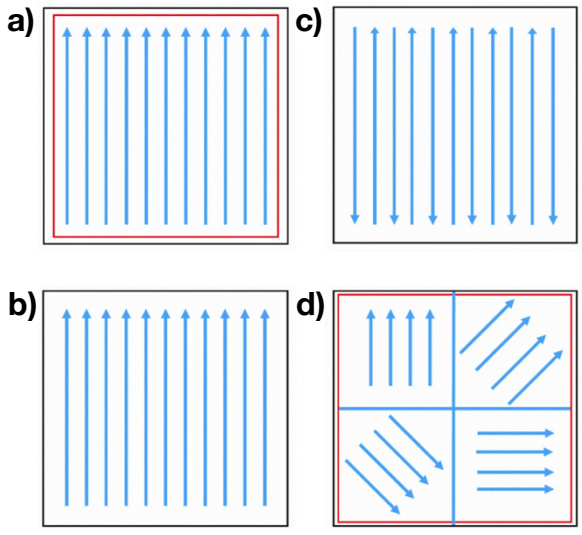

Figure 12: Four commonly used hatching strategies: **a)** Stripes with contour, **b)** Stripes without contour, **c)** Meander-style and **d)** Checkerboard-style [35].

2.3.4. Combining Process Parameters

To make complex and multi-parametric processes, such as LPBF, comparable, the introduction of factors that combine many of the most critical influences, is a logical step. In energy-beam controlled AM processes, this factor has been defined as the volumetric or surface energy density, with the former one being more widely used in LPBF [31, 39]. This volumetric energy density, E (J/mm^3) combines the laser power, P (W), scanning speed, v (mm/s), hatching distance, d (mm) as well as layer thickness, t (mm) into one parameter, as can be seen in equation 4 [31].

$$E = \frac{P}{v \cdot d \cdot t} \quad \left[\frac{J}{mm^3}\right] \tag{4}$$

Despite this equation's practicability and descriptiveness, the limited number of factors taken into account by it, disregards substantial aspects of the complexity in LPBF, as it largely ignores the influence of the chosen hatching pattern as well as the material's absorption rate, heat capacity, conductivity and their influence on the residual heat present during the exposure of overlying powder layers. The consideration of these – and more – factors, however, leads to lengthy and complex equations, that are more widely used in simulations of thermal processes in PBF and therefore counteracts the attempt to join most of the important parameters into one simplified and easily comparable factor, such as the energy density. [40]

2.3.5. Postprocessing

Additive manufacturing requires, as is the case with most conventional manufacturing processes, and contrary to the oftentimes proclaimed quick and easy way to final products, process-dependent postprocessing. In the case of PBF of metals, this includes not only the separation of products and base plate, but also the non-trivial removal of any support structures, as well as potential heat treatments, e.g. for stress relief or surface hardening purposes, or conventional finishing techniques, such as milling (figure 13) or sandblasting, should the AM-specific step-like surface quality not be desired in the final product. [31]

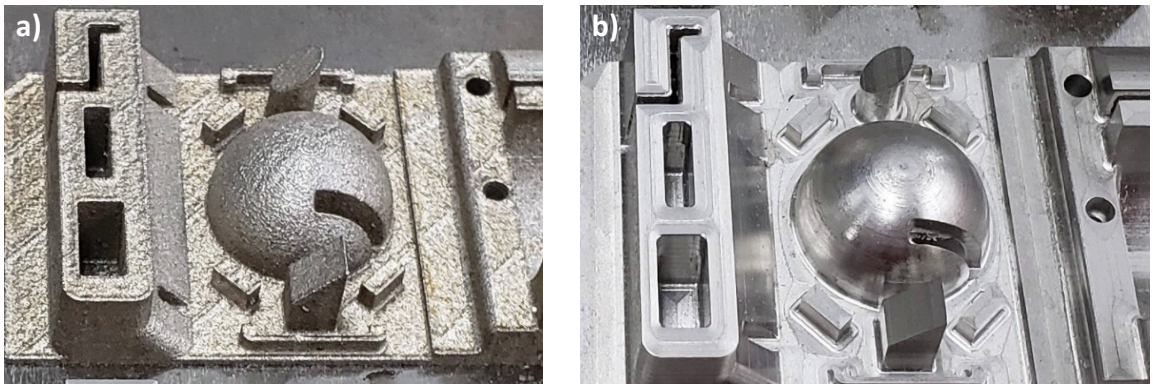

Figure 13: Additively manufactured mold **a)** before and **b)** after postprocessing (CNC milling) [41].

In the case of magnetic applications, postprocessing might also include any required magnetization as previously described in chapter 2.2.3., as well as – depending on the operation criticality of any occurring eddy losses – precise machining, e.g. to reduce air gaps between rotors and stators in generators and electric motors as well as possible. These gaps are volumes of decreased permeability, and therefore act as “magnetic resistors” with accompanying increased losses (figure 14) [42].

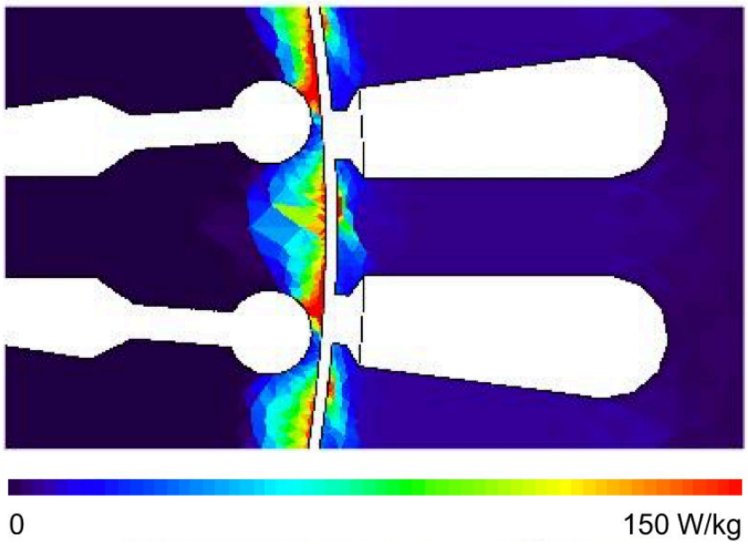

Figure 14: Simulated magnetic losses in an electric motor’s air gap between rotor (left part) and stator (right part) [42].

3. Materials and Experiments

Since this thesis ought to cover many of the key steps to the production and testing of additively manufactured Fe-Si soft magnets, the following experiments and methods were conducted and used to give an as comprehensive insight as possible into the most process-critical parameters.

3.1. Powders

As a basis for all experiments, pre-sieved and classified Fe- and- Si-powders of 99.75 % and > 99.95 % purity, respectively, and particle sizes between 15 and 53 micrometers, were procured from Testbourne Ltd in Hampshire, Unites Kingdom. The sieving of both powders was performed by the manufacturing company and, apart from the certification of particle size range (15-53 µm), no size distribution data could be obtained from them. Thus, both powder's morphologies and particle size distributions were investigated using scanning electron microscopy (SEM) and light microscopy (LIMI) with a TESCAN MAGNA and an Olympus BX51, respectively, in combination with the open-source image processing software ImageJ [43].

3.2. Powder Mixing

Two obtain two different Fe-Si alloys, "FeSi1.5wt%" and "FeSi3.5wt%", respectively consisting of 98.5 wt% Fe with 1.5 wt% Si added and 96.5 wt% Fe with 3.5 wt% Si added, the corresponding powders were weighed according to the calculated masses (table 2) and mixed with a drum hoop mixer JEL RRM Mini-II by J. Engelsmann AG (figure 15) for four hours at 40 rpm without the addition of mixing additives in ambient atmosphere (FeSi1.5wt%: 21.5 °C and 36 % relative air humidity; FeSi3.5wt%: 22.0 °C and 28 % relative air humidity). However, since both powder mixtures were stored for one week, their humidity contents are to be seen as equal, thus eliminating this possibly process influencing parameter.

Figure 15: Drum hoop mixer JEL RRM Mini-II by J. Engelsmann AG used for powder mixing.

Table 2: Fe- and Si-contents and corresponding weighed masses for FeSi1.5wt% and FeSi3.5wt%.

Alloy	Fe [wt%]	Fe [g]	Si [wt%]	Si [g]	Total mass [g]
FeSi1.5wt%	98.50	492.50	1.50	7.50	500
FeSi3.5wt%	96.50	482.50	3.50	17.50	500

To ensure both powders to be sufficiently blended, an additional SEM sample was prepared from FeSi3.5wt% and investigated. Following this step, silica gel pouches were added into both mixture containers to ensure minimal powder humidity until their content's further use in the ensuing PBF processes.

3.3. Preprocessing

As one of the key steps in additive manufacturing, preprocessing-aspects were naturally given special attention: A sample part geometry was chosen, CAD software was used to plan the manufacturing of an array of these specimens with carefully elected slicing and LPBF process parameters.

3.3.1. Sample Geometry

To be able to perform a variety of tests after the sample manufacturing and only basic postprocessing, a simple shape, that does not require any support structure, was chosen: a cylinder. To fit the proper number of specimens on the machine-wise predetermined 55 mm diameter base plate inlays without the need for vast amounts of neat powder and, in an effort to thereby reduce the accumulated powder waste to a minimum, a target sample size of 6.00 mm in height and 3.05 mm in diameter was defined. Additionally, since all samples were separated from their base plate by electrical discharge machining (EDM), 3.00 mm were added to the cylinder's height to account for this parting and any further postprocessing steps. Furthermore, to be able to distinguish individual samples after they have been separated from their baseplate, a number, protruding 0.25 mm and indicating the process parameters used in the respective sample, was added on top of the cylinders in CAD. Thus, as shown in figure 15, each sample's dimensions were defined to be 9.25 mm in height and 3.05 mm in diameter.

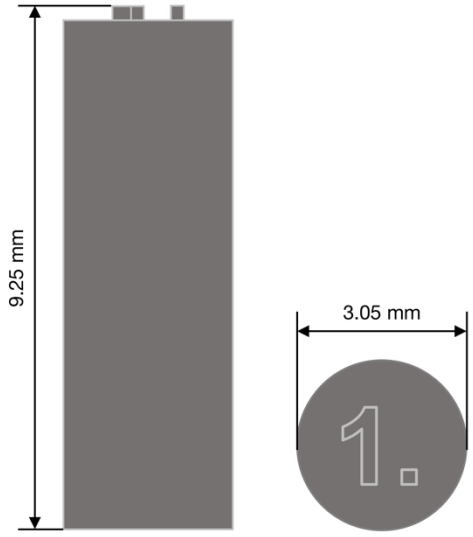

Figure 16: Schematic of one sample cylinder with its protruding numbering "1." on top.

3.3.2. CAD and Slicing

After the basic sample shape was defined, the subsequently required stereolithography (STL) files, sometimes called “Standard Tessellation Language” files, were created using Autodesk Netfabb [44]. This software allows simple CAD operations as well as all further features needed for additive manufacturing, like slicing and setting important process parameters such as layer height and hatching distance. Finally, an array of 64 samples was placed on a base plate with 55 mm diameter. Figure 17 shows a Netfabb screenshot of all specimen’s placement relative to each other.

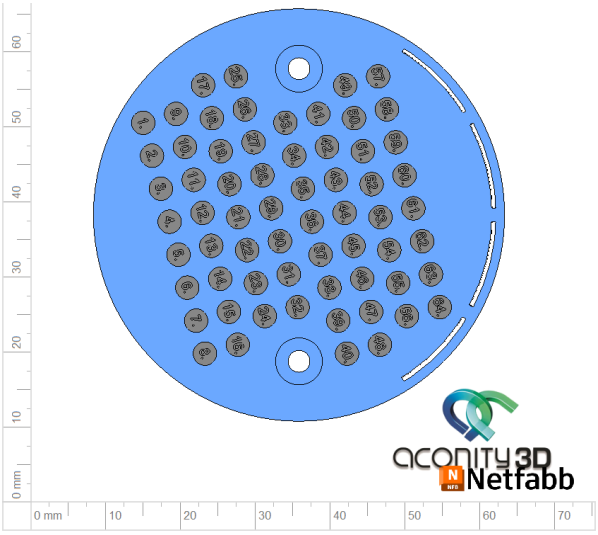

Figure 17: Sample placement on 55 mm diameter base plate (top view).

Following the digital sample placement, each one’s contour was offset inwards by 40 µm to take the LPBF machine’s laser spot size of 80 µm into account and prevent the process from producing substantial overexposure. Stripe hatching with contour was chosen as the same hatching style for all samples, since the inclusion of this additional and complex process parameter would extend the scope of this thesis. In order to ensure a sufficiently sized melt pool, meaning an overlap between two neighbouring tracks during the LPBF process, the hatching distance was – in accordance with relevant literature on the matter [45] – set to be equal to the laser spot size of 80 µm. The final slicing parameter, the angle increment, by which each new layer’s hatching direction is rotated relative to its underlying one, was set to be 43 °. This angle’s main requirement is that it should not be a divisor of 360. If that would be the case, the same laser path

would get exposed again after a defined number of layers and thus increase the probability for unequal heat distribution and the creation of hotspots, i.e. defects in the final product. All chosen slicing-parameters are comprehensively listed in table 3.

Table 3: List of the chosen slicing parameters.

Slicing Parameter	Value
Offset	-40 µm
Layer height	40 µm
Hatching distance	80 µm
Hatching style	Stripe with contour
Angle increment	43 °

Combining the sample's geometry and layer height, each sample was made up of 231 individual layers. These layers and their respective further settings were exported into command line interface (CLI) files, which are handleable by the AM machine used for sample production.

3.4. Laser Powder Bed Fusion

Following the previously mentioned preprocessing steps, further necessary part process parameters (PPPs) were defined directly at the LPBF machine, which was used for this thesis – along with all subsequent investigations – at the Erich Schmid Institute of Materials Science (ESI) at the Montanuniversität Leoben and is shown in figure 18, an Aconity MIDI+ by aconity3D [46].

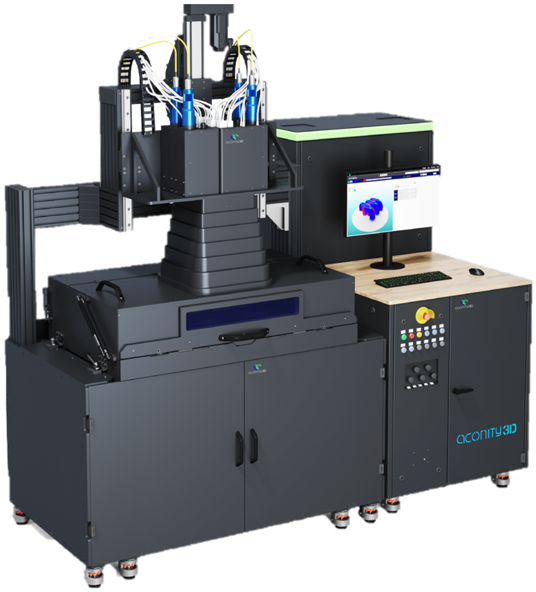

Figure 18: Aconity MIDI+, a LPBF machine by aconity3D, was used for this thesis [46].

3.4.1. Process Hardware

The used PBF machine is equipped with a class IV fiber laser with a maximum power – limited by the installed cooling system – of 500 W and a wavelength of 1070 nm for processing and one red class I guiding laser for ease of sample positioning with an undisclosed wavelength.

Aconity MIDI+ offers the option of various base plate and supply chamber, materials (steel or aluminium) as well as different recoaters. At the time, steel or aluminium plates with different dimensions, circular or rectangular shapes were available at the facilities at ESI. To use a minimal amount of powder, one modified baseplate, with an outer diameter of 250 mm and (up to) three in-line inlays with diameters of 55 mm (figure 19), respectively, was used. These base plates are made of the standard material for Aconity

MIDI+: 316L – a common austenitic stainless steel (X2CrNiMo17-12-2). Yet, since alle necessary samples fit on one of the inlays, only the most left inlay plate was used per alloy trial. To avoid any preventable powder loss, all other openings were sealed using antistatic adhesive tape.

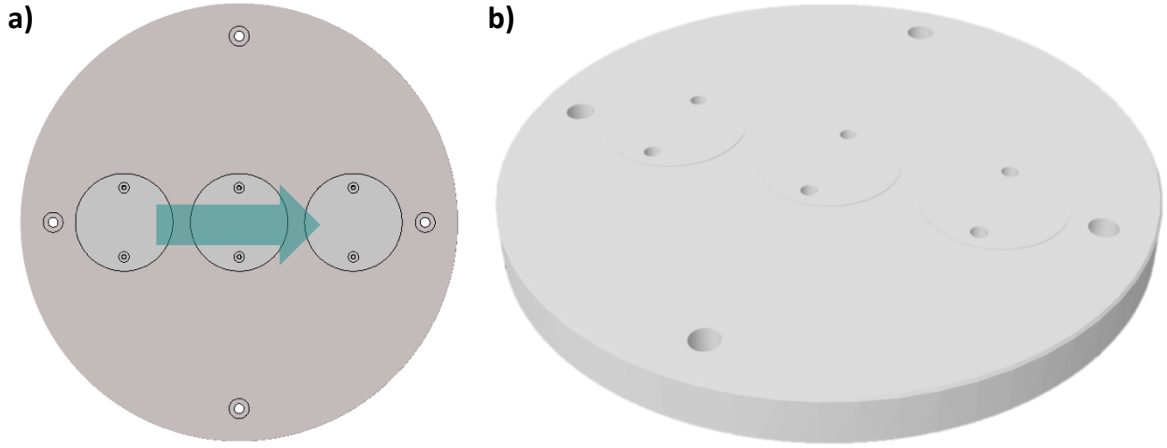

Figure 19: Modified base plate with three 55 mm inlays in **a)** top view and **b)** perspective view. The green arrow indicates the recoating direction.

All 250 mm diameter build plates are in direct contact with a water-cooled mounting system below, thus providing a near-constant downward heat flux during the LPBF process. Due to the limited process-specific know-how with the produced powder mixtures, a brush-style recoater was used for the subsequent sample production due to it being more forgiving concerning any uneven melting behaviour or protruding defects that might occur during the sample manufacturing.

The continuous O_2 level monitoring and precise control of both, the Ar inlet flow rate, as well as fume extraction, made possible by the accompanying software AconitySTUDIO for Aconity MIDI+, allow for the manufacturing process boundary conditions to be well defined. During the sample production, O_2 levels of 80.0 ppm and 59.5 ppm for both alloys, FeSi1.5wt% and FeSi3.5wt%, respectively, were maintained via an Ar gas flow rate of 7 l/min and a fume extraction rate of 1.5 m/s.

3.4.2. Part Process Parameters

After the CAD- and slicing phase, all further considered PPPs, namely laser power, scan speed, as well as additional boundary conditions were defined. As satisfactory results could be reached with a laser power of 150 W to 200 W for stainless and high speed steels, respectively, the former value was used as a starting point [47, 48]. Furthermore, power values of 125 W, 175 W and 200 W were investigated. The same approach was chosen for the laser scanning speed – here a value of 800 mm/s is one experience-based standard for other Fe-based materials [47]. To broaden the range of energy densities, scan speeds of 700 mm/s, 900 mm/s and 1000 mm/s were also considered. Table 4 summarizes all studied laser powers and scanning speeds into one matrix and assigns each power-speed-combination a respective letter.

Table 4: Laser power and scanning speed combination matrix with respectively assigned letters.

v / P	700 mm/s	800 mm/s	900 mm/s	1000 mm/s
125 W	A	B	C	D
150 W	E	F	G	H
175 W	I	J	K	L
200 W	M	N	O	P

To account for all subsequent experiments, four cylindrical samples were assigned to every one of the resulting 16 possible combinations of laser power and scanning speed. The resulting 64 specimens were arranged according to figure 20 for both alloys. The direction of exposure was chosen to be “from top to bottom”, i.e. against the direction of Ar flow. Additionally, in order to control the powder flow on the base plate, a thin wall, spanning one third of the plate’s circumference on the side opposing the supply chamber, i.e. on the plate’s right side, was added. Previous experiments showed, that due to the lack of any outer containment, like the build chamber wall in case the 250 mm plates would be used, this support is necessary, if 55 mm diameter inlays are being used. This wall – separated in four segments – is indicated by the grey arc on the plate’s left in figure 20.

Thus, with all important parameters fixed, the resulting volumetric energy densities were calculated using equation 4.

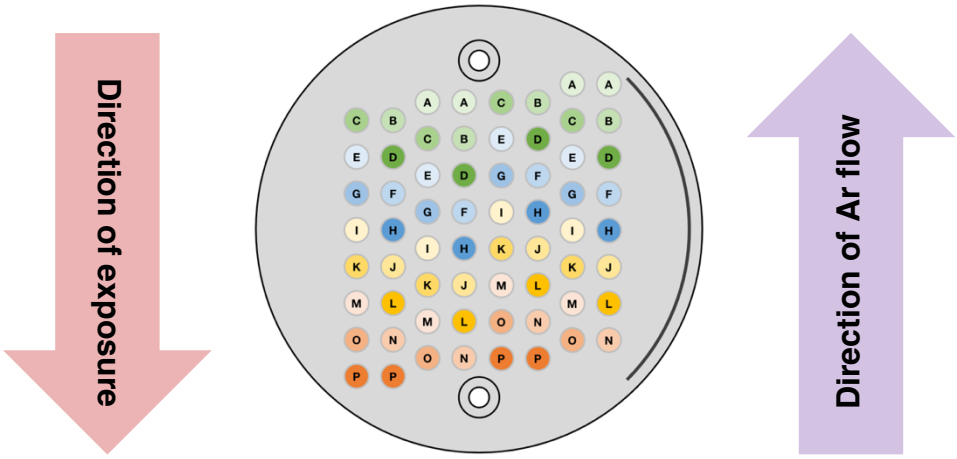

Figure 20: Schematic sample positioning, direction of Ar flow and direction of exposure.

The following calculation for the energy density of combination D (E_D) implements all necessary parameters into equation 4, i.e. the previously (in chapter 3.3.2.) defined hatching distance of 0.08 mm and powder layer thickness of 0.04 mm.

$$E_D = \frac{125\ \mathrm{W}}{1000\ \frac{\mathrm{mm}}{\mathrm{s}} \cdot 0.08\ \mathrm{mm} \cdot 0.04\ \mathrm{mm}} = 39.06\ \frac{\mathrm{J}}{\mathrm{mm}^3} \qquad (4)$$

The resulting values are shown – and color-coded – in table 5. The combination D (125 W laser power and 1000 mm/s scanning speed) yields in the lowest value of 39.06 J/mm^3. The other extreme – combination M (200 W and 700 mm/s) – can be found in the opposing matrix corner with an energy density of 89.29 J/mm^3.

Table 5: Laser power and scanning speed combination matrix with their respectively calculated and color-coded energy densities (J/mm^3). Green represents low and red represents high values.

v / P	700 mm/s	800 mm/s	900 mm/s	1000 mm/s
125 W	55.80	48.83	43.40	39.06
150 W	66.96	58.59	52.08	46.88
175 W	73.13	68.36	60.76	54.69
200 W	89.29	78.13	69.44	62.50

3.5. Postprocessing

Following the manufacturing, all samples – still attached to their base plate – were extensively cleaned with a brush, vacuum cleaner, 70 % pure isopropyl alcohol and ultrasonic cleaning. Thereafter, in order to obtain samples with correct dimensions and parallel cylinder faces and to remove the protruding numbering, which was needed to be able to distinguish and assign individual specimens after the EDM process. This grinding and polishing process was performed manually with a manual specimen holder by Kulzer GmbH – a device specifically made for the plano-parallel grinding of small samples (figure 21) [49]. The wet-grinding and subsequent -polishing was done in steps (500 grit, 800 grit and 1000 grit) with a Struers LaboPol-25 (figure 22).

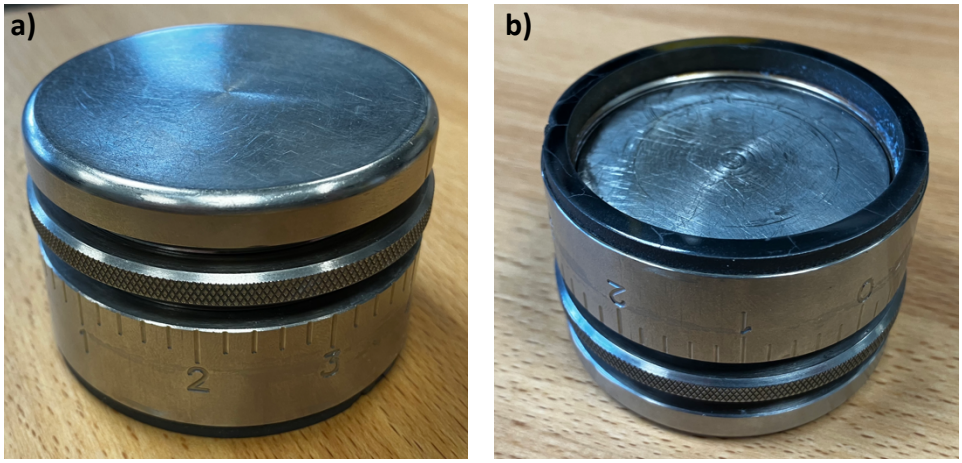

Figure 21: Kulzer manual specimen holder used to ensure the cylinder face's parallelism. **a)** Device in grinding position; **b)** Device in upside-down position.

Figure 22: Struers LaboPol-25 used for the performed wet-grinding and -polishing steps [48].

3.6. Sample Characterization

3.6.1. Sample Dimensions

Every specimen's outer dimensions – meaning cylinder diameter and height – were measured with an electronic outside micrometer (040-1865510 by Helios Preisser) after they have been cut from their base plates via EDM, as well as after their grinding and polishing to meet the defined dimensions. Thus, each cylinder's flat surfaces were processed, while their lateral surface stayed unpolished. The determined sample dimensions were further needed for additional characterization methods, such as compression testing and magnetic hysteresis testing.

3.6.2. Porosity Measurement

The final part's density, i.e. porosity plays, as is the case with more conventional powder based manufacturing processes, a major role in the characterization of PBF- and AM-manufactured products [31]. One industry-wide well-established method for nearly fully dense parts, i.e. parts with no significant open porosity, is the so-called the Archimedes method [51]. This method makes use of the fact, that the pores of a component act as microscopic, internal floats and thus apply an upward buoyant force, should the part be submerged in a liquid. The resulting reduction in weight in this state is measurable and, should the liquid's density be known, leads to the component's density. The sample's density (ρ) can be calculated by utilization of equation 5, whereby the dry sample's weight (m_{dry}), its weight in liquid (m_{liq}) are to be measured and the liquid's (temperature dependent) density (ρ_{liq}) has to be known [51]. All required values for ρ_{liq} for water and ethanol are listed in the used equipment's manual. For these measurements, a Sartorius SECURA225-1S precision scale and the further necessary density measurement kit VF4601 (figure 23) were used, which allows for the respective densities to be calculated automatically by the precision scale's designated density-measurement-setting.

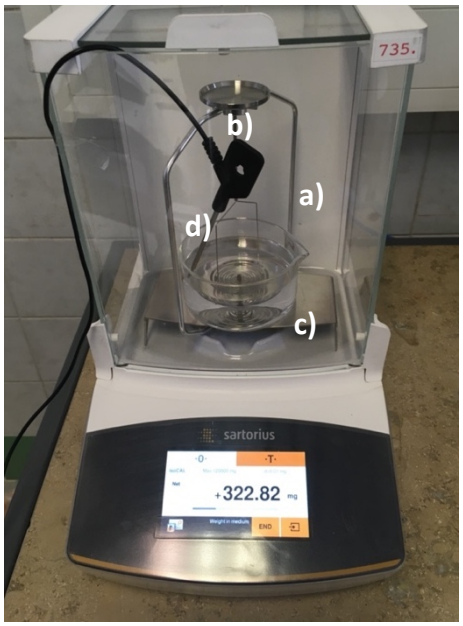

Figure 23: The utilized setup for density measurements: The density measurement kit includes **a)** a metal frame and **b)** a sample holder as well as **c)** a beaker. Additionally, **d)** an electronic thermometer was used.

$$\rho = \frac{\rho_{liq} \cdot m_{dry}}{m_{dry} - m_{liq}} \quad \left[\frac{g}{cm^3}\right] \tag{5}$$

For easier handling and because of its lower vapor pressure, deionized water was used as the liquid medium. Its temperature was constantly monitored during each measurement. Since, to calculate a sample's porosity, its bulk density must be known and no relevant and reliable data could be found in the literature, a fully dense sample of each alloy was made by virtue of an arc melting process. The melting process was repeated three times in pure Ar atmosphere in an Arc Melter AM/0,5 by Edmund Bühler GmbH per alloy specimen to ensure maximum homogeneity in the samples. Finally, every sample's porosity (Π) was calculated using equation 6 [50].

$$\Pi = \left(1 - \frac{\rho}{\rho_{bulk}}\right) \cdot 100\ \% \quad [\%] \tag{6}$$

With very well understood and fine-tuned process parameter-material-combinations, e.g. for various steels or Ti6Al4V, densities of up to 99.99 % of their respective bulk densities are achievable [51]. For this thesis, however, the goal was to obtain as low Π-values as possible with the previously defined process parameters. For even lower porosities, i.e.

fully dense samples, possible further refined parameters will be discussed in this thesis' conclusion.

3.6.3. Hardness Measurement

As an indicator for the mechanical performance of additively manufactured ferrosilicon, low force Vickers hardness measurements (HV0.5) were performed on a selection of samples. To rationally limit the necessary number of experiments, samples were picked based on their porosities: four specimens – one per corresponding part process parameter set – with relatively low porosities were chosen per alloy. These samples were first cut transversally (TV) to receive two halves, of which one would be further cut longitudinally (LT) (figure 24). All hardness tests were performed with a DuraScan 70 G5 hardness tester by Zwick/Roell (figure 25) and in accordance with the relevant standards EN ISO 6507 / ASTM E384. [52, 53]

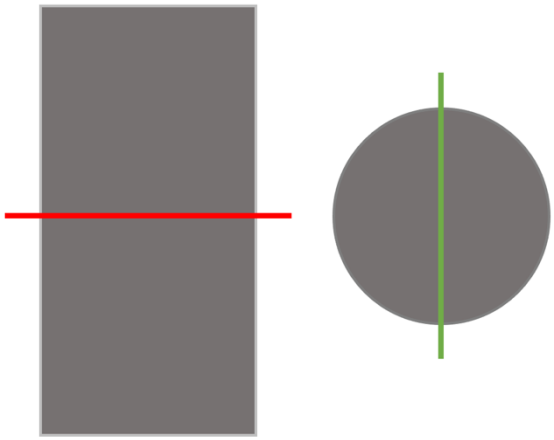

Figure 24: Schematic sample cylinder cutting: Transversal cut (red) followed by a longitudinal cut (green) on one of both halves.

After cutting, each of the samples were embedded in resin and further prepared to be examined in a SEM as well as low force hardness tested. As test method, HV0.5 testing was chosen. The test setup allowed for the necessary test force (F) of 4.903 N to be applied fully automatically. This force is equal to 0.5 kgf (kilogram-force or kilopond) and thus the namesake number in HV0.5.

Figure 25: DuraScan 70 by Zwick/Roell used for the low force Vickers hardness mapping [54].

To investigate any possible hardness variations across a sample's cross section, i.e. fluctuations between different laser scanning paths or individual layers, hardness maps were generated with a number of hardness indents that still allowed them to be sufficiently spaced apart to be valid tests according to the standards ($\geq 2.5\ d_{HV}$). To receive the Vickers hardness, a diamond pyramid indenter with a tip angle (θ) of 136 ° is pressed into a sample's surface for 10 to 15 s. The resulting indent shows two prominent diagonals (d1, d2), which are measured and averaged to receive the mean diagonal length (d_{HV}). This d_{HV} is further used in equation 7 to calculate HV0.5 [55].

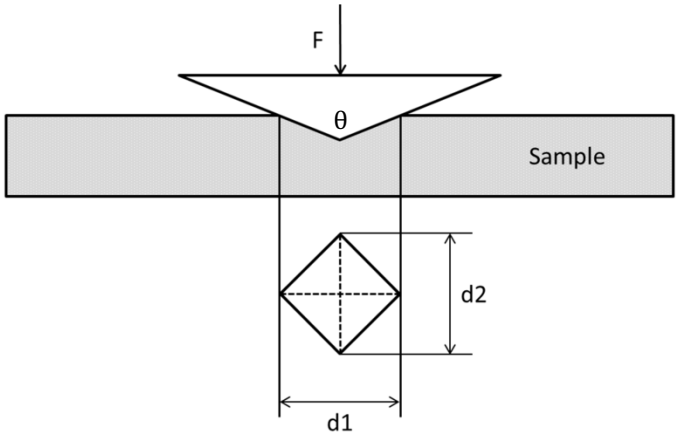

Figure 26: Schematic of a Vickers hardness test [55].

$$\mathrm{HV0.5} = 0.102 \cdot \frac{2 \cdot \mathrm{F} \cdot \sin\left(\frac{\theta}{2}\right)}{{d_{\mathrm{HV}}}^2} \quad \left[\frac{\mathrm{N}}{\mathrm{mm}^2}\right] \tag{7}$$

Vickers hardness is usually given as a dimensionless number, despite its arithmetical unit of force per area, i.e. stress (N/mm^2 or MPa). The state-of-the-art machine used for these measurements evaluates each indent automatically. All indents were examined and their diagonals measurements corrected, if nonsensical values were obtained due to some error in the machine's algorithm. Furthermore, a small python program was created using Anaconda Navigator 1.10.0 and its environment Spyder 4.1.5 to visualize the measured hardness maps and for the calculation of mean HV0.5 values. The code can be found in appendix 7.4.

3.6.4. Hysteresis Measurement

To conclude the testing regime, the magnetic behaviour of two samples was tested by virtue of a hystograph (figure 27), which was custom made by Dr. Brockhaus Messtechnik GmbH & Co. KG, which was employed due to the lack of an Epstein frame, which would be required for the comparable measurement of the additively manufactured samples with soft magnetic strip or sheet materials, i.e. electrical steel, according to DIN EN 60404-2 [56].

Figure 27: Experimental setup for magnetic testing.

Hystographs are mainly used for the characterization of hard magnetic materials and utilize relatively strong magnetic fields of up to 2.5 MA/m, while in Epstein frames, fields of up to 30 kA/m are common, thus making a quantitative remark on the magnetic performance of AM Fe-Si futile. However, as these magnetic fields are – as was described in chapter 2.2.6. – cycled to investigate the material's hysteresis behaviour in

both setups, a qualitative statement might be made. The hystograph uses a primary coil to impose the magnetic field and a secondary coil to measure the sample's resulting magnetization. The massive primary coil's two poles are used to clamp the sample, thus holding it in place for the measurement (figure 28). Before doing so, the specimen is placed inside a thin frame's center hole, which is surrounded by two secondary coils to receive the required data.

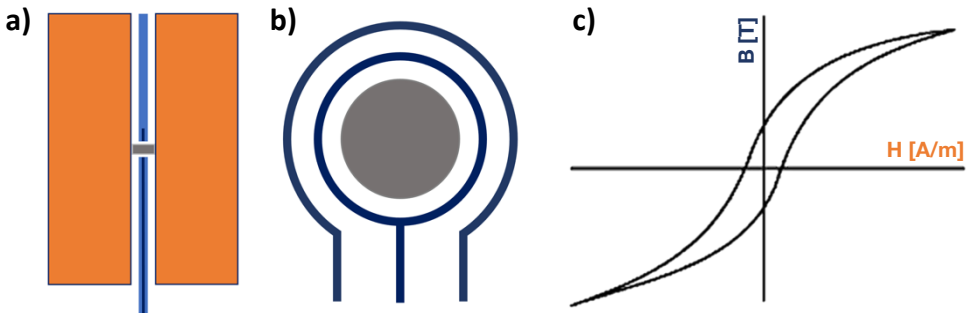

Figure 28: Schematic of a hystograph measurement: **a)** The sample (grey) is positioned between the two primary coil's poles (orange); **b)** Top view of the sample in the center of two secondary (dark blue) coils; **c)** The orange H (magnetic field strength) and green M (magnetization) relate to the primary and secondary coil's influence on the resulting B-H-curve's axes [57].

While the inner coil, which surrounds the specimen, measures the flux inside the sample, the outer one is facilitating the measurement of the flux through the air in vicinity of the cylinder, thus making it possible to subtract any external magnetic fields that might influence the experiment [58]. To perform the underlying calculations, the accompanying software, MPG Expert by Brockhaus, has to be provided with the sample's dimensions and density. Additionally, a maximum supply current for the primary coil, which was set to 5.0 A for both measurements, must be defined.

4. Results and Discussion

4.1. Powder Characteristics

As can be seen in figure 29, although smaller than 15 µm particles can be seen in both SEM images, none bigger than the proclaimed 53 µm could be found in the examined Fe powder sample.

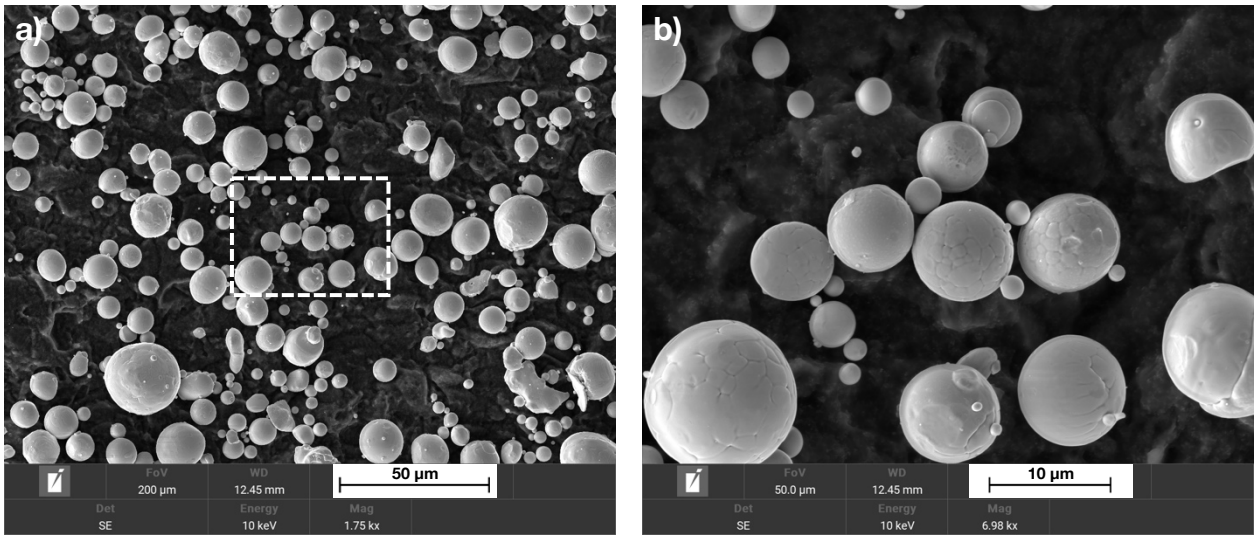

Figure 29: SEM images of Fe powder at **a)** 1750x and **b)** 6980x magnification.
The dashed box (left) indicates the position of the zoomed in image on the right.

At first glance, important qualities, such as the prominently consistent spherical shape, almost complete absence of strongly deformed or even acicular particles, as well as the presence of only occasional satellites, are apparent. In figure 29b, individual, roughly micrometer-sized grains can be distinguished in some of the investigated particles. The evident suitability of the obtained Fe powder for the use in AM becomes even more palpable, when compared to the Si powder on hand. The performed SEM imaging – as is shown in figure 30 – revealed the powder particles to be more of spheroidal or even flaky appearance than the desired spherical shape.

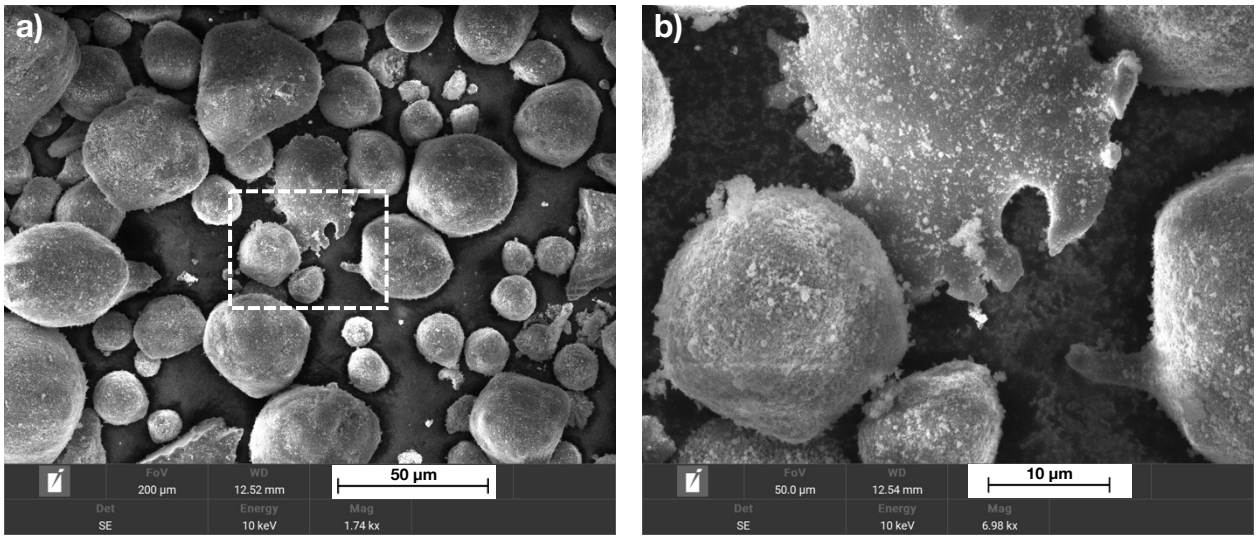

Figure 30: SEM images of Si powder at **a)** 1750x and **b)** 6980x magnification.
The dashed box (left) indicates the position of the zoomed in image on the right.

In addition to this AM-wise undesirable trait, individual particles ranging between 50 µm and 100 µm as well as significant amounts of finely dispersed oxides on the particle's surfaces (figure 30b) could be found.

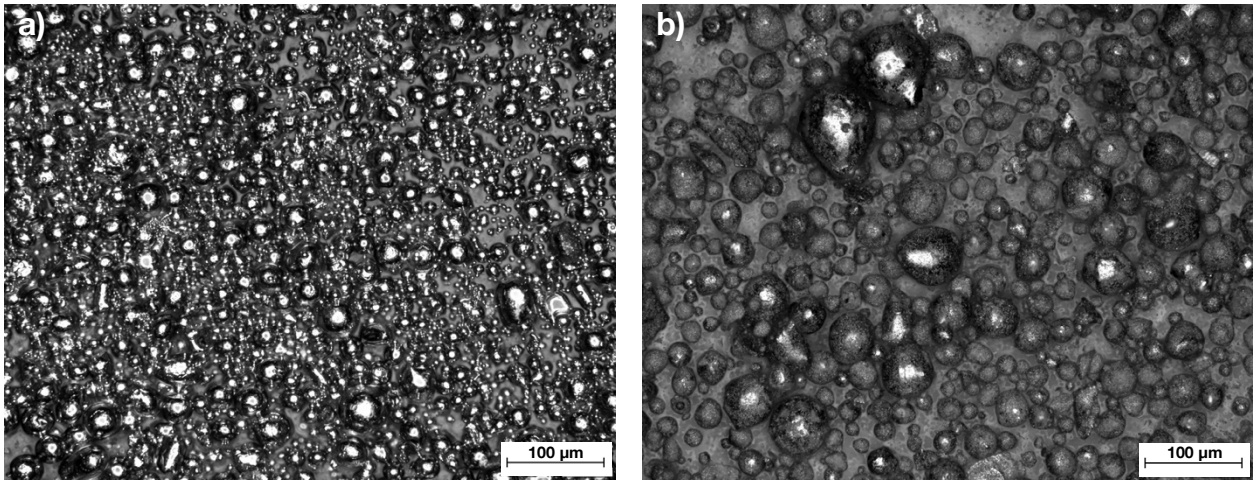

Figure 31: LIMI images of **a)** Fe powder & **b)** Si powder at 200x magnification.

Nonetheless, both powders were used for all further experiments, since particles with diameters larger than the set layer thickness during the LPBF process would simply be pushed aside by the recoater and therefore have no further influence on the process.
Figure 32 shows SEM images of FeSi3.5wt% after the mixing process. Evidently, no agglomerates formed during the mixing. Furthermore, due to of the eccentric rotational movement performed by the mixing device, no separation of Fe and Si happened, despite

their relative density difference. During the mixing process, previously described dispersed silicon oxides seem to have been evenly distributed throughout the blend as small specks are also visible on Fe particles.

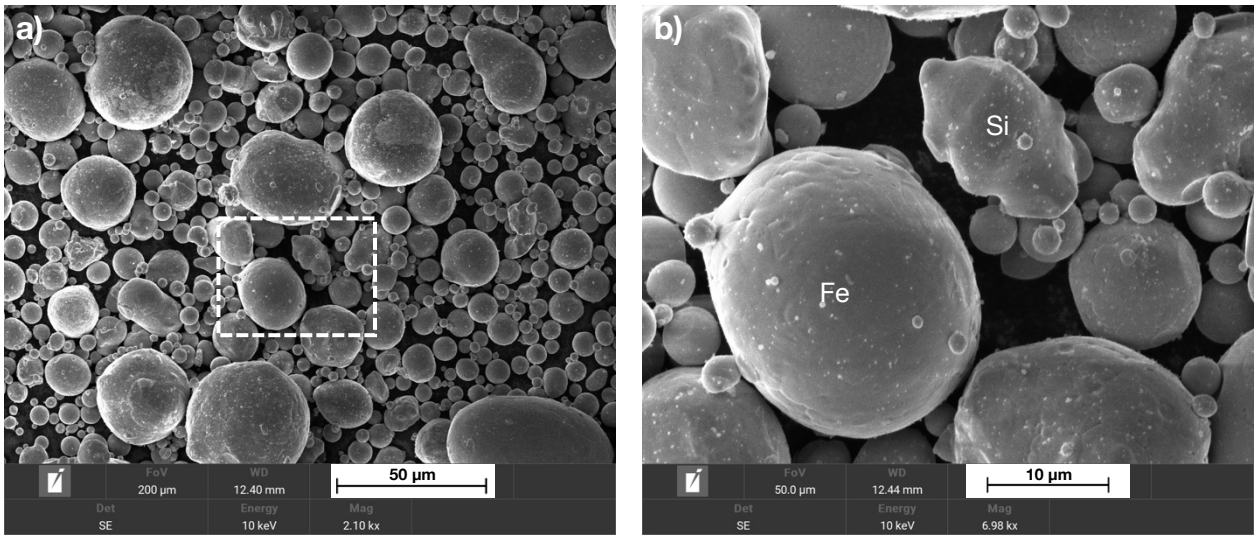

Figure 32: SEM images of mixed Fe-Si powder (FeSi3.5wt%) at **a)** 2100x and **b)** 6980x magnification. The dashed box on the left indicates the position of the zoomed in image on the right side.

Next to the overall morphology and due to the lack of provided information by the powder manufacturer, a particle size distribution analysis was performed by the utilization of figure 29, figure 30 and the open-source software ImageJ. This software allows the precise measurement of distances and areas, should a respective scale be provided in the image. Figure 33 shows the two particle size distributions: grey bars representing Fe and blue bars representing Si particles, based on figure 29 and figure 30, respectively. The Fe powder, as was already expected by looking at its SEM micrograph, consists of finer particles with values for D_{90}, D_{50} and D_{10} of 10.78 ± 2.49 µm, 4.55 ± 1.01 µm and 1.87 ± 0.33 µm, respectively. The Si powder sample generally consists of larger, less rounded, particles. The measured values of 28.19 ± 7.47 µm for D_{90}, 13.37 ± 4.08 µm for D_{50} and 2.03 ± 0.34 µm for D_{10} further acknowledge this observation. Although not as narrow as expected, both powder sample's particle size distributions are well within the manufacturer-side proclaimed upper limit of 53 µm. The lower limit of 15 µm, however, was – especially when looking at the Fe powder data – largely not met.

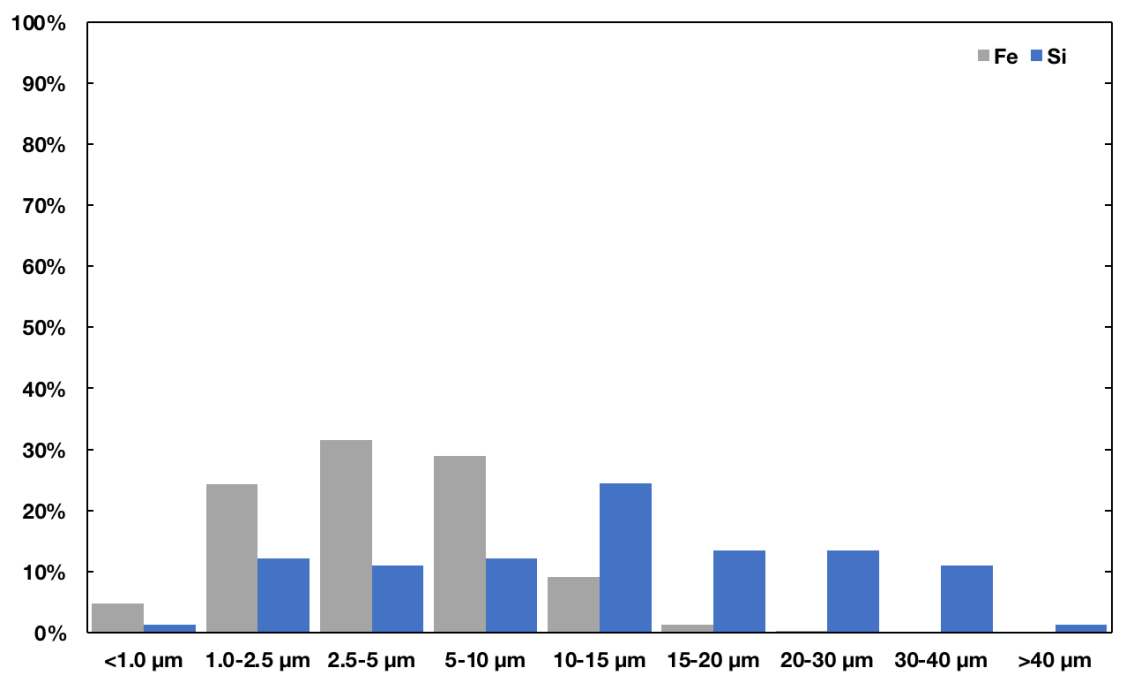

Figure 33: Particle size distribution of Fe (grey) and Si (blue) powders.

4.2. Sample Dimensions

After the successful AM sample production (figure 34), all 128 samples – 64 per alloy – were separated from their respective base plates via EDM to be ground and polished down to the required dimensions.

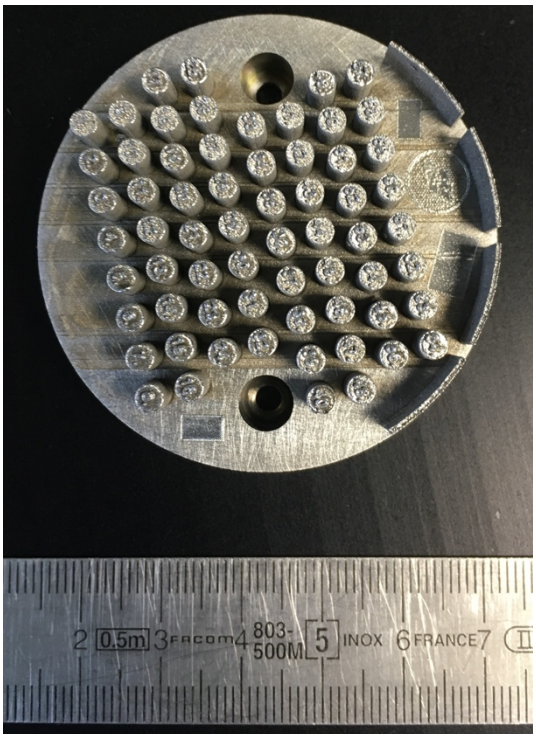

Figure 34: FeSi3.5wt% samples, still attached to their base plate after manufacturing.

Table 6 and table 7 comprehensibly indicate that, due to overexposure and the effects of the processing laser spot's energy distribution not being in an ideal top hat shape, a heat affected zone, surpassing the chosen offset of 40 µm, led to generally too large sample diameters. The average excess in sample diameters – 157.66 ± 12.47 µm in case of FeSi1.5wt% and 170.70 ± 14.38 µm in case of FeSi3.5wt% – suggest a systematic error, which would be handleable by reducing the sample's diameter in the early CAD stage accordingly. However, further experiments, to prove the consistency of this error independence from the sample's shape, were not conducted.

Table 6: Measured sample diameters (mm) for FeSi1.5wt%.

v / P	700 mm/s	800 mm/s	900 mm/s	1000 mm/s
125 W	3.20 ± 0.01	3.20 ± 0.01	3.20 ± 0.01	3.19 ± 0.01
150 W	3.20 ± 0.01	3.20 ± 0.01	3.20 ± 0.01	3.20 ± 0.01
175 W	3.21 ± 0.01	3.21 ± 0.01	3.21 ± 0.01	3.21 ± 0.01
200 W	3.22 ± 0.01	3.23 ± 0.01	3.21 ± 0.02	3.24 ± 0.01

Table 7: Measured sample diameters (mm) for FeSi3.5wt%.

v / P	700 mm/s	800 mm/s	900 mm/s	1000 mm/s
125 W	3.20 ± 0.01	3.21 ± 0.01	3.22 ± 0.01	3.19 ± 0.01
150 W	3.22 ± 0.01	3.22 ± 0.01	3.21 ± 0.01	3.21 ± 0.01
175 W	3.23 ± 0.01	3.22 ± 0.01	3.22 ± 0.02	3.22 ± 0.01
200 W	3.24 ± 0.02	3.24 ± 0.01	3.23 ± 0.02	3.24 ± 0.02

As all specimens needed to be ground and polished to meet their specified heights of 6.00 mm, lateral dimension measurements before this postprocessing step were, albeit not imperative, conducted. This data can be found in appendix 7.1. The mean cylinder's heights are listed in table 8 and table 9. Since this step was performed manually, mean deviations from the target measurement of 6.00 mm by 97.78 ± 86.23 µm (FeSi1.5wt%) and 66.78 ± 28.05 µm (FeSi3.5wt%) were deemed satisfactory.

Table 8: Measured sample heights (mm) for FeSi1.5wt%.

v / P	700 mm/s	800 mm/s	900 mm/s	1000 mm/s
125 W	5.69 ± 0.00	5.98 ± 0.06	6.09 ± 0.09	6.08 ± 0.03
150 W	6.10 ± 0.02	6.07 ± 0.02	6.16 ± 0.08	6.28 ± 0.06
175 W	6.10 ± 0.05	6.03 ± 0.03	6.09 ± 0.02	6.01 ± 0.04
200 W	5.97 ± 0.10	6.00 ± 0.01	5.98 ± 0.02	5.93 ± 0.04

Table 9: Measured sample heights (mm) for FeSi3.5wt%.

v / P	700 mm/s	800 mm/s	900 mm/s	1000 mm/s
125 W	5.92 ± 0.02	5.99 ± 0.06	6.06 ± 0.04	6.14 ± 0.02
150 W	6.05 ± 0.09	6.07 ± 0.01	6.05 ± 0.06	6.06 ± 0.04
175 W	6.07 ± 0.02	6.07 ± 0.05	6.10 ± 0.01	6.04 ± 0.03
200 W	5.91 ± 0.02	5.95 ± 0.02	6.02 ± 0.01	6.05 ± 0.05

4.3. Porosity Measurements

By virtue of the precision scale's capability to perform density calculations automatically after the liquid's correct current density has been entered, the following mean densities, listed in table 10 were obtained for the reference bulk materials, i.e. both fully dense arc melted specimens.

Table 10: Measured bulk densities.

Alloy	ρ_{bulk} [g/cm^3]
FeSi1.5wt%	7.772
FeSi3.5wt%	7.654

It is noteworthy, that $\rho_{bulk,3.5wt\%}$ diverges substantially from literature values, which are usually not measured, but calculated based on both pure constituent's densities and their respective mass percentages [10]. This method, however, results in an approximated value, as it disregards the change of lattice constants, or even their crystal structure, and thus the change in bulk density, in case two (or more) elements form a solid solution. Therefore, both experimentally received values serve as references for the further porosity calculation according to equation 6. Table 11 and table 12 list all obtained mean densities for FeSi1.5wt% and FeSi3.5wt%, respectively.

Table 11: Obtained sample densities (g/cm^3) of FeSi1.5wt%.

v / P	700 mm/s	800 mm/s	900 mm/s	1000 mm/s
125 W	7.514 ± 0.083	7.497 ± 0.066	7.545 ± 0.062	7.406 ± 0.058
150 W	7.627 ± 0.067	7.557 ± 0.071	7.625 ± 0.028	7.584 ± 0.058
175 W	7.643 ± 0.038	7.640 ± 0.054	7.616 ± 0.067	7.631 ± 0.062
200 W	7.630 ± 0.038	7.659 ± 0.022	7.642 ± 0.046	7.659 ± 0.052

Table 12: Obtained sample densities (g/cm^3) of FeSi3.5wt%.

v / P	700 mm/s	800 mm/s	900 mm/s	1000 mm/s
125 W	7.507 ± 0.075	7.398 ± 0.093	7.360 ± 0.069	7.301 ± 0.097
150 W	7.562 ± 0.036	7.564 ± 0.031	7.566 ± 0.052	7.563 ± 0.040
175 W	7.576 ± 0.033	7.586 ± 0.032	7.594 ± 0.044	7.534 ± 0.083
200 W	7.558 ± 0.040	7.577 ± 0.036	7.563 ± 0.041	7.553 ± 0.041

Finally, based on equation 6, these listed densities and their corresponding bulk, i.e. reference, values, the following (table 13 and table 14) energy density-depended porosities were calculated. For individual sample data, please refer to appendix 7.2.

Table 13: Calculated porosities (%) for FeSi1.5wt% with corresponding relative color-codes. Green represents relatively low and red higher porosities.

v / P	700 mm/s	800 mm/s	900 mm/s	1000 mm/s
125 W	3.32 ± 1.07	3.53 ± 0.85	2.92 ± 0.80	4.70 ± 0.75
150 W	1.87 ± 0.86	2.76 ± 0.91	1.89 ± 0.37	2.42 ± 0.74
175 W	1.66 ± 0.49	1.70 0± 0.69	2.01 ± 0.87	1.82 ± 0.79
200 W	1.83 ± 0.49	1.45 ± 0.28	1.67 ± 0.60	1.45 ± 0.67

Table 14: Calculated porosities (%) for FeSi3.5wt% with corresponding relative color-codes. Green represents relatively low and red higher porosities.

P \ v	700 mm/s	800 mm/s	900 mm/s	1000 mm/s
125 W	1.91 ± 0.98	3.34 ± 1.21	3.83 ± 0.90	4.60 ± 1.26
150 W	1.20 ± 0.47	1.18 ± 0.41	1.14 ± 0.68	1.18 ± 0.53
175 W	1.02 ± 0.44	0.88 ± 0.42	0.78 ± 0.58	1.56 ± 1.08
200 W	1.25 ± 0.52	1.00 ± 0.48	1.18 ± 0.54	1.31 ± 0.54

At the very first glance, it is apparent, that the energy density heavily influences the final part's porosity. While the lowest energy influx D (125 W and 1000 mm/s), predictably results in the highest porosities for both investigated alloys, the optimal P-v-combination slightly varies, with N (200 W and 800 mm/s) and J (175 W and 900 mm/s), for FeSi1.5wt% and FeSi3.5wt%, respectively. However, both combinations I and N (175 W and 200 W with 800 mm/s) yield relatively low Π values, both within the standard deviation of J. The plotting of all obtained porosities over their respective energy densities clearly emphasizes the correlation of these two parameters. As can be seen in both Π-E-graphs, i.e. figure 35 and figure 36.

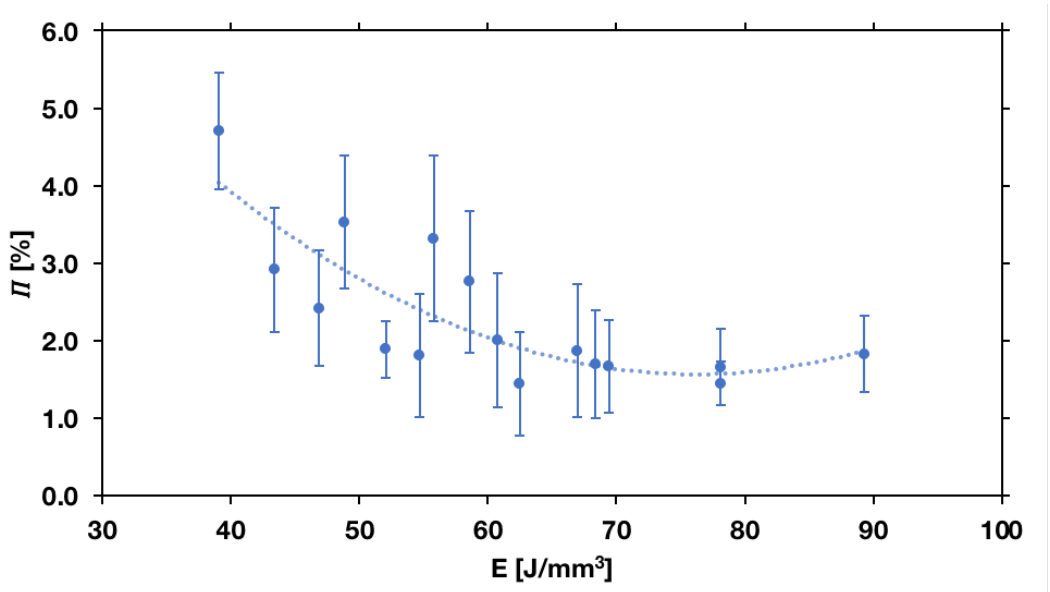

Figure 35: Π-E-graph for FeSi1.5wt%. A quadratic polynomial (dotted line) was fitted to the calculated porosities (dots).

To find the optimal energy density, a quadratic polynomial was fitted for both alloys.

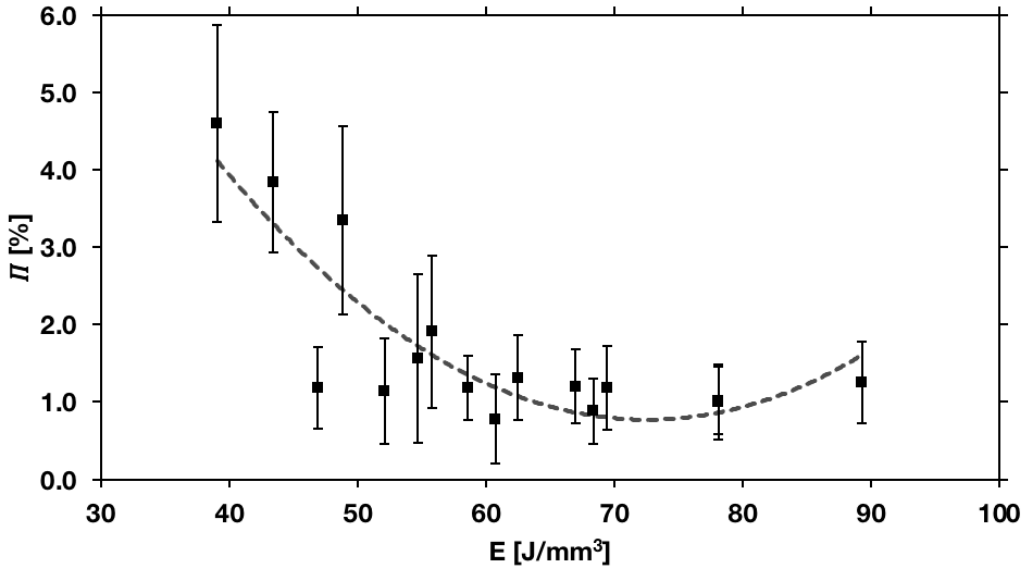

Figure 36: Π-E-graph for FeSi3.5wt%. A quadratic polynomial (dashed line) was fitted to the calculated porosities (squares).

Both polynomial functions for FeSi1.5wt% and FeSi3.5wt%, i.e. equation 8 and equation 9, respectively, were derived to find the minimum values for Π and their corresponding energy densities.

$$\Pi_{\mathrm{FeSi1.5wt\%}} = 0.0018 \cdot \mathrm{E}^2 - 0.2734 \cdot \mathrm{E} + 11.985 \quad (8)$$

$$\Pi_{\mathrm{FeSi3.5wt\%}} = 0.0030 \cdot \mathrm{E}^2 - 0.4323 \cdot \mathrm{E} + 16.455 \quad (9)$$

From these derivatives (equation 10 and equation 11), E_{min}, being the energy density for each respective alloy's minimum porosity, can be calculated by finding E for $\frac{\mathrm{d}\Pi}{\mathrm{dE}} = 0$.

$$\frac{\mathrm{d}\Pi_{\mathrm{FeSi1.5wt\%}}}{\mathrm{dE}} = 0.0036 \cdot \mathrm{E} - 0.2734 \quad (10)$$

$$\frac{\mathrm{d}\Pi_{\mathrm{FeSi3.5wt\%}}}{\mathrm{dE}} = 0.0060 \cdot \mathrm{E} - 0.4323 \quad (11)$$

The close proximity of both values – 76.20 J/mm^3 for FeSi1.5wt% and 72.57 J/mm^3 for FeSi3.5wt% – indicates an achievable porosity minimum within a relatively small energy density range. Figure 37 depicts the superimposition of all porosity-energy density combinations for both investigated alloys as well as E_{min} according to their respective

polynomial fits. Based on these performed porosity analyses, samples with P-v-combinations J, N, O and P were further investigated with the subsequent mechanical testing, thus rooting out all other PPP sets due to relatively high porosities.

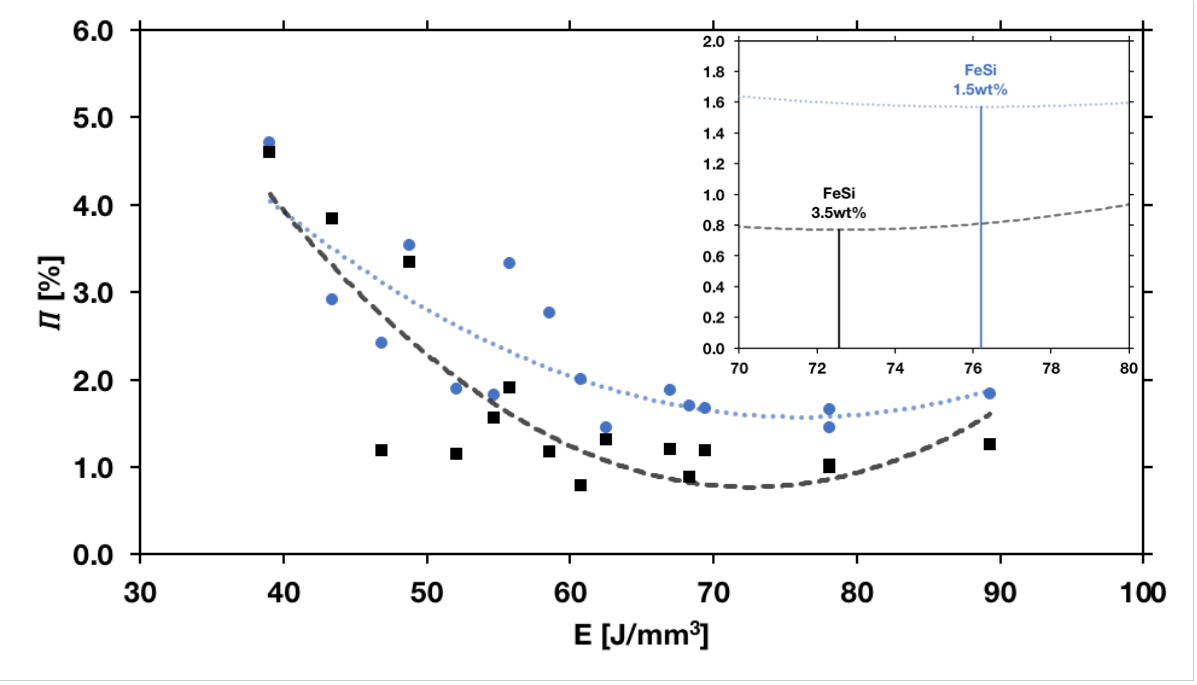

Figure 37: Π-E-graph for FeSi1.5wt% (blue / dots) and FeSi3.5wt% (black / squares) with fitted polynomials and their derived porosity minima. Depiction without error bars for presentation purposes.

4.4. SEM Micrographs

Following the density measurements, the calculation of Πs and the selection of least porous specimens, SEM samples were – as previously describes – prepared and SEM micrographs taken. A small selection of those will be described in this chapter. For further SEM images of each sample, please refer to appendix 7.3. Lastly, two promising samples were analysed via electron backscatter diffraction (EBSD) to reveal their grain's orientation.

4.4.1. FeSi1.5wt% Micrographs

Figure 38 depicts sample № 62, which was manufactured using the PPP set J, i.e. 175 W and 800 mm/s, transversally (figure 38a) and longitudinally (figure 38b) cut. Pores are mainly found along the contour and up to roughly 200 µm below the cylinder's surface. Some individual particles, that attached too strongly to be removed by the cleaning process, can be seen along the sample's edge.

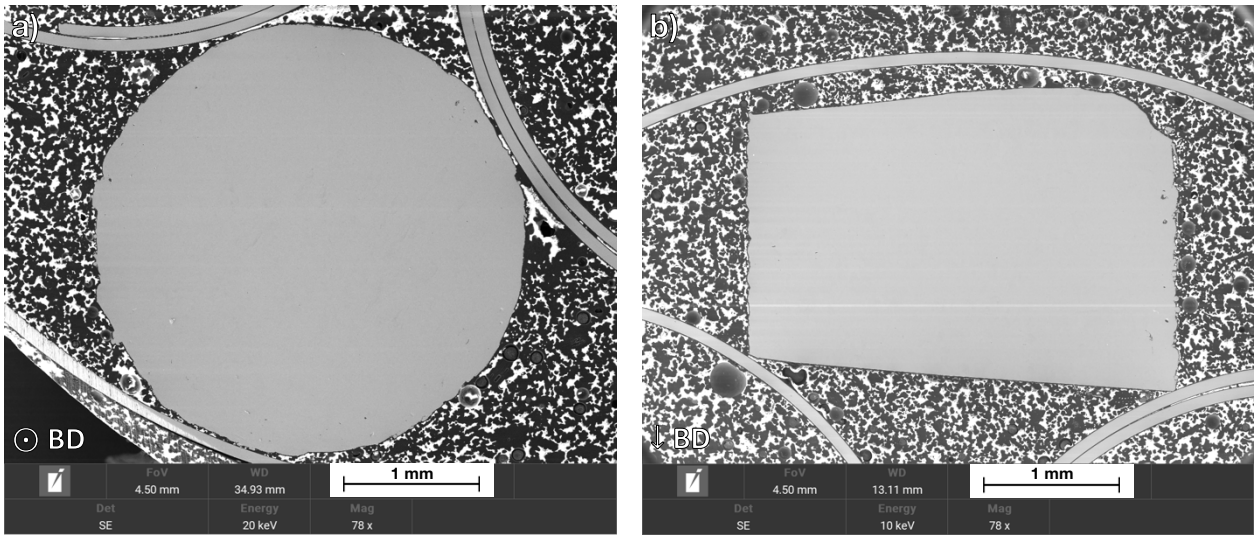

Figure 38: FeSi1.5wt% sample (PPP set J): Most pores are in the sub-micron range, yet some range from 5 µm to 10 µm. Individual pores can be seen mainly along the contour in **a)** the cross section and **b)** the lengthwise cut sample.

Sub-micrometer small pores are predominant in this sample and defects larger than a few micrometers are rarely found in the bulk, i.e. more than 200 µm under the sample's surface. This observation is confirmed, when looking at the lengthwise cut cylinder

(figure 38b). The rare large pores, however, indicate incomplete melting behaviour as intact powder particles can be found lining the pore's walls.

Figure 39 depicts sample № 64, of PPP set N (200 W and 800 mm/s). Here the porosity along the contour became more prominent, yet again at roughly 200 µm below the specimen's surface, a border could be drawn where almost no pores larger than 10 µm could be found. However, the near-surface porosity was more noticeable and even formed localized networks which were hard to distinguish from micro cracks.

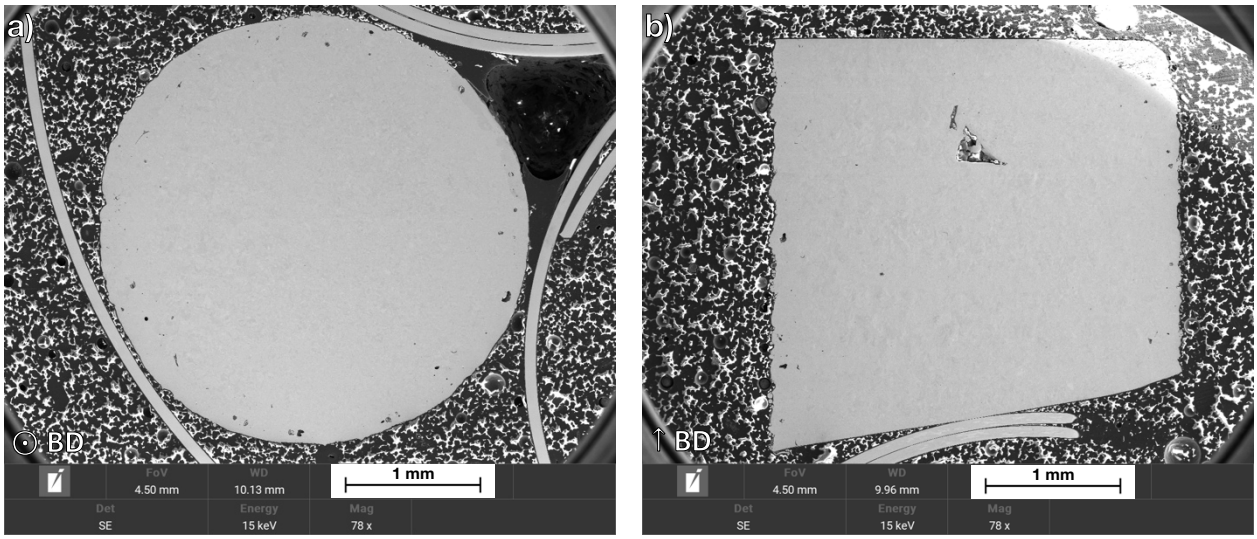

Figure 39: FeSi1.5wt% sample (PPP set N) at 78x magnification: **a)** Pores concentrate along the contour; **b)** Larger pore networks near the surface.

The lengthwise cut PPP set N sample (figure 39b) impresses with two massive pores along its centre axis. One of which – measuring roughly 400 µm at its maximum extend and perpendicular to BD – is partially filled with melted, as well as unmelted material, suggesting a considerable error during the manufacturing process. The sample's SEM micrographs suggest, besides the two massive defects in its centre, relatively high density. Thus, the main standard deviation in N's porosity might come from these specific pores.

Sample № 56, which was manufactured with P-v-combination O (200 W and 900 mm/s) is shown in figure 40. In this specimen, the previously described surface-near areas with more higher pore concentrations could not be found, as pores – roughly 50 µm and more in diameter – are present throughout the sample.

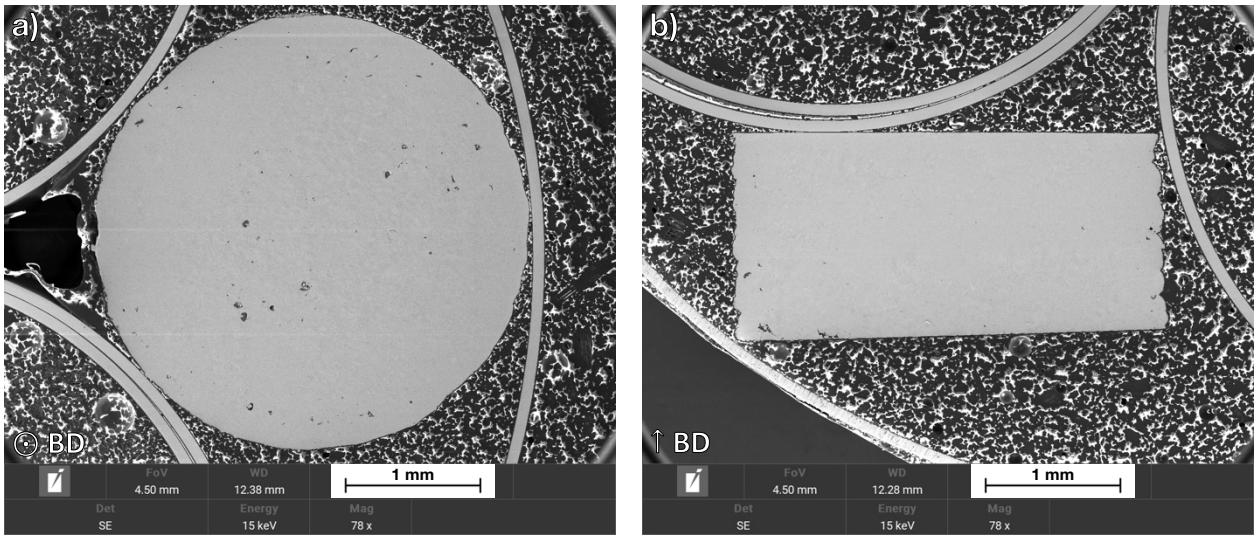

Figure 40: FeSi1.5wt% sample (PPP set O) at 78x magnification: **a)** Pores can be found throughout the specimen, which is not as clear in **b)** its longitudinal cut.

As the last representative specimen of FeSi1.5wt%, sample № 48, manufactured using PPP set P, i.e. 200 W and 1000 mm/s, was prepared and examined. The SEM imaging revealed relatively large pores, forming in a ring pattern along the contour line, as is clearly visible in figure 41. The perpendicularly cut half revealed massive pores – again hinting at subpar manufacturing parameters.

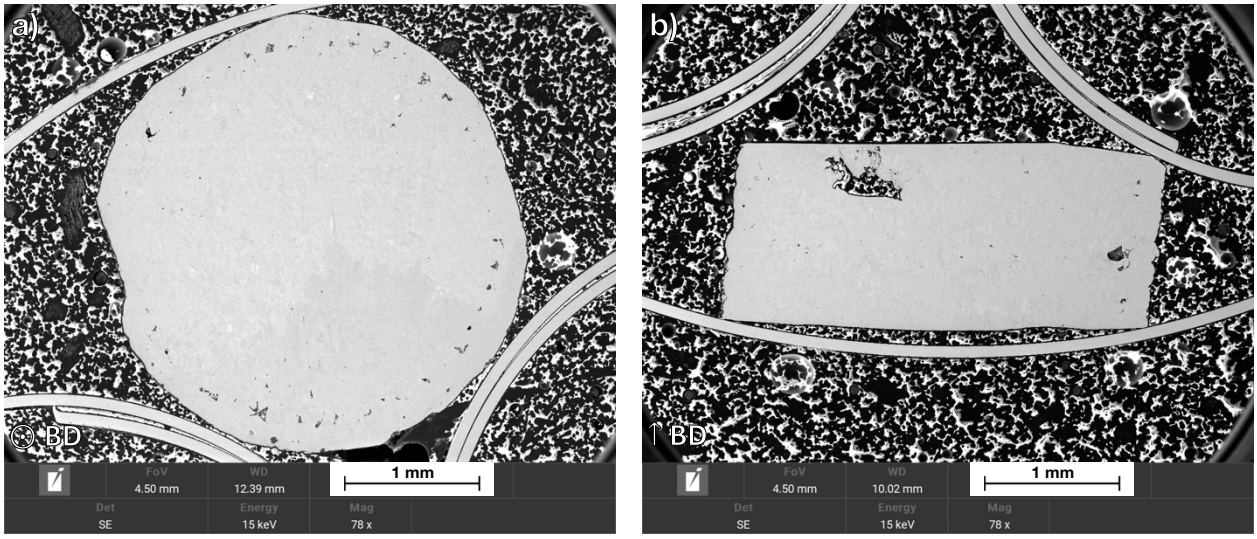

Figure 41: FeSi1.5wt% sample (PPP set P) at 78x magnification: **a)** Large pores concentrate around the sample's contour; **b)** Massive defects became apparent in its longitudinal cut.

The largest defect spread approximately 600 µm through the sample. Additionally, it seems that this defect led to incomplete melting in the subsequent layers above it, as individual, partially melted, powder particles can be seen in figure 41b.

These exemplary micrographs emphasize once again the importance of precisely tuned process parameters in LPBF. An energy density variation of 5.86 J/mm^3, i.e. the difference between both laser power-scanning speed-combinations J and P, may result in parts with few, localized pores (PPP set J), or in parts with major, macroscopic defects (PPP set P).

4.4.2. FeSi3.5wt% Micrographs

Sample № 45 was the first of four FeSi3.5wt% specimens to be examined. This sample was manufactured using PPP set J and showed, as can be seen in figure 42, a small number of pores along the contour, as well as the centre region.

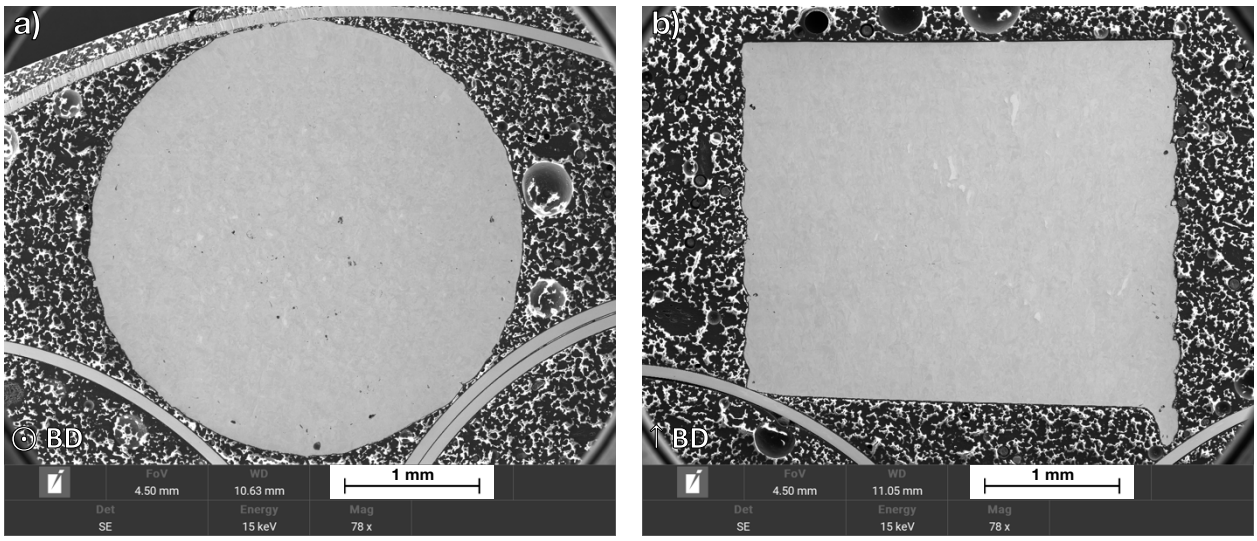

Figure 42: FeSi3.5wt% sample (PPP set J) at 78x magnification: **a)** Larger pores concentrate around the sample's contour and can also be found in lower numbers in its center; **b)** Pores are majorly found close to the sample's edge.

The largest defects measured approximately 100 µm. The longitudinally cut sample, shown in figure 42b, in contrast to its perpendicularly cut half, revealed few smaller pores in the bulk and more and larger ones closer to its edge. Interestingly, some areas seem to not have formed the desired alloy, but rather islands of almost pure Fe, as later energy-dispersive X-ray spectroscopy measurements would confirm.

This localized unmixing and the subsequently visible Fe areas are even more pronounced in sample № 15 (PPP set N). Besides these peculiarities, this sample's pores again concentrated along its contour, as is presented in figure 43.

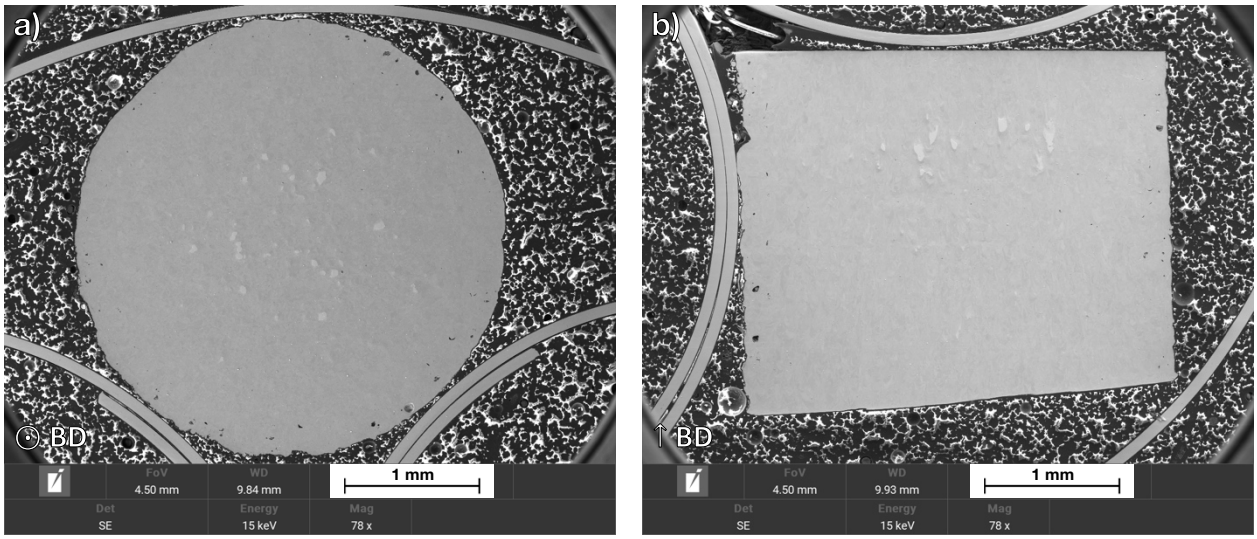

Figure 43: FeSi3.5wt% sample (PPP set N) at 78x magnification: **a)** Next to the lighter Fe islands in the sample center, most pores can be found along its edge; **b)** The lengthwise cut specimen reveals that Fe islands seem to be found mainly above a certain layer number.

The higher concentration of Fe islands above a certain sample height suggests, that there might have been larger Fe powder particles present during the recoating of the corresponding layers. These individual areas of pure Fe were also present in sample № 39 after its manufacturing with PPP set O. Additionally, a higher number of pores could be detected in the sample's centre region as well as relatively large ones close to its outline. The LT cut sample (figure 44b) suggests some sort of binding error between distinctive individual layers. This is represented through two almost perfectly straight lines of pores perpendicular to the building direction. These two lines are roughly 100 µm apart, suggesting two events of imperfect fusing between a neat powder layer and its underlying, already melted and solidified predecessor.

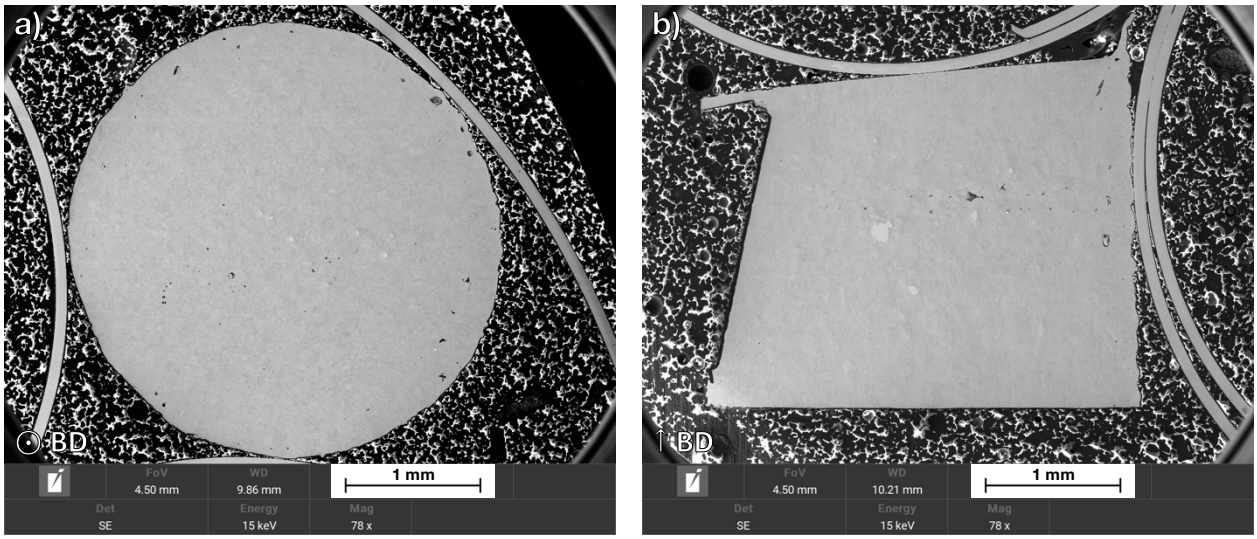

Figure 44: FeSi3.5wt% sample (PPP set O) at 78x magnification: **a)** Pores are no longer concentrated along the contour; **b)** Individual Fe islands, as well as pores, accumulated along almost straight lines perpendicular to BD, are visible.

Lastly, sample № 40 which was made with PPP set P was examined. Here, although once again Fe islands could be found, most pores formed along the specimen's outline with few individuals surpassing 20 µm in diameter (figure 45).

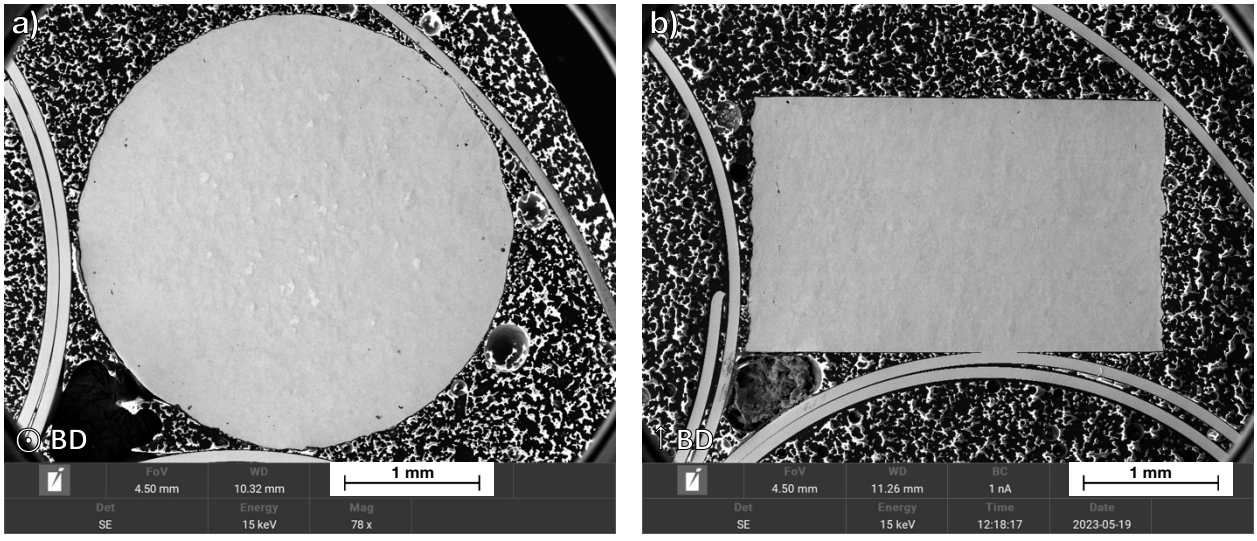

Figure 45: FeSi3.5wt% sample (PPP set P) at 78x magnification: **a)** Pores are once again mainly found along the sample's contour; **b)** Individual Fe islands and no pores larger than approximately 20 µm are visible.

4.4.3. EBSD Measurements

To better understand the printed sample's morphology, additional EBSD measurements were performed using the TESCAN MAGNA. Two samples, both made with the same P-v-combination of 200 W laser power and 800 mm/s scanning speed (PPP set N), were chosen and investigated at a tilt angle of 70 °. For their analysis, the inverse pole figure z-scheme (IPF-Z) was used for both EBSD maps.

Sample № 64, i.e. the specimen representing FeSi1.5wt% in figure 46, consists of localized regions of accumulated small grains and indicates no clearly preferred crystallographic direction. Insufficiently melted, yet embedded powder grains, might explain the stark contrast between the larger grains with less porosity, the relatively confined areas of higher porosity – depicted as individual black pixels – and the proximity of fine grains to those areas. In addition to these micropores, surface defects, e.g. black streaks from scratches due to improper sample manipulation are visible. However, further parameter studies with a refined part process parameter set might deliver similar results for FeSi1.5wt% and for FeSi3.5wt%, as parts of figure 46 already consist of larger and more homogeneously oriented grains, thus indicating the process's feasibility.

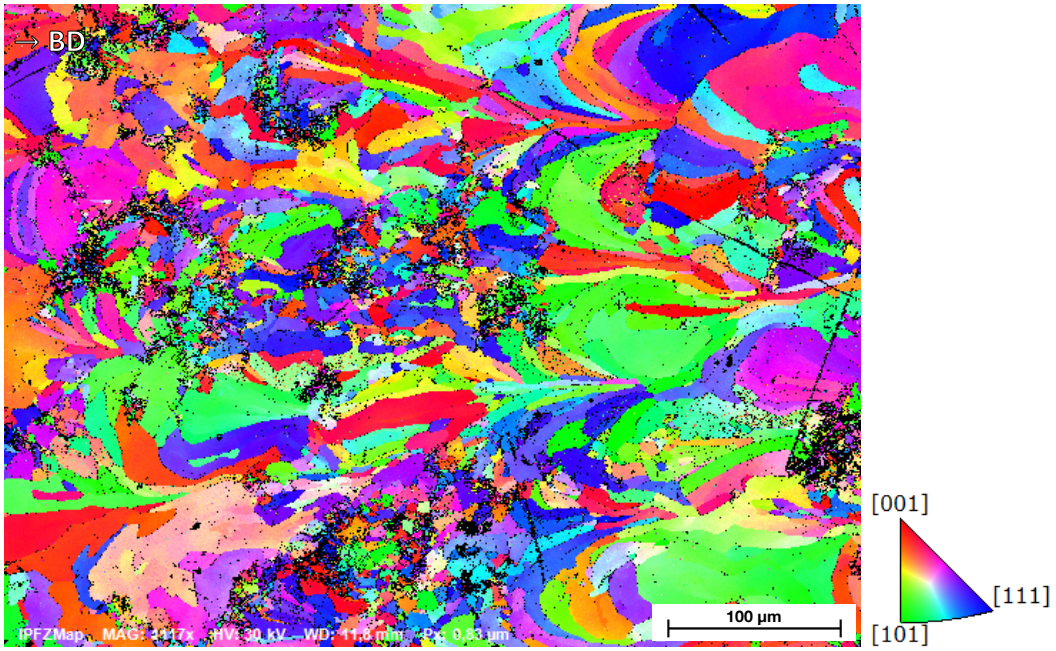

Figure 46: EBSD image of one FeSi1.5wt% sample made with PPP set N.

FeSi3.5wt% sample № 40's grains are, in comparison to the FeSi1.5wt% sample's, more coherent in size and orientation, thus implying a more consistent melting behaviour for the utilized PPP set. Additionally, less pores and surface defects are present in this specimen, as can be seen in figure 47. Areas of <100> and <101> directions clearly dominate the micrograph, making it partially difficult to distinguish individual scanning tracks and their corresponding former melt pool paths. The IPF-Z colouring scheme further reveals the preferred grain orientations to be magnetically soft, i.e. <100>, depicted as red areas, and intermediately soft directions, i.e. <101>, depicted as green areas, and perpendicular to the building direction. Whereas blue areas, indicating <111>, i.e. magnetically hard directions are only marginally found in this direction.

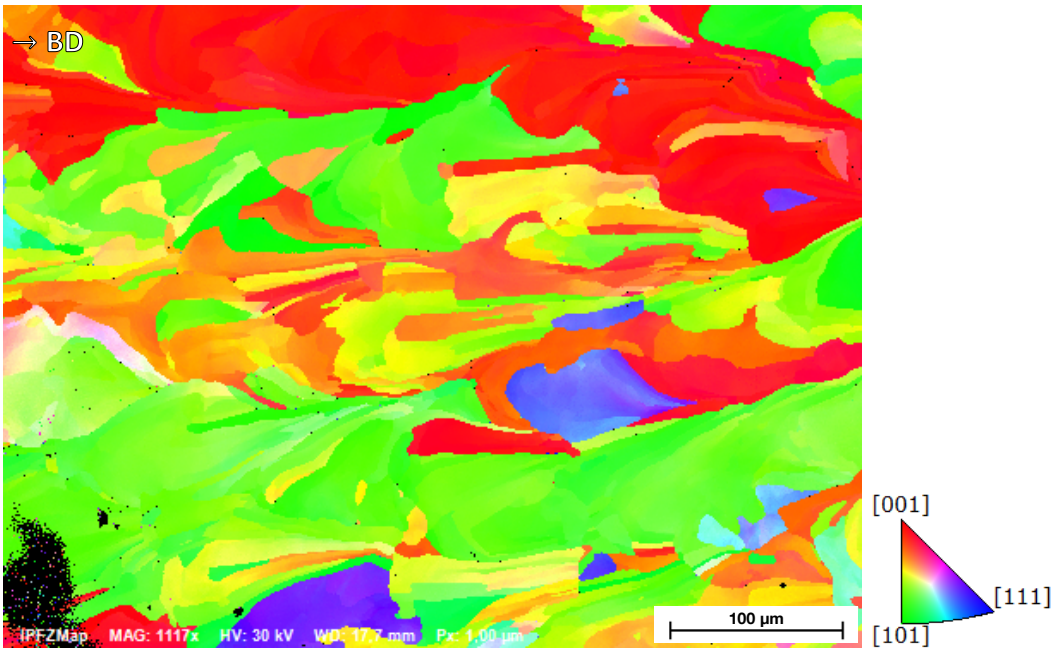

Figure 47: EBSD image of one FeSi3.5wt% sample made with PPP set N.

Additional EBSD measurements on samples made by more varying part process parameters would be needed to further verify this observed correlation between BD and magnetically favourable orientation.

4.5. Hardness Measurements

To ensure the conformity with all relevant hardness measurement standards, individual preliminary indents were made on an area of the LT cut sample half, which was further not used for data evaluation. It was found that one indent's diagonals are, on average in the range of 65 µm in length (figure 48a). This would require any neighbouring indents to be at least 165.5 µm apart from each other. To accommodate any hardness variations – and therefore elongation or shortening of the indent's diagonals – an equal distance of 180 µm was chosen for the hardness mapping (figure 48b). This mapping resulted, on average, in 200 indents per TV, and 80 indents per longitudinally cut sample part. While cross sections were tried to be fully covered by indents, the lengthwise cut fraction was covered from edge to edge in five rows of indents.

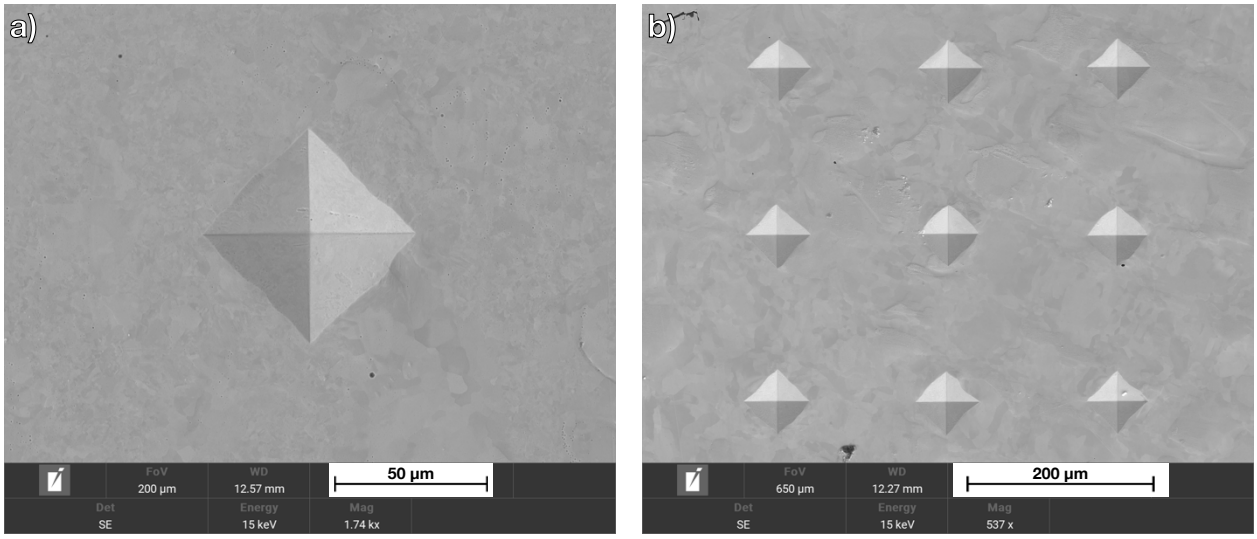

Figure 48: Vickers indents in Fe-Si. **a)** On average, d_{HV} is in the range of 65 µm (magnification: 1740x); **b)** Equally spaced indents after hardness mapping (magnification: 537x).

4.5.1. HV0.5 for FeSi1.5wt%

All mean HV0.5 values for transversally and LT cut FeSi1.5wt% samples are listed in table 15 and table 16, respectively. While PPP set N yielded the lowest hardness and smallest standard deviation for both cut orientations (TV: 177.69 ± 18.53 HV0.5; LT: 182.43 ± 7.39 HV0.5), the maximum HV0.5 were measured with PPP set P (199.91 ± 22.89 HV0.5) and O (195.93 ± 10.85 HV0.5) for the cross- and lengthwise cut, respectively.

Table 15: Measured hardness values (HV0.5) of TV cut FeSi1.5wt%.

v / P	800 mm/s	900 mm/s	1000 mm/s
175 W	184.58 ± 26.44	-	-
200 W	177.69 ± 18.53	188.58 ± 19.07	199.91 ± 22.89

Table 16: Measured hardness values (HV0.5) of LT cut FeSi1.5wt%.

v / P	800 mm/s	900 mm/s	1000 mm/s
175 W	195.57 ± 11.76	-	-
200 W	182.43 ± 7.39	195.93 ± 10.85	192.65 ± 15.09

The spatial resolution of all hardness indents could be made visible by virtue of the programmed python code. Figure 49 depicts the process: The sample is mapped with equidistantly spaced Vickers indents, which supply the program with the necessary hardness data and respective relative indent-coordinates to produce the corresponding hardness map.

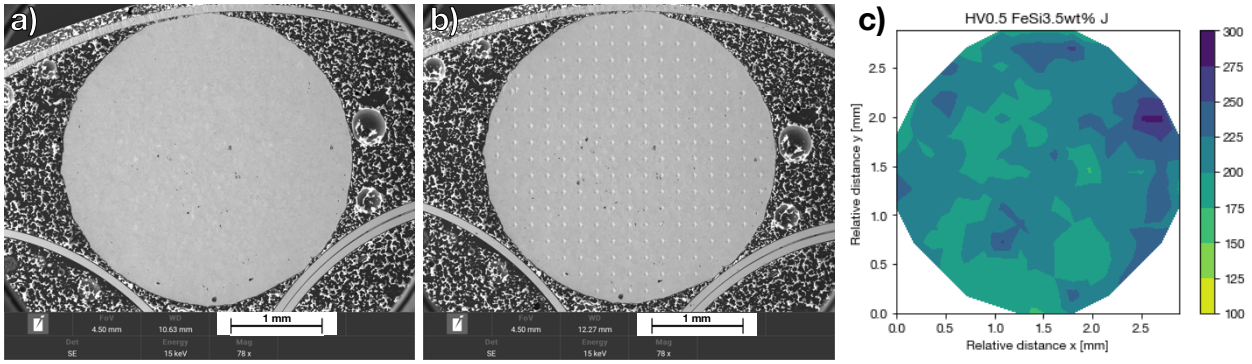

Figure 49: FeSi3.5wt% sample J at 78x magnification: **a)** before testing; **b)** after hardness mapping with – in this case – 220 Vickers indents and **c)** the resulting hardness map after data processing.

These maps, shown in figure 50 for FeSi1.5wt%, indicate a more consistent hardness distribution in both samples J and N, with only small areas at the border with significantly higher HV0.5 values. These areas become more pronounced in specimens O and P.

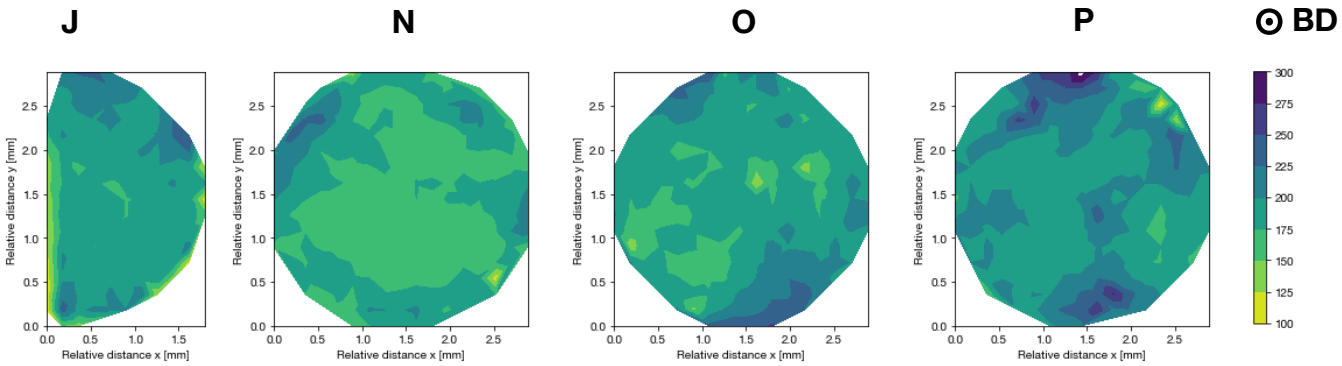

Figure 50: HV0.5 hardness maps for TV cut FeSi1.5wt%.

This is emphasized by the fact that the difference between the highest and lowest measured hardness values in these four TV cut samples is 110.0 HV0.5 for N and 213.0 HV0.5 for P (figure 50) sample being embedded too closely to the SEM sample's border, only one half of sample J could be used for this measurements, 144 data points could be included in the data evaluation.

The trend of more less fluctuating hardness values throughout the sample with a more moderate scanning speed of 800 mm/s, which was used for samples J and N, could also be made visible in the LT cut sample parts (figure 51). Here, the difference between the highest and lowest detected value was 37.0 HV0.5 for sample N, while the highest, could be measured in sample P (128.7 HV0.5). Nonetheless, no clear distinction between the hardness of contour-near regions or bulk regions could be made for all samples.

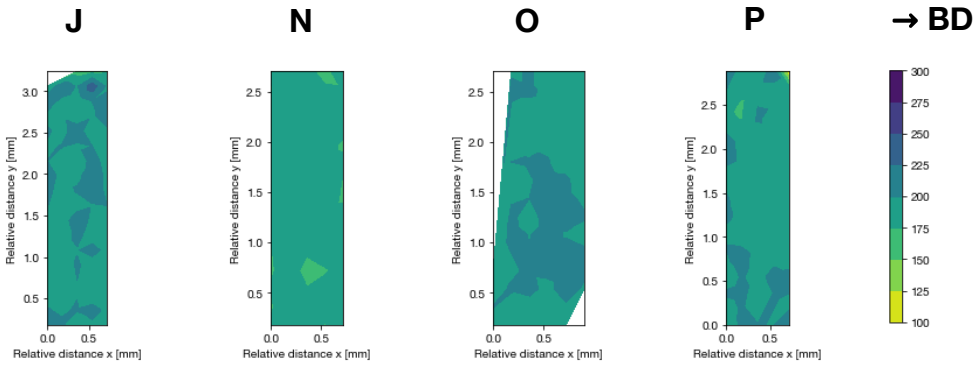

Figure 51: HV0.5 hardness maps for LT cut FeSi1.5wt%.

4.5.2. HV0.5 for FeSi3.5wt%

The same procedures were repeated with four FeSi3.5wt% samples, thus resulting in hardness values listed in table 17 and table 18 for transversally and longitudinally cut parts, respectively.

Table 17: Measured hardness values (HV0.5) of TV cut FeSi3.5wt%.

v / P	800 mm/s	900 mm/s	1000 mm/s
175 W	208.58 ± 18.53	-	-
200 W	200.00 ± 16.20	204.27 ± 16.29	213.71 ± 16.26

Table 18: Measured hardness values (HV0.5) of LT cut FeSi3.5wt%.

v / P	800 mm/s	900 mm/s	1000 mm/s
175 W	219.60 ± 13.78	-	-
200 W	217.84 ± 16.09	216.88 ± 16.54	213.54 ± 13.96

Although partially within the margin of standard deviation, averaged hardness values of FeSi3.5wt% surpassed those of FeSi1.5wt% samples. This was attributed to the alloy's higher Si content, thus experiencing an increased solution hardening effect.

The part process parameters that led to the most homogeneous hardness distribution was, once again, PPP set N, i.e. laser power of 200 W and a scanning speed of 800 mm/s, as can be seen in its relatively large areas of the same colour in figure 52. The difference between the highest and lowest hardness value was found to be – despite its more inhomogeneous hardness distribution – minimal in sample P (107.0 HV0.5) and maximal in sample O (144.0 HV0.5). Both values are well below the maximum of FeSi1.5wt%, thus suggesting a more stable process with this alloy.

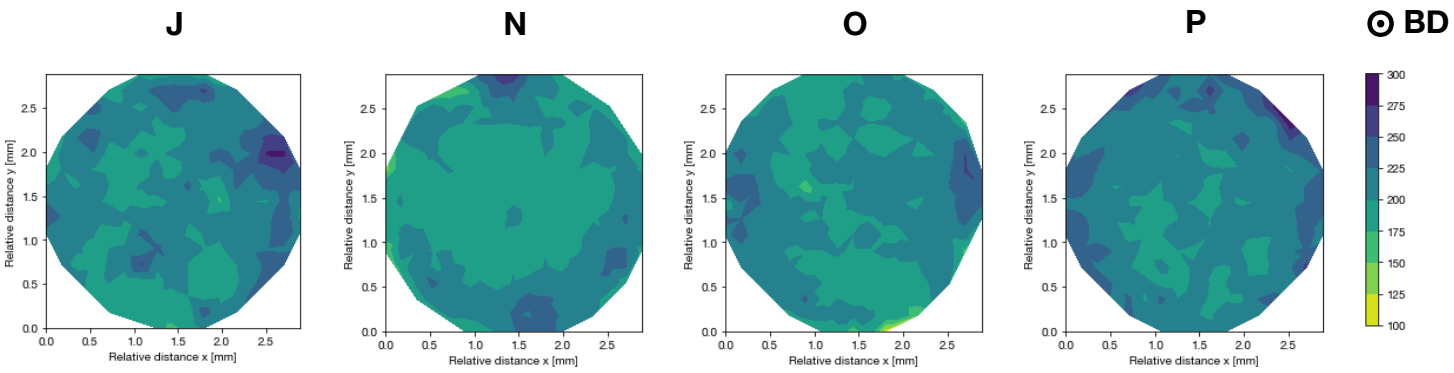

Figure 52: HV0.5 hardness maps for TV cut FeSi3.5wt%.

The investigation of longitudinally cut samples revealed more diverse hardness maps (figure 53) – possibly due to the fewer data points and smaller area covered by Vickers indents. Two samples, N and O, produced hardness distributions with more localized maxima and minima. The largest (102.0 HV0.5) and smallest (66.0 HV0.5) differences between the highest and lowest measured values were found in samples O and J, respectively.

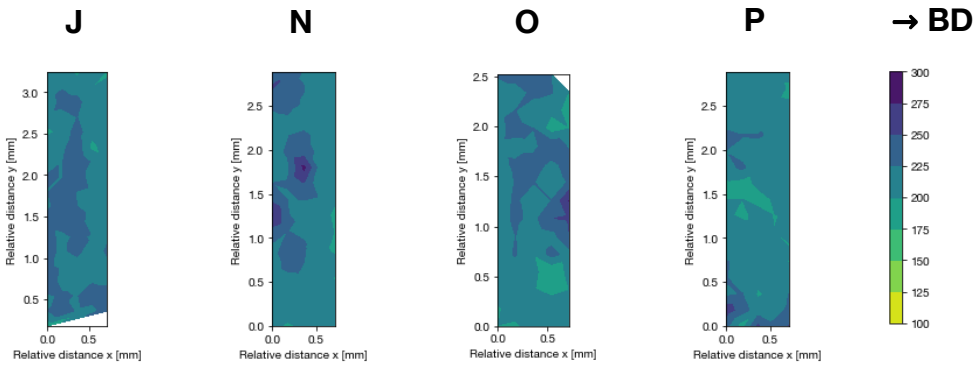

Figure 53: HV0.5 hardness maps for LT cut FeSi3.5wt%.

When directly compared, the consistently higher hardness of FeSi3.5wt% – indirectly proportionally decreasing with increasing energy densities – becomes apparent. Figure 54 emphasizes this observation by plotting the respective hardness values and energy densities with which each sample was manufactured. To further underline this, polynomial graphs were fitted to both data sets, where FeSi1.5wt% data is printed in blue dots and FeSi3.5wt% data in black squares. It is noteworthy to mention, that all measured hardness values are, according to Omura et al., well within range of

conventionally manufactured electrical steel, i.e. between 154 HV0.5 and 217 HV0.5 [59]. Additionally, no cracks formed at the Vickers indent's corners.

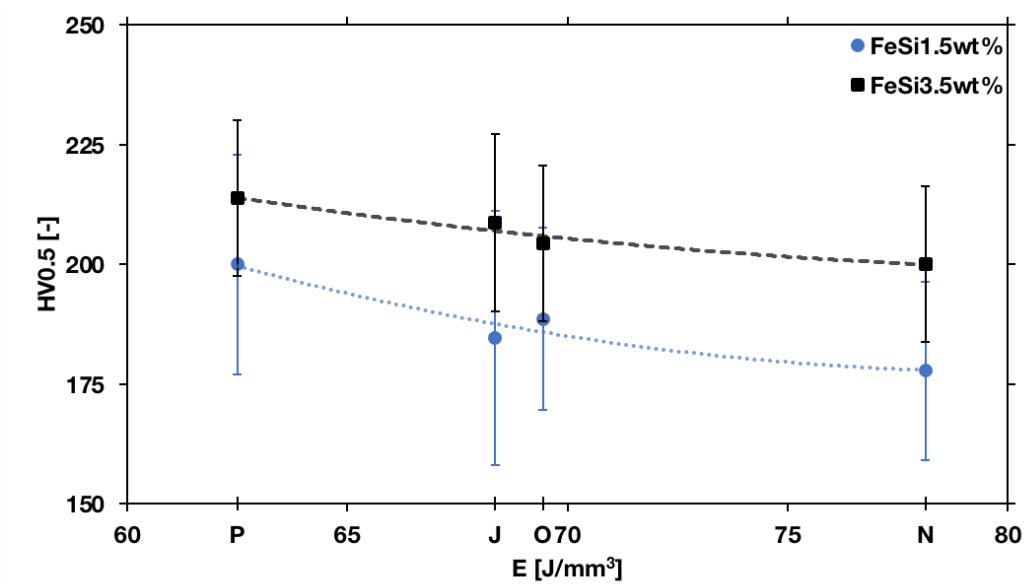

Figure 54: Hardness-energy density plot for TV cut FeSi1.5wt% (blue dots) and FeSi3.5wt% (black squares), manufactured with PPP sets P, J, O & N.

For this reason, one FeSi3.5wt% specimen (sample № 47) – made with P-v-combination N – was chosen to be magnetically tested for its hysteresis behaviour. Additionally, one strongly contrasting sample (№ 59), which was manufactured with the PPP set D (125 W and 1000 mm/s), was put to the same test using a hystograph.

4.6. Hysteresis Measurements

The two tested sample's dimensions (appendix 7.1.) and densities (appendix 7.2.) were entered into the software and carefully placed inside the requisite secondary coil frame. Before testing, each sample was temporarily secured in place with adhesive tape to ensure its concentric placement. This tape was removed after the clamping by both primary coil poles and thus the correct placement was assured. The subsequent test was repeated three times per sample, which was fully demagnetized and repositioned after each run. Furthermore, the secondary coils were re-calibrated after each test sequence. Figure 55 depicts the mean hysteresis loop for FeSi3.5wt% sample № 47. This specimen was manufactured using PPP set N and showed relatively low porosity (0.86 %).

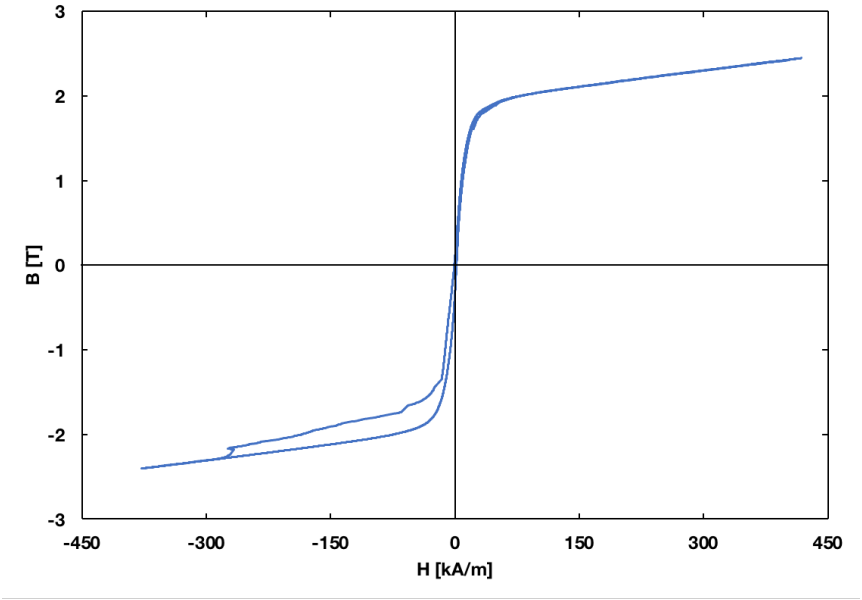

Figure 55: Mean B-H-curve of sample № 47 – manufactured with PPP set N.

The loop is widening significantly in the third and less so in the first quadrant due to measurement artifacts from the three curves. In this region, the hystograph's power supply switches its mode to reach stronger magnetic fields. These graph inconsistencies, as can be seen in appendix 7.5, can be found – more or less pronounced – in every measurement data set and emphasise the theoretically improper material for this experimental setup.

The relatively large span of roughly 800 kA/m for H in this graph is deceiving, as despite its seemingly narrow shape, which undoubtedly indicates a soft magnetic material, the

apparent mean coercivity of 875 A/m differs – by a factor of 67.8 – from the expected range of H_c for FeSi3.0 (12.9 A/m [23]). However, the three measurement's mean saturation flux density of 2.16 ± 0.05 T was found to be – contrary to the coercivity's high divergence from literature – more consistent with the reported values of 2.20 T for pure Fe and 1.50 T to 2.15 T for FeSi3.0, respectively [62, 63]. A zoomed-in view of all three B-H-curves for this specimen is shown in figure 56. There, the relatively low resolution due to the measurement system's limited data collection rate shows as roughness throughout the curves. Additionally, the second measurement's graph deviates from the other's curves. One rational reason for this behaviour could be sample misalignment during the repositioning prior to the measurement.

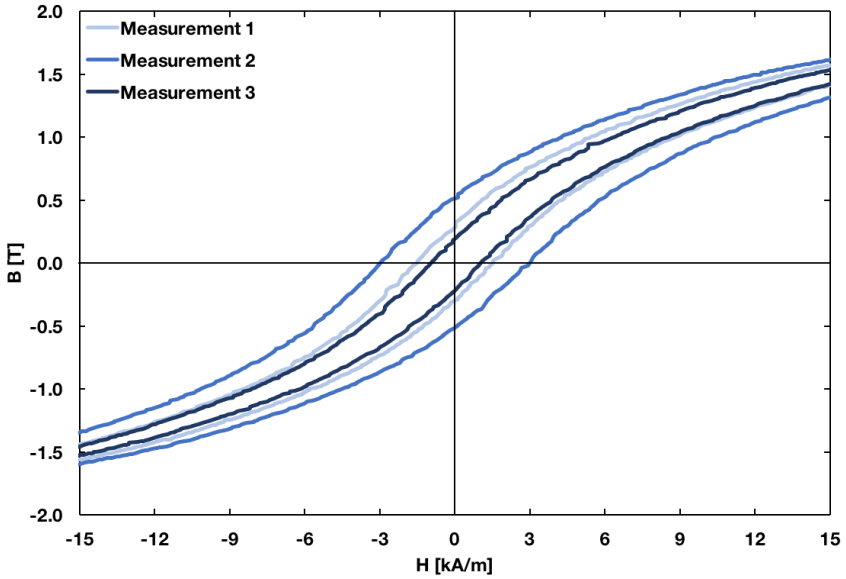

Figure 56: A more detailed view on the individual B-H-curves of sample № 47 (PPP set N).

FeSi3.5wt% sample № 59 was chosen as the second specimen to be magnetically tested. This cylinder was manufactured with P-v-combination D, i.e. the lowest resulting energy density investigated in this thesis. It was expected to yield measurably contrasting hysteresis loops because of its comparatively high porosity of 5.33 % and the therefore entrapped gas acting as nonmagnetic fluid, i.e. as "magnetic resistance". Figure 57 depicts the resulting mean B-H-curve. Albeit not as conspicuous, this graph is also widening in the first and third quadrant as a consequence of measurement artifacts. The calculated mean coercivity (1255 A/m) would even more strongly diverge, i.e. by a factor

of 97.3, from an expected value close to the literature for FeSi3.0. Despite this significantly higher discrepancy between the measured coercivity and any literature values, this same trend does not apply for B_s as distinctively, as the mean saturation flux density was found to be 2.04 ± 0.08 T – thus being only marginally smaller for the more porous sample № 59 than for the less porous № 47. However, also this value is in good agreement with the reported literature for Fe and FeSi3.0 [62, 63].

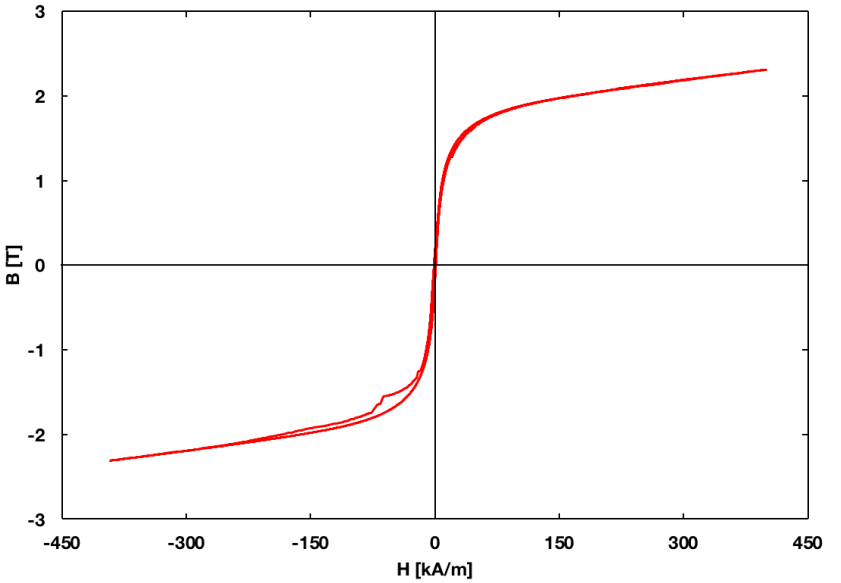

Figure 57: Mean B-H-curve of sample № 59 – manufactured with PPP set D.

Figure 58 indicates more proficient sample handling, which consequently clearly leads to more consistent B-H-curves. However, the graphs still show the aforementioned roughness due to a relatively low data collection rate, which is – of course – adjusted to the requirements of hard magnetic material testing.

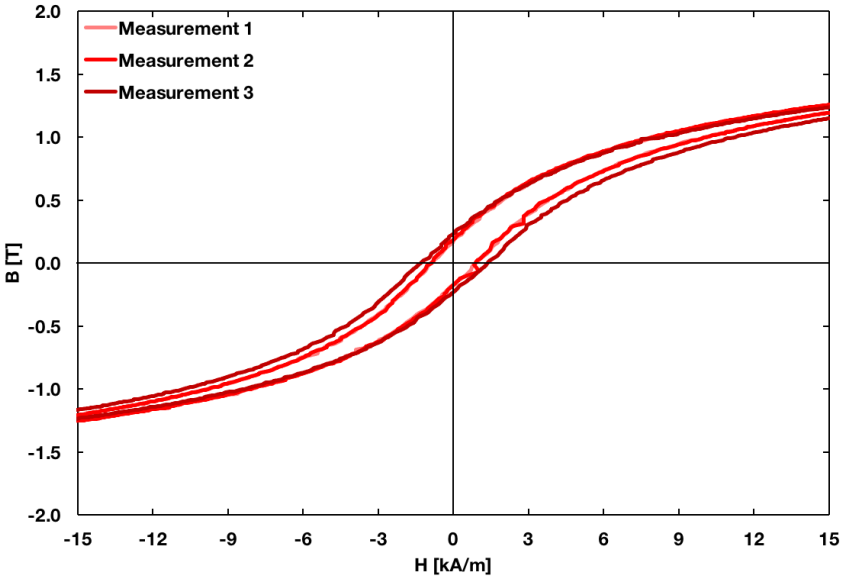

Figure 58: A more detailed view on the individual B-H-curves of sample № 59 (PPP set D).

Due to the lack of equipment according to the relevant standard, which would undoubtedly yield correctly measured coercivities, no comprehensive magnetic testing regime on all manufactured samples could be performed. Therefore, the qualitative comparison of one sample with relatively high and one sample with relatively low porosity for alloy FeSi3.5wt% and its implications for the influence of process parameters on final magnetic performance must suffice.

5. Conclusions

This thesis shows the feasibility of laser powder bed fusion to produce soft magnetic ferrosilicon parts, which are integral parts of electric motors and generators. Since conventional manufacturing processes restrict the final product's form factor and feature dimensions, additive manufacturing offers a more advanced approach due to its fundamentally different from-bottom-to-top construction principle. This may be the foundation for lighter machines, while still providing comparable or even surpassing power outputs, i.e. more efficient electric motors and generators. A desirable goal in a world of ever-increasing electric appliances and electricity demand.

In the conducted LPBF parameter study, two strongly impacting criteria, the laser power and the laser scanning speed were varied between 125 W to 200 W and from 700 mm/s to 1000 mm/s, respectively. Four cylindrical samples of 3 mm in diameter and 6 mm in height were manufactured per each of the resulting energy densities with which the specimens would be made. This yielded a total of 128 samples, as two different Fe-based alloys, one with 1.5 wt% and one with 3.5 wt% Si added to the main element, were investigated. Following the sample production and necessary post processing, each sample's density, i.e. porosity, was determined by virtue of the Archimedes method.

Furthermore, four samples with relatively low porosities were chosen per alloy to be examined in a SEM regarding their porosity distribution. These analyses revealed more favourable energy densities that led to small pores that appeared mainly in the sample's contour region and were probably caused by ineptly chosen additional process parameters such as the hatching distance or contour offset. Concluding the SEM measurements, two EBSD experiments were performed on two samples, one per alloy, that were manufactured using the identical process parameters of 200 W laser power and 800 mm/s scanning speed. This analysis revealed a clear correlation between building direction and orientation of magnetically soft crystallographic axes in the FeSi3.5wt% sample. However, no such clear relationship could be found for FeSi1.5wt%. Nonetheless, this key insight of building direction dependent grain

orientation may prospectively play a major role for the additive manufacturing of FeSi soft magnetic parts.

Low force Vickers hardness tests were conducted to further characterize the eight, based on their low porosities, chosen specimens. To investigate, if the measured HV0.5 hardness shows any location dependency that might indicate possible starting points for crack forming, hardness maps were created by equally spacing Vickers indent positions across the cut surfaces and automatically test each sample. The thusly created data was analysed with a small python script and processed into hardness heat maps to visualize any hardness inconsistencies throughout the specimens.

Following the mechanical testing routine, two FeSi3.5wt% samples were magnetically tested in a hystograph, which produced qualitatively comparable hysteresis loops. Since this experimental setup is intended for hard magnets no quantitatively significant data could be produced. However, these B-H-curves indicate a higher coercivity, i.e. “magnetic hardness”, for samples with lower porosities and vice versa, thus confirming the to be expected correlation of porosity and coercivity.

Finally, based on the gathered data, an idealized set of PPPs for a possible next iteration of experiments could be defined: Since both alloy’s lowest porosities were obtained with similar P-v-combinations for FeSi1.5wt% FeSi3.5wt%, a compromise was made to define 800 mm/s as best suited regarding the scanning speed. The fixing of this value made it possible to calculate the theoretically needed laser power for the lowest achievable porosities by deviating quadratic fit functions for alloy-specific porosity-energy density graphs. FeSi1.5wt%, having a higher melting point (T_m) of roughly 1533 °C [9] would therefore require an input of 195.1 W and FeSi3.5wt% (T_m of roughly 1510 °C [9]) one of 185.8 W resulting in energy densities of 76.2 J/mm^3 and 72.6 J/mm^3, respectively.

6. References

[1] W. D. Callister, D. G. Rethwisch, "Materials science and engineering: An introduction", *John Wiley & Sons*, New York, 2011, pp. 775-777.

[2] M. D. Coey, "Magnetism and magnetic materials", *Cambridge University Press*, Cambridge, 2010, pp. 8-10.

[3] O. Gutfleisch, M. A. Willard, E. Brück, et. al, Magnetic Materials and Devices for the 21st Century: Stronger, Lighter, and More Energy Efficient, *Advanced Materials* 23 (2011) pp. 832-836, doi: 10.1002/adma.201002180.

[4] P. Biermayr, C. Dißauer, M. Eberl, et. al, "Innovative Energietechnologien in Österreich – Marktentwicklung 2019", https://nachhaltigwirtschaften.at/resources/iea_pdf/schriftenreihe-2020-14-marktstatistik-2019-bf.pdf, July 2022.

[5] Statista GmbH, "Dossier on electromobility", https://de.statista.com/statistik/studie/id/43860/dokument/elektromobilitaet-in-oesterreich-statista-dossier, August 2022.

[6] N. A. Spaldin, "Magnetic Materials: Fundamentals and Applications", Cambri*dge University Press*, Cambridge, 2011, pp. 65-154.

[7] G. Engdhal, "Handbook Of Electrical Steel", *World Scientific Publishing Company*, Singapore, 2021, pp. 285-297.

[8] F. González, Y. Houbaert, A review of ordering phenomena in iron-silicon alloys, *Revista de Metallurgia* 49 (2013), pp. 178-199, doi: 10.3989/revmetalm.1223.

[9] M. Gasik, L. Holappa, M. Tangstad, et. al, "Handbook of Ferroalloys – Theory and Technology", *Butterworth-Heinemann*, Oxford, 2013, pp. 3-286.

[10] G. Stornelli, F. A. Di Schino, P. Folgarait, et. al, Properties of Additively Manufactured Electric Steel Powder Cores with Increased Si Content, *Materials* 14 (2021) pp. 1489-17, doi: 10.3390/ma14061489.

[11] B. C. Sales, O. Delaire, M. A. McGuire, A. F. May, Thermoelectric properties of Co-, Ir-, and Os-doped FeSi alloys: Evidence for strong electron-phonon coupling, Phys*ical Review B* 83 (2011), pp. 125209-7, doi: 10.1103/PhysRevB.83.125209.

[12] C. M. Hurd, Varieties of magnetic order in solids, *Contemporary Physics* 23 (1982), pp. 469-493, doi: 10.1080/00107518208237096.

[13] N. W. Ashcroft, N. D. Mermin, "Festkörperphysik", *Oldenbourg*, Munich, 2013, pp. 883-923.

[14] W. Heisenberg, Mehrkörperproblem und Resonanz in der Quantenmechanik, *Zeitschrift für Physik* 38 (1926) pp. 411-426, doi: 10.1007/BF01397160.

[15] D. Kriegner, H. Reichlova, J. Grenzer, et. al, Magnetic anisotropy in antiferromagnetic hexagonal MnTe, *Physical Review B* 96 (2017) p. 214418-8, doi: 10.1103/PhysRevB. 96.214418.

[16] M. V. Mamonova, M. Yu. Makeev, D. S. Kalinin, A. A. Zenova, First-principles Calculations of Magnetic Anisotropy of Fe and Co Films Separated by Nonmagnetic Metallic Interlayers, *Physics of the Solid State* 64 (2022) pp. 56–63, doi: 10.1134/ S1063783422010127.

[17] R. C. O'Handley, "Modern Magnetic Materials: Principles and Applications", *John Wiley & Sons*, New York, 2000, pp. 179-215.

[18] R. A. Serway, R. J. Beichner, J. W. Jewett, "Physics for Scientists and Engineers", *Saunders College Publishing*, Philadephia, 2000, p. 963.

[19] F. C. Campbell, "Elements of Metallurgy and Engineering Alloys", *ASM International*, Novelty, 2008, p. 557.

[20] S. Valeri, S. Altieri, P. Luches, L. Duò (ed.) et al., "Magnetic Properties of Antiferromagnetic Oxide Materials: Surfaces, Interfaces, and Thin Films", *Wiley-VCH*, Weinheim, 2010, pp. 25-68.

[21] B. Fegley (ed.), "Practical Chemical Thermodynamics for Geoscientists", *Academic Press*, Cambridge, 2013, pp. 81-125.

[22] C. Wu, J. Jin, "Frontiers in Magnetic Materials: From Principles to Material Design and Practical Applications", *CRC Press*, Boca Ranton, 2023, pp. 16-27.

[23] D. R. Lide (ed.), "CRC Handbook of Chemistry and Physics", *CRC Press*, Boca Raton, 2005, p. 2198.

[24] J. F. Schenck, The role of magnetic susceptibility in magnetic resonance imaging: MRI magnetic compatibility of the first and second kinds, *Medical Physics* 23 (1996), pp. 815-850, doi: doi.org/10.1118/1.597854.

[25] T. Narayanan, M. Shaijumon, P. Ajayan, et al., Synthesis of High Coercivity Core–Shell Nanorods Based on Nickel and Cobalt and Their Magnetic Properties, *Nanoscale Research Letters* 5 (2010), pp. 164-168, doi: 10.1007/s11671-009-9459-7.

[26] ISO/ASTM 52900:2021, Additive manufacturing - General principles - Fundamentals and vocabulary, April 2023.

[27] Jamie D., "A Comprehensive List of All the Metal 3D Printer Manufacturers", https://www.3dnatives.com/en/metal-3d-printer-manufacturers, April 2023.

[28] E. Toyserkani, D. Sarker, O. O. Ibhadode, et al., "Metal Additive Manufacturing", *John Wiley & Sons*, New York, 2022, pp. 32-41, 65-76, 206-254.

[29] K. R. Balasubramanian, V. Senthilkumar (eds.), "Additive Manufacturing Applications for Metals and Composites", *IGI Global*, Pennsylvania, 2020, pp. 1-24, 249-270.

[30] D. Godec, J. Gonzalez-Gutierrez, A. Nordin et al., "A Guide to Additive Manufacturing", *Springer Nature Switzerland AG*, Cham, 2022, pp. 252-290.

[31] A. B. Spierings, N. Herres, G. Levy, Influence of the particle size distribution on surface quality and mechanical properties in AM steel parts, *Rapid Prototyping Journal* 17 (2011), pp. 195-202, doi: 10.1108/13552541111124770.

[32] M. Habibnejad-korayem, J. Zhang, Y. Zou, Effect of particle size distribution on the flowability of plasma atomized Ti-6Al-4V powders, *Powder Technology* 392 (2021), pp. 536-543, doi: 10.1016/j.powtec.2021.07.026.

[33] V. Griffiths, J. P. Scanlan, M. H. Eres, et al., Cost-driven build orientation and bin packing of parts in Selective Laser Melting (SLM), *European Journal of Operational Research* 273 (2019), pp. 334-352, doi: 10.1016/j.ejor.2018.07.053.

[34] C. Y. Yap, C. K. Chua, Z. L. Dong, et al., Review of selective laser melting: Materials and applications, *Applied Physics Reviews* 2 (2015), p. 41101-22, doi: 10.1063/1.4935926.

[35] O. O. Salman, F. Brenne, T. Niendorf, et al., Impact of the scanning strategy on the mechanical behavior of 316L steel synthesized by selective laser melting, *Journal of*

Manufacturing Processes 45 (2019), pp. 255-261, doi: doi.org/10.1016/j.jmapro. 2019.07.010.

[36] H. Roiranda, B. Malarda, A. Horb, N. Saintierc, Effect of laser scan pattern in laser powder bed fusion process: The case of 316L stainless steel, *Procedia Structural Integrity* 38 (2022), pp. 149-158, doi: 10.1016/j.prostr.2022.03.016.

[37] J. Robinson, I. Ashton, P. Fox, et al., Determination of the effect of scan strategy on residual stress in laser powder bed fusion additive manufacturing, *Additive Manufacturing* 23 (2018), pp. 13-24, doi: 10.1016/j.addma.2018.07.001.

[38] M. Shao, S. Vijayan, P. Nandwana, et al., The effect of beam scan strategies on microstructural variations in Ti-6Al-4V fabricated by electron beam powder bed fusion, *Materials & Design* 196 (2020), p. 109165-16, doi: 10.1016/j.matdes.2020.109165.

[39] H. Fayazfar, M. Salarian, A. Rogalsky, et al., A critical review of powder-based additive manufacturing of ferrous alloys: Process parameters, microstructure and mechanical properties, *Materials & Design* 144 (2018), pp. 98–128, doi: 10.1016/j.matdes. 2018.02.018.

[40] K. S. Ramani, C. He, Y. L. Tsai, et al., SmartScan: An intelligent scanning approach for uniform thermal distribution, reduced residual stresses and deformations in PBF additive manufacturing, *Additive Manufacturing* 52 (2022), p. 102643-13, doi: 10.1016/j.addma. 2022.102643.

[41] u/todwod, "3D printed stainless steel made with a 'Matsuura Lumex Avance 25' with CNC milling capabilities. Flash drive for scale", https://www.reddit.com/r/3Dprinting/comments/ay3d8f/3d_printed_stainless_steel_made_with_a_matsuura, April 2023.

[42] P. Rasilo, U. Aydin, T. P. Holopainen, A. Arkkio, Analysis of iron losses on the cutting edges of induction motor core laminations, *XXII International Conference on Electrical Machines* (2016), Lausanne, pp. 1312-1317, doi: 10.1109/ICELMACH.2016.7732694.

[43] ImageJ, "Image Processing and Analysis in Java", https://imagej.net/software/imagej, May 2023.

[44] Autodesk Inc., "Fusion 360 with Netfabb features", https://www.autodesk.com/products/netfabb/features, April 2023.

[45] M. C. Sow, T. de Terris, O. Castelnau, et al., Influence of beam diameter on Laser Powder Bed Fusion (L-PBF) process, *Additive Manufacturing* 36 (2020), pp. 1-11, doi: 10.1016/j.addma.2020.101532.

[46] Aconity GmbH, "Aconity MIDI+ - Technical Specifications", https://configurator.aconity3d.com/storage/documents/configurator-machines/gxPFMisXKEtzchm0/AconityMIDI+_2022.pdf, April 2023.

[47] X. Ni, D. Kong, W. Wu, et al., Corrosion Behavior of 316L Stainless Steel Fabricated by Selective Laser Melting Under Different Scanning Speeds, *Journal of Materials Engineering and Performance* 27 (2018), pp. 3667–3677, doi: 10.1007/s11665-018-3446-z.

[48] J. Saewe, N. Carstensen, P. Kürnsteiner, et al., Influence of increased carbon content on the processability of high-speed steel HS6-5-3-8 by laser powder bed fusion, *Additive Manufacturing* 46 (2021), pp. 102125-11, doi: 10.1016/j.addma.2021.102125.

[49] Kulzer GmbH, "Accessories Embedding Systems Histology", https://kulzer-technik.com/en-kt/en-kt/products/accessories-embedding-systems-histology.html, May 2023.

[50] University of Wollongong Australia, "Struers LaboPol – Product Brochure", https://documents.uow.edu.au/content/groups/public/@web/@aiim/documents/doc/uow155164.pdf, May 2023.

[51] M. W. Barsoum, "Fundamentals of Ceramics", *Institute of Physics Publishing*, London, 2003, p. 79.

[52] M. Bengisu, "Engineering Ceramics", *Springer*, Berlin Heidelberg, 2001, pp. 363-365.

[53] C. J. Kong, C. J. Tuck, I. A. Ashcroft, et al., High density TI6AL4V via SLM processing: Microstructure and mechanical properties, *Proceedings of the 22nd Annual International Solid Freeform Fabrication Symposium* (2011), pp. 475-483, doi: 10.26153/tsw/15309.

[54] EN ISO 6507, Metallic materials — Vickers hardness test, May 2023.

[55] ASTM E384, Standard Test Method for Microindentation Hardness of Materials, May 2023.

[56] Zwick/Roell GmbH & Co. KG, "Product information – DuraScan G5 fully-automated hardness testing machine (0.25 gf - 62.5 kgf) DuraScan 50 G5, 70 G5, 80 G5", https://www.zwickroell.com/fileadmin/content/Files/SharePoint/user_upload/PI_EN/15_186_DSG5_fully_automatic_PI_EN.pdf, May 2023.

[57] Eurofins Qualitech AG - Swiss institute for interlaboratory proficiency, "Vickers Hardness Testing", https://swissproficiency.com/en/product/vickers, May 2023.

[58] DIN EN 60404-2, Magnetic materials - Part 2: Methods of measurement of the magnetic properties of electrical steel strip and sheet by means of an Epstein frame, May 2023.

[59] Holmarc Opto-Mechatronics Ltd., "B-H-Curve / Magnetic – Hysteresis Curve Experiment Model HO-ED-EM-09", https://www.holmarc.com/B-H_curve_experiment .php, May 2023.

[60] E. Steingroever, G. Ross, "Messverfahren der Magnettechnik", *Magnet-Physik Dr. Steingroever GmbH*, Cologne, 2016, pp. 55-57.

[61] T. Omura, Y. Zaizen, M. Fukumura, et al., Effect of Hardness and Thickness of Nonoriented Electrical Steel Sheets on Iron Loss Deterioration by Shearing Process, *IEEE Transactions on Magnetics* 51-11 (2015), pp. 1-4, doi: 10.1109/TMAG. 2015.2443176.

[62] R. C. O'Handley, R. A. Meyers (ed.), “Encyclopedia of Physical Science and Technology (Third Edition) - Magnetic Materials”, *Academic Press*, Cambridge, 2003, pp. 919-944.

[63] T. N. Lamichhane, L. Sethuraman, A. Dalagan, et al., Additive manufacturing of soft magnets for electrical machines – a review, *Materials Today Physics* 15 (2020), pp. 100255-23, doi: 10.1016/j.mtphys.2020.100255.

7. List of Figures

8. List of Tables

9. Appendix

9.1. Sample Dimensions

9.1.1. FeSi1.5wt%

Energy Density	Sample № [-]	Ø [mm]	h [mm]
A	25	3.20	5.69
	57	3.20	5.69
	17	3.20	5.68
	49	3.21	5.69
B	26	3.21	6.00
	58	3.21	5.90
	41	3.19	6.00
	9	3.20	6.03
C	1	3.19	6.17
	18	3.19	6.13
	33	3.19	6.10
	50	3.21	5.97
D	27	3.18	6.11
	10	3.20	6.06
	42	3.19	6.11
	59	3.19	6.05
E	2	3.19	6.09
	19	3.21	6.09
	34	3.19	6.11
	51	3.21	6.13
F	28	3.21	6.09
	11	3.21	6.08
	43	3.20	6.05
	60	3.19	6.08
G	3	3.20	6.17
	20	3.20	6.21
	35	3.19	6.22
	52	3.20	6.05
H	29	3.19	6.28
	61	3.19	6.35
	12	3.20	6.25
	44	3.20	6.22

Energy Density	Sample № [-]	Ø [mm]	h [mm]
I	4	3.21	6.04
	21	3.22	6.08
	36	3.22	6.15
	53	3.20	6.13
J	30	3.22	6.07
	45	3.21	6.05
	13	3.22	6.00
	62	3.20	6.02
K	5	3.22	6.07
	22	3.21	6.11
	37	3.19	6.09
	54	3.21	6.08
L	31	3.21	6.01
	63	3.22	6.03
	14	3.21	6.05
	46	3.20	5.95
M	6	3.21	6.00
	23	3.22	6.03
	38	3.22	6.01
	55	3.22	5.82
N	32	3.24	5.98
	64	3.23	6.00
	15	3.21	6.02
	47	3.23	5.99
O	7	3.19	6.01
	24	3.22	5.97
	39	3.21	5.96
	56	3.23	5.99
P	16	3.23	5.93
	48	3.24	5.97
	8	3.24	5.94
	40	3.24	5.89

9.1.2. FeSi3.5wt%

Energy Density	Sample № [-]	Ø [mm]	h [mm]
A	25	3.19	5.94
	57	3.22	5.89
	17	3.20	5.92
	49	3.20	5.94
B	26	3.21	5.92
	58	3.23	5.99
	41	3.20	6.06
	9	3.21	6.01
C	1	3.23	6.07
	18	3.21	6.11
	33	3.20	6.04
	50	3.23	6.01
D	27	3.18	6.12
	10	3.19	6.13
	42	3.20	6.17
	59	3.20	6.14
E	2	3.23	5.93
	19	3.22	6.06
	34	3.24	6.13
	51	3.21	6.09
F	28	3.22	6.05
	11	3.21	6.08
	43	3.22	6.08
	60	3.21	6.06
G	3	3.20	6.00
	20	3.20	6.07
	35	3.22	6.12
	52	3.22	6.02
H	29	3.21	6.01
	61	3.20	6.07
	12	3.21	6.10
	44	3.23	6.05

Energy Density	Sample № [-]	Ø [mm]	h [mm]
I	4	3.24	6.06
	21	3.22	6.08
	36	3.24	6.05
	53	3.22	6.09
J	30	3.22	6.03
	45	3.24	6.13
	13	3.22	6.10
	62	3.21	6.03
K	5	3.21	6.10
	22	3.21	6.10
	37	3.24	6.11
	54	3.23	6.08
L	31	3.21	6.02
	63	3.21	6.08
	14	3.24	6.05
	46	3.23	6.02
M	6	3.27	5.93
	23	3.24	5.93
	38	3.22	5.91
	55	3.25	5.88
N	32	3.25	5.95
	64	3.26	5.98
	15	3.24	5.95
	47	4.23	5.93
O	7	3.21	6.01
	24	3.24	6.01
	39	3.21	6.02
	56	3.25	6.03
P	16	3.26	6.01
	48	3.26	6.11
	8	3.21	6.08
	40	3.24	6.00

9.2. Porosity Measurements

9.2.1. FeSi1.5wt%

Energy Density	Sample № [-]	ρ [g/cm³]	Π [%]
A	25	7.541	2.97
	57	7.442	4.25
	17	7.569	2.61
	49	7.527	3.15
B	26	7.545	2.92
	58	7.477	3.80
	41	7.500	3.50
	9	7.538	3.02
C	1	7.547	2.90
	18	7.551	2.85
	33	7.606	2.13
	50	7.512	3.35
D	27	7.433	4.36
	10	7.439	4.28
	42	7.412	4.63
	59	7.358	5.33
E	2	7.614	2.04
	19	7.682	1.16
	34	7.642	1.68
	51	7.618	1.98
F	28	7.599	2.22
	11	7.572	2.58
	43	7.614	2.03
	60	7.510	3.38
G	3	7.646	1.62
	20	7.632	1.81
	35	7.619	1.96
	52	7.618	1.99
H	29	7.559	2.74
	61	7.606	2.13
	12	7.623	1.91
	44	7.608	2.11

Energy Density	Sample № [-]	ρ [g/cm³]	Π [%]
I	4	7.627	1.87
	21	7.642	1.67
	36	7.678	1.21
	53	7.662	1.42
J	30	7.636	1.75
	45	7.656	1.50
	13	7.676	1.24
	62	7.637	1.74
K	5	7.619	1.97
	22	7.657	1.48
	37	7.653	1.54
	54	7.646	1.63
L	31	7.666	1.36
	63	7.603	2.17
	14	7.675	1.25
	46	7.654	1.52
M	6	7.639	1.71
	23	7.619	1.97
	38	7.658	1.46
	55	7.621	1.94
N	32	7.541	1.69
	64	7.442	1.35
	15	7.569	1.49
	47	7.527	1.28
O	7	7.541	2.02
	24	7.442	1.17
	39	7.569	1.39
	56	7.527	1.97
P	16	7.541	1.59
	48	7.442	1.39
	8	7.569	1.95
	40	7.527	1.64

9.2.2. FeSi3.5wt%

Energy Density	Sample № [-]	ρ [g/cm^3]	Π [%]
A	25	7.576	1.02
	57	7.453	2.62
	17	7.515	1.82
	49	7.462	2.50
B	26	7.459	2.55
	58	7.321	4.35
	41	7.366	3.77
	9	7.458	2.56
C	1	7.391	3.43
	18	7.396	3.38
	33	7.347	4.01
	50	7.301	4.61
D	27	7.356	3.89
	10	7.361	3.83
	42	7.276	4.94
	59	7.237	5.45
E	2	7.591	0.83
	19	7.562	1.20
	34	7.554	1.31
	51	7.571	1.08
F	28	7.558	1.26
	11	7.597	0.75
	43	7.570	1.10
	60	7.558	1.26
G	3	7.608	0.60
	20	7.569	1.11
	35	7.543	1.45
	52	7.563	1.19
H	29	7.571	1.08
	61	7.540	1.49
	12	7.597	0.74
	44	7.568	1.13

Energy Density	Sample № [-]	ρ [g/cm^3]	Π [%]
I	4	7.608	0.60
	21	7.569	1.11
	36	7.579	0.98
	53	7.554	1.30
J	30	7.606	0.63
	45	7.591	0.82
	13	7.579	0.98
	62	7.597	0.74
K	5	7.582	0.94
	22	7.602	0.68
	37	7.603	0.67
	54	7.610	0.57
L	31	7.564	1.18
	63	7.449	2.68
	14	7.591	0.82
	46	7.535	1.55
M	6	7.559	1.24
	23	7.543	1.45
	38	7.563	1.19
	55	7.601	0.69
N	32	7.573	1.06
	64	7.562	1.20
	15	7.605	0.64
	47	7.588	0.86
O	7	7.575	1.04
	24	7.588	0.86
	39	7.586	0.89
	56	7.524	1.69
P	16	7.593	0.80
	48	7.532	1.60
	8	7.559	1.24
	40	7.535	1.55

9.3. SEM Micrographs

9.3.1. FeSi1.5wt%

Transversal cut of sample J: 175 W and 800 mm/s

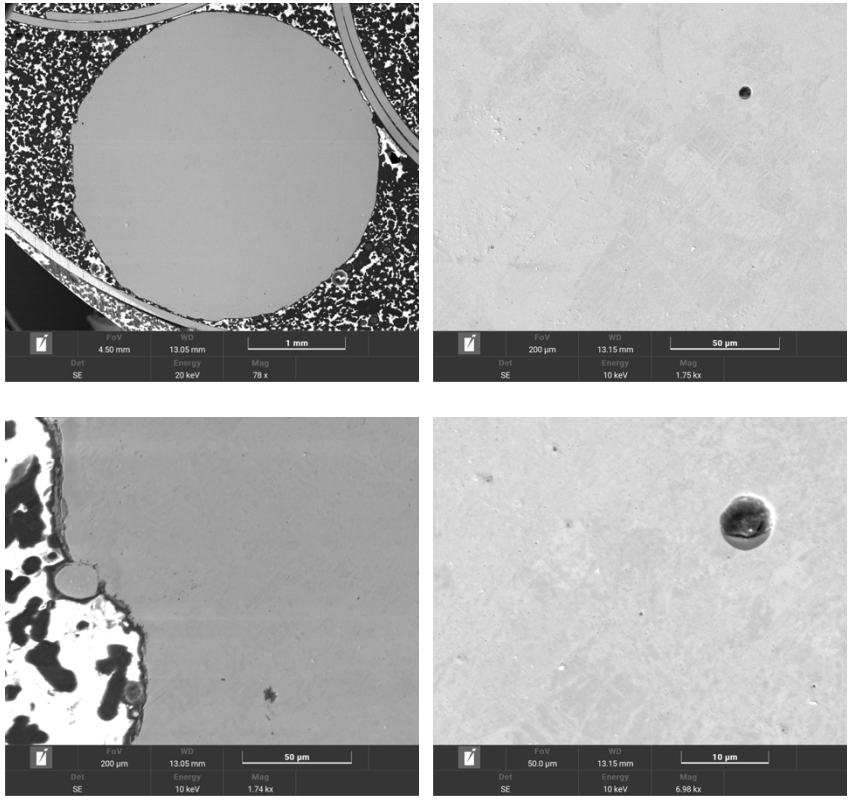

⊙ **BD**

Longitudinal cut of sample J: 175 W and 800 mm/s

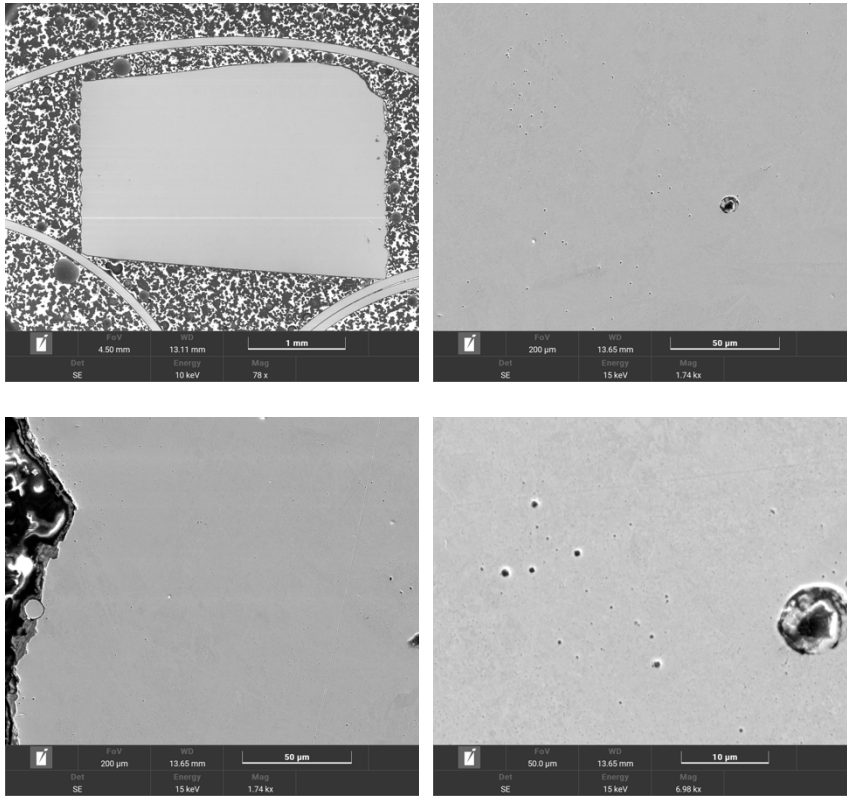

↓ **BD**

Top left: full cut sample; top right: zoomed-in view on center area;

bottom left: zoomed-in view on border area; bottom right: further zoomed-in view on center area.

Transversal cut of sample N: 200 W and 800 mm/s

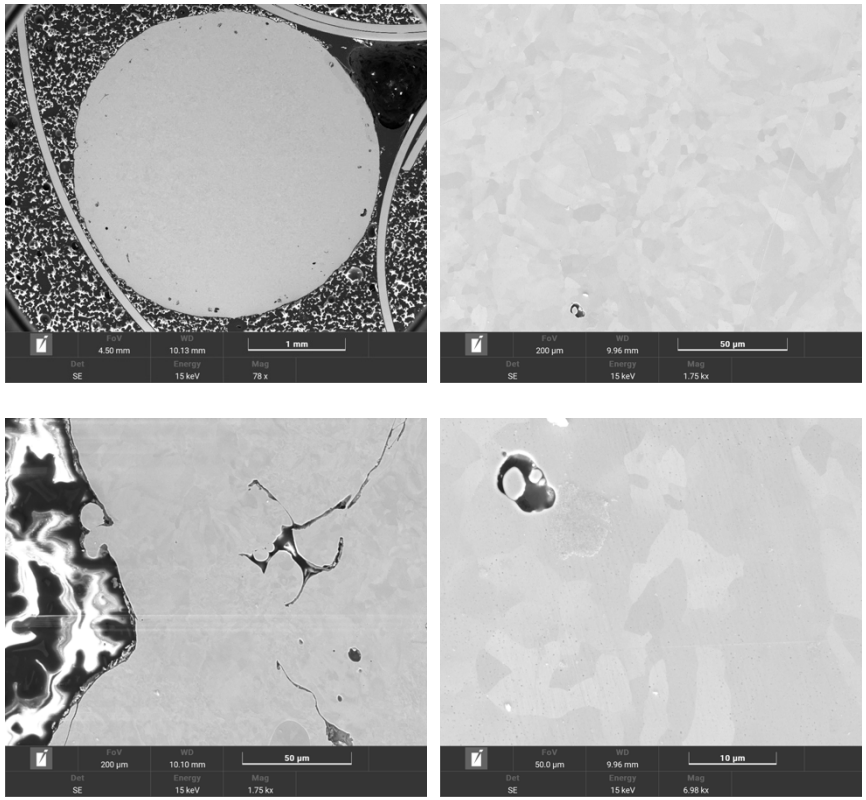

Longitudinal cut of sample N: 200 W and 800 mm/s

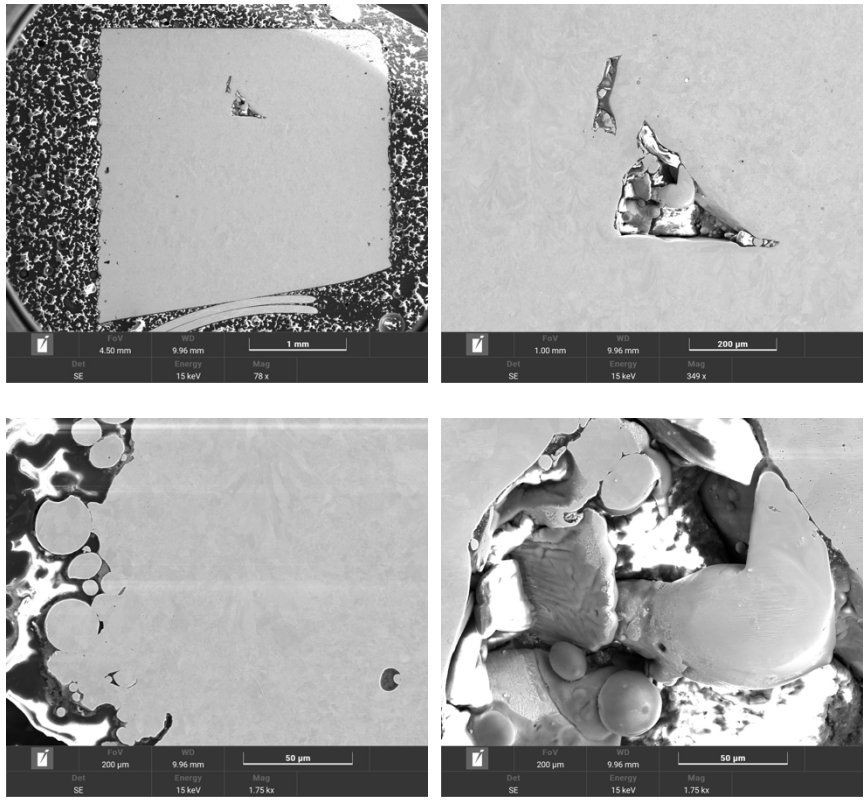

⊙ **BD**

↑ **BD**

Top left: full cut sample; top right: zoomed-in view on center area;

bottom left: zoomed-in view on border area; bottom right: further zoomed-in view on center area.

Transversal cut of sample O: 200 W and 900 mm/s

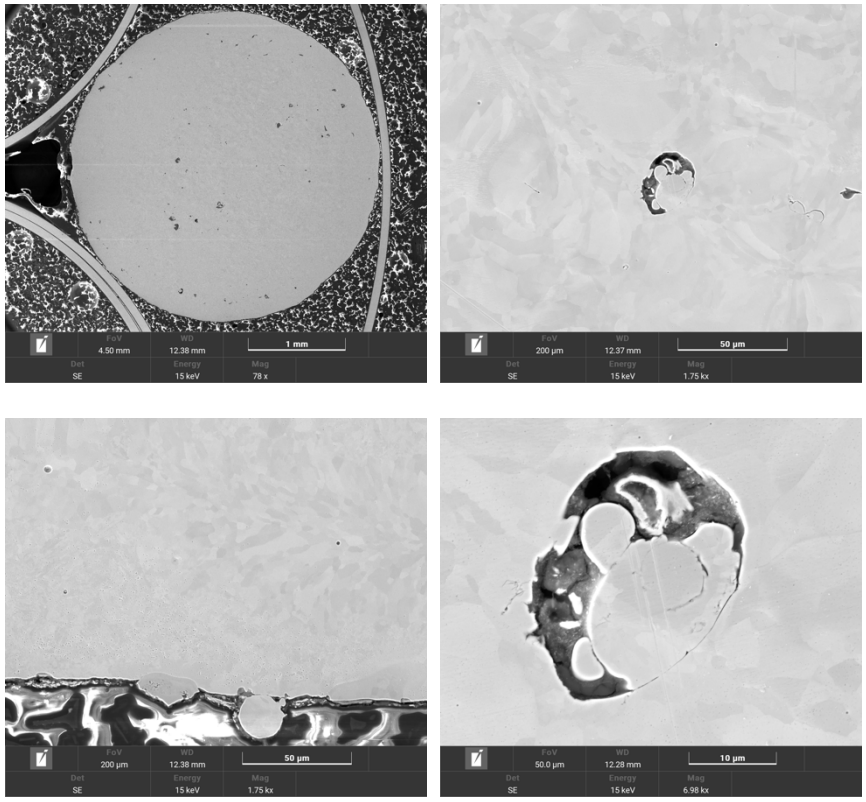

⊙ **BD**

Longitudinal cut of sample O: 200 W and 900 mm/s

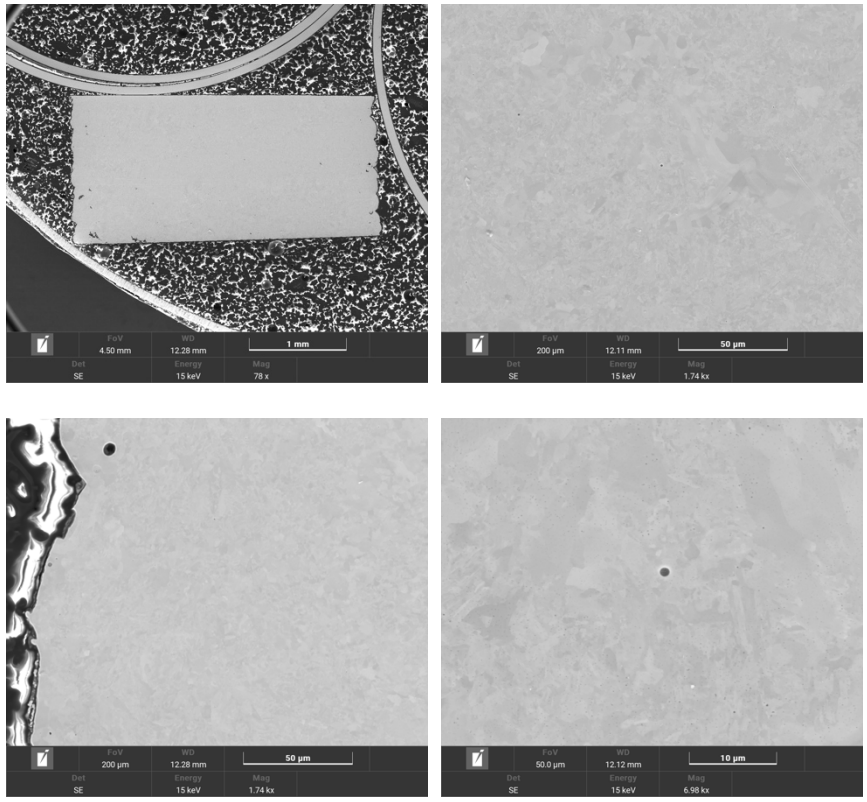

↑ **BD**

Top left: full cut sample; top right: zoomed-in view on center area;
bottom left: zoomed-in view on border area; bottom right: further zoomed-in view on center area.

Transversal cut of sample P: 200 W and 1000 mm/s

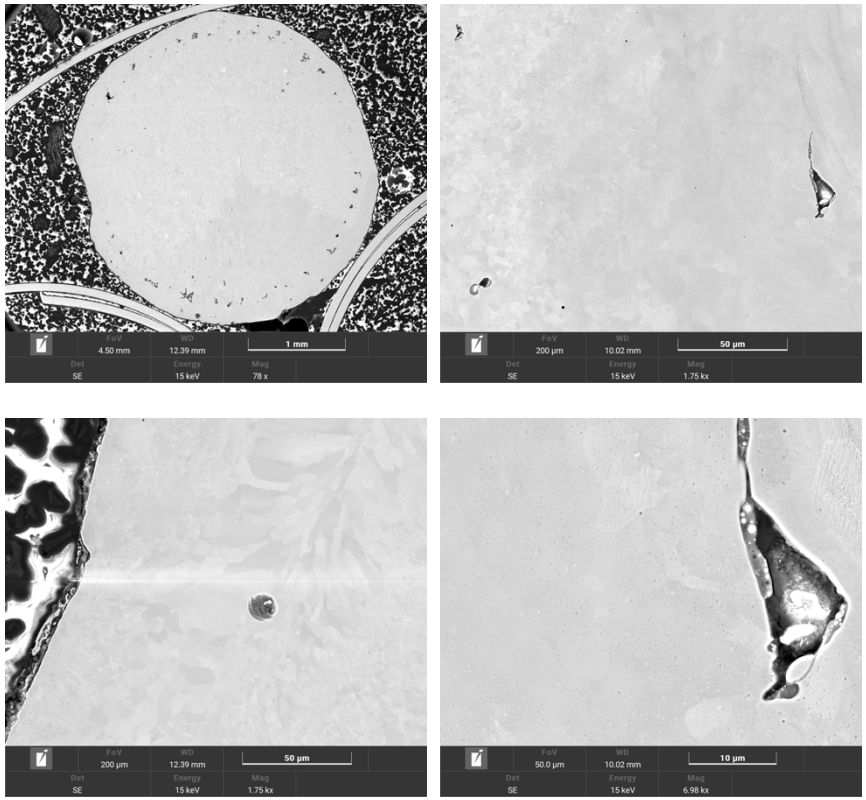

⊙ **BD**

Longitudinal cut of sample P: 200 W and 1000 mm/s

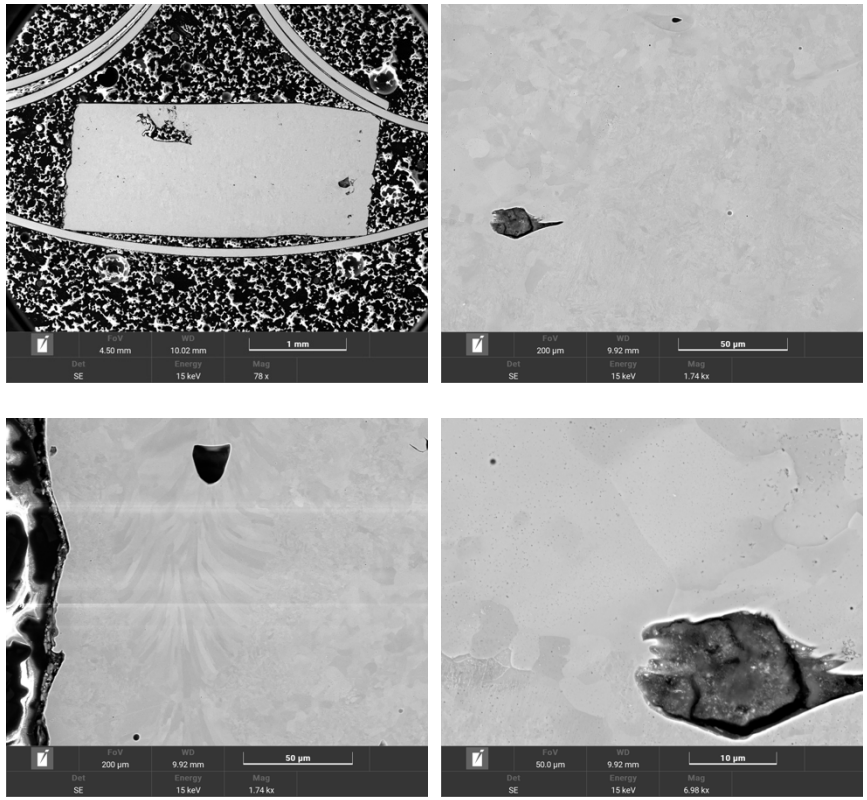

↑ **BD**

Top left: full cut sample; top right: zoomed-in view on center area;

bottom left: zoomed-in view on border area; bottom right: further zoomed-in view on center area.

9.3.2. FeSi3.5wt%

Transversal cut of sample J: 175 W and 800 mm/s

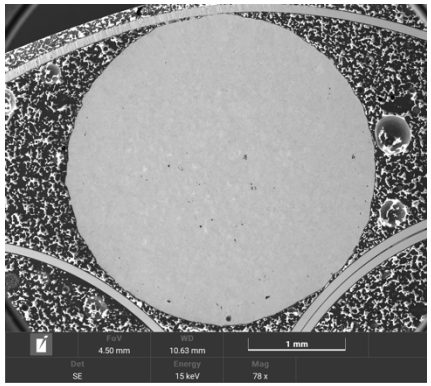

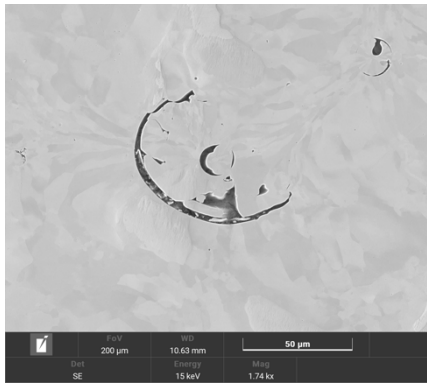

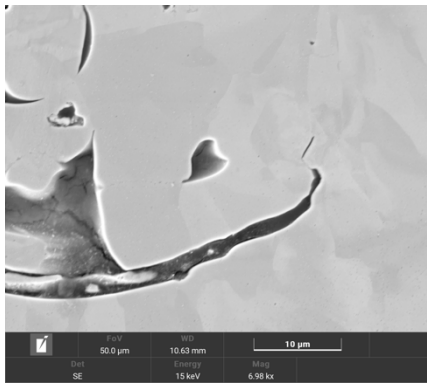

⊙ **BD**

Longitudinal cut of sample J: 175 W and 800 mm/s

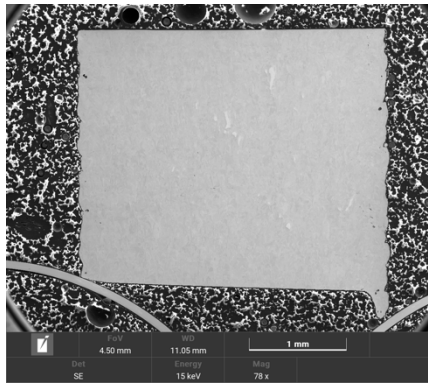

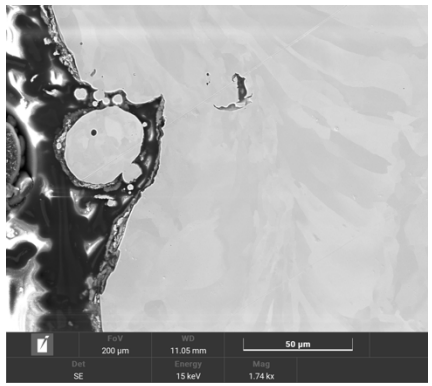

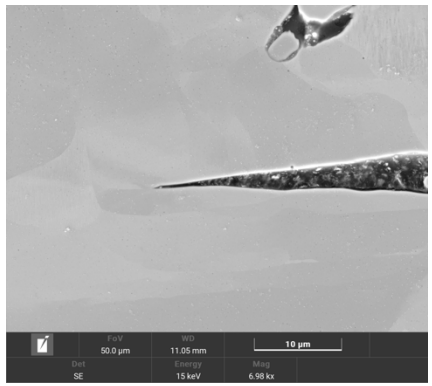

↑ **BD**

Top left: full cut sample; top right: zoomed-in view on center area;

bottom left: zoomed-in view on border area; bottom right: further zoomed-in view on center area.

Transversal cut of sample N: 200 W and 800 mm/s

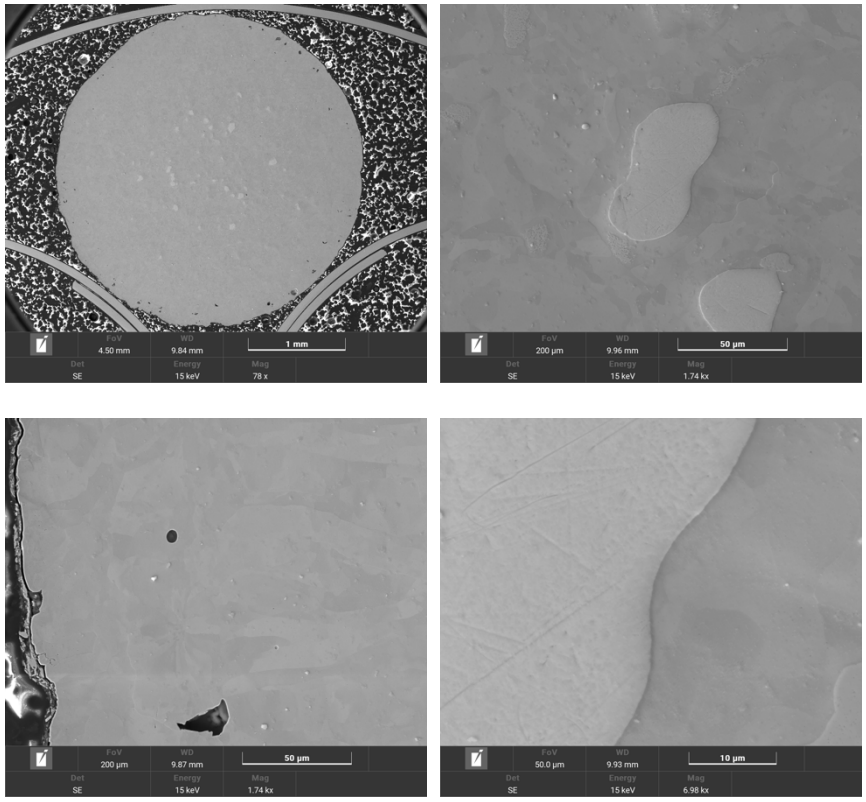

⊙ **BD**

Longitudinal cut of sample N: 200 W and 800 mm/s

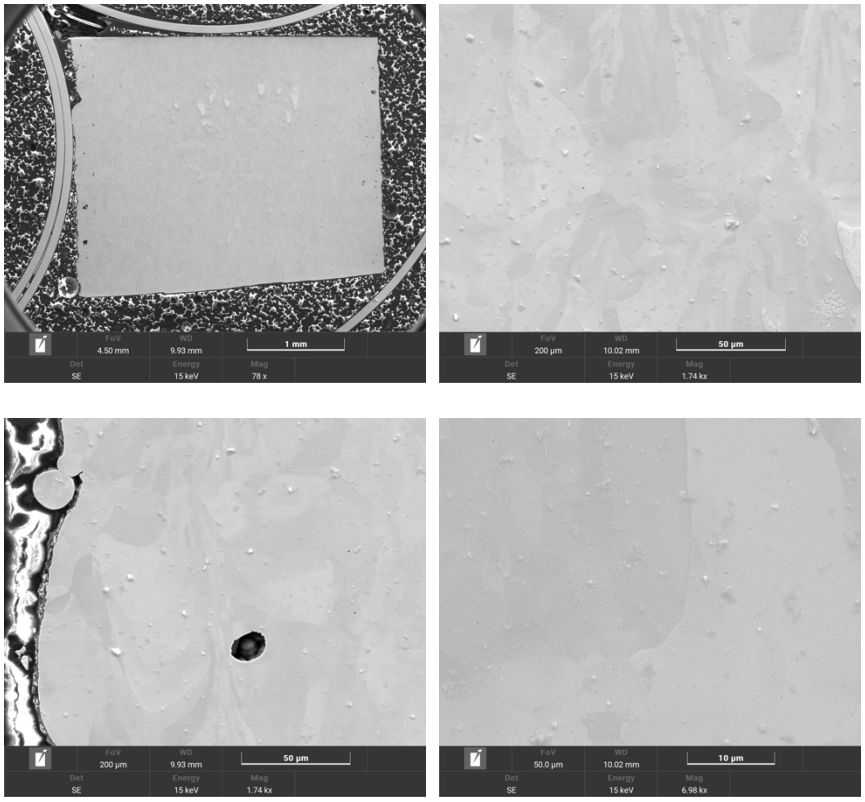

↑ **BD**

Top left: full cut sample; top right: zoomed-in view on center area;
bottom left: zoomed-in view on border area; bottom right: further zoomed-in view on center area.

Transversal cut of sample O: 200 W and 900 mm/s

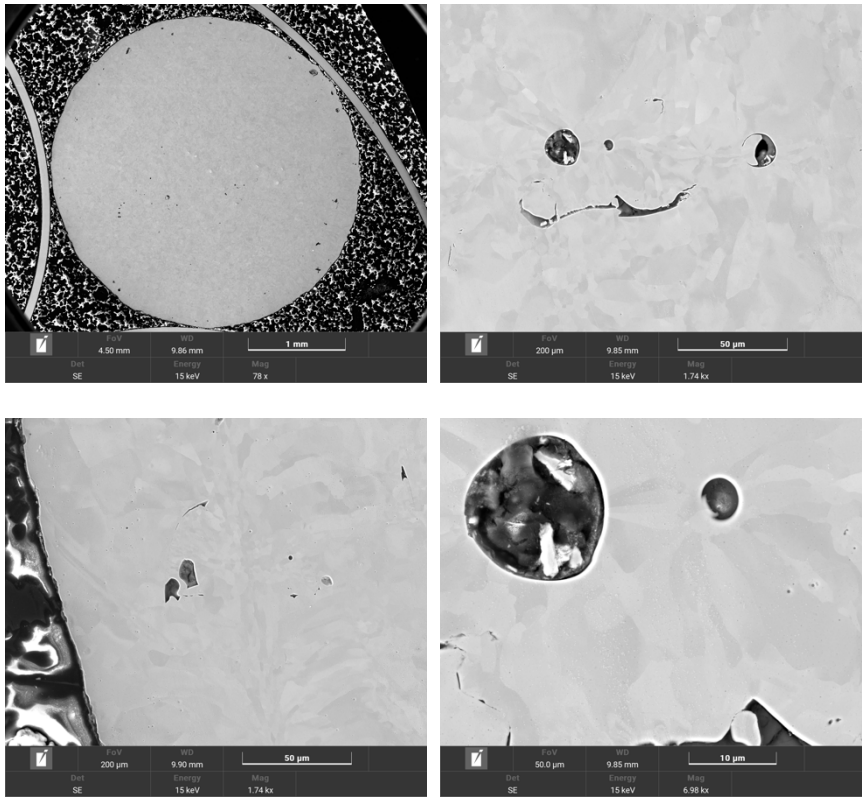

⊙ **BD**

Longitudinal cut of sample O: 200 W and 900 mm/s

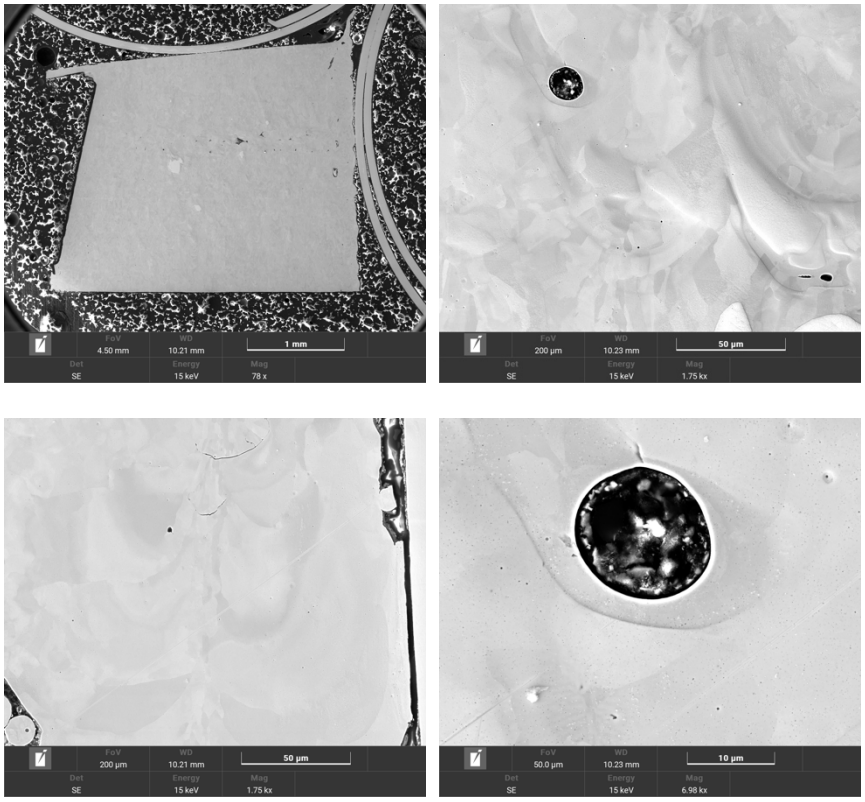

↑ **BD**

Top left: full cut sample; top right: zoomed-in view on center area;

bottom left: zoomed-in view on border area; bottom right: further zoomed-in view on center area.

Transversal cut of sample P: 200 W and 1000 mm/s

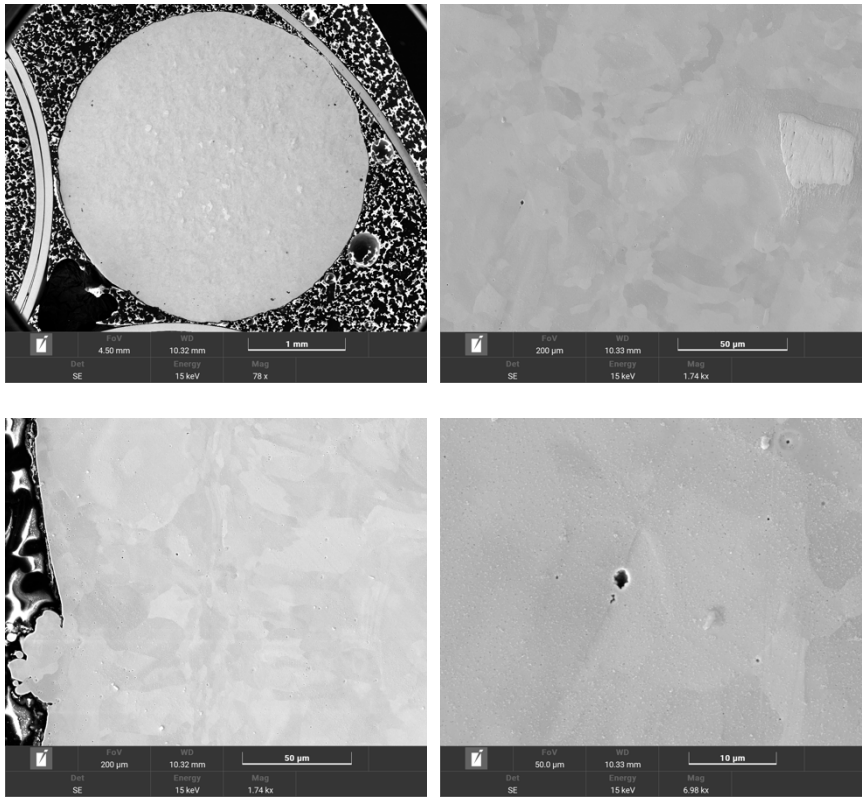

⊙ **BD**

Longitudinal cut of sample P: 200 W and 1000 mm/s

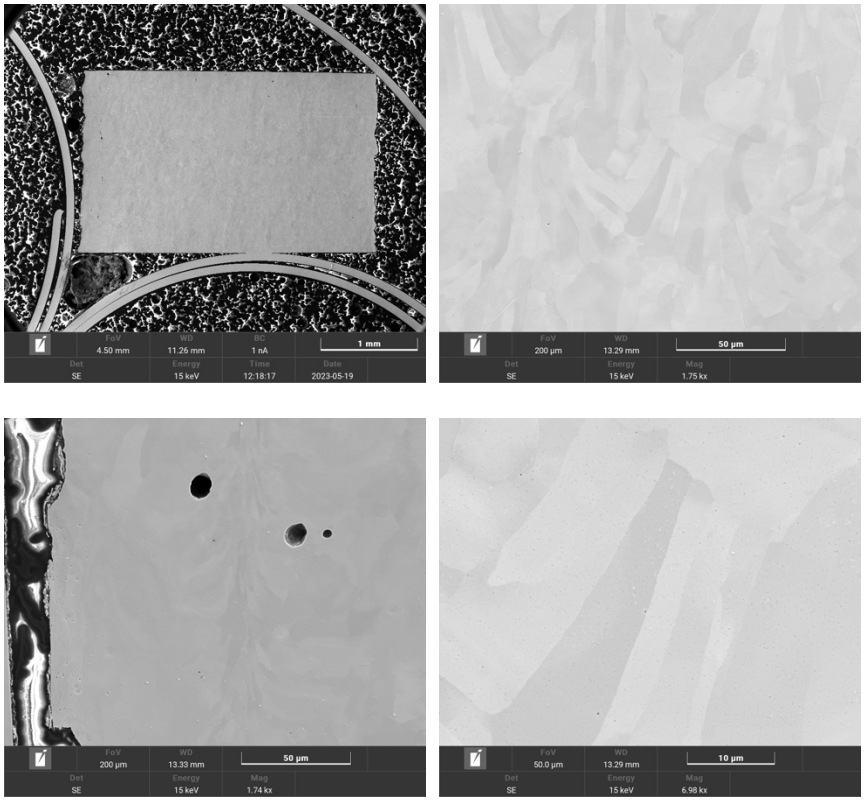

↑ **BD**

Top left: full cut sample; top right: zoomed-in view on center area;

bottom left: zoomed-in view on border area; bottom right: further zoomed-in view on center area.

9.4. Hardness Measurements

9.4.1. Python Script

Python scipt used for the data extraction. visualization and mean hardness calculation:

Code	Comments
from glob import glob import os import csv import matplotlib.pyplot as plt from matplotlib import cm import numpy as np	Package import
os.chdir('/Users/Robert/Documents/Folder/Document FOLDER = 'Foldername goes here' FILENAME = 'FileNameGoesHere.csv' DELIMITER = ';' PRINT_xLABEL = 'Measuring width [mm]' PRINT_yLABEL = 'Measuring depth [mm]' PRINT_zLABEL = 'Hardness (HV0.5)' os.chdir(FOLDER) OPEN_FILE = open(FILENAME. 'r') COLORCODE = 'viridis_r'	Opening the CSV file and defining further needed variables.
hardness = [] xAbsolute = [] xRelative = [] yAbsolute = [] yRelative = [] with open(FILENAME) as csvdatei: csv_reader_object = csv.reader(csvdatei. delimiter=DELIMITER) for row in csv_reader_object: H = row[4].replace('.'.'.') xAbs = row[8].replace('.'.'.') xRel = row[9].replace('.'.'.') yAbs = row[10].replace('.'.'.') yRel = row[11].replace('.'.'.') hardness.append(H)	Data extraction and sorting.

xAbsolute.append(xAbs) xRelative.append(xRel) yAbsolute.append(yAbs) yRelative.append(yRel) hardness.pop(0) hardness = np.array(hardness. dtype=float) xAbsolute.pop(0) xAbsolute = np.array(xAbsolute .dtype=float) xRelative.pop(0) xRelative = np.array(xRelative. dtype=float) yAbsolute.pop(0) yAbsolute = np.array(yAbsolute. dtype=float) yRelative.pop(0) yRelative = np.array(yRelative. dtype=float)	
AvgHardness = np.mean(hardness) AvgHardness_StdDev = np.std(hardness) xRelmin = np.min(xRelative) xRelative = xRelative – xRelmin x = xRelative y = yRelative z = hardness	Calculation of mean hardness and correct relative indent coordinates.
fig.ax = plt.subplots() ax.set_aspect('equal') tcf = ax.tricontourf(x. y. z. np.arange(100.325.25). cmap=COLORCODE) ax.set_xlabel(PRINT_xLABEL) ax.set_ylabel(PRINT_yLABEL) plt.rcParams['font.family'] = 'Helvetica Neue' fig.colorbar(tcf) plt.show()	Data visualization.
print('# Mean hardness: %.2f' % AvgHardness. '± %.2f' % AvgHardness_StdDev. '#\n\ # Maximum hardness: %.2f' % np.max(hardness). '#\n\ # Minimum hardness: %.2f' % np.min(hardness). '#\n\ # Number of test points: %.f' % len(x).')	Hardness values output.

9.5. Hysteresis Loops

9.5.1. FeSi3.5wt% sample N

Hysteresis loops for three individual hystography measurements.

Zoomed-in view on the left B-H-diagram's center part.

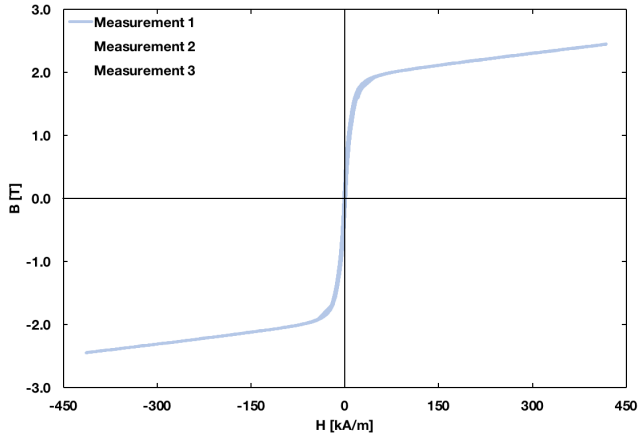

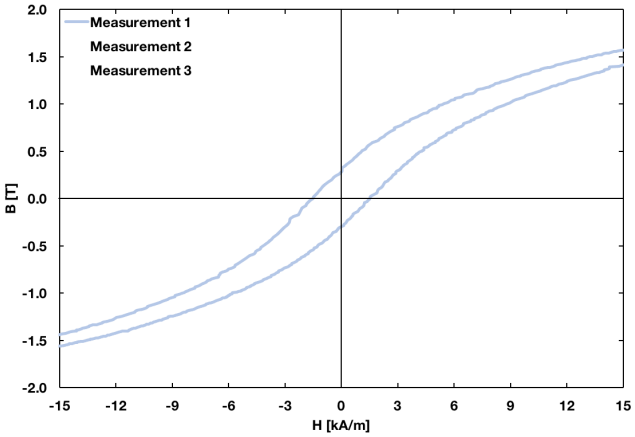

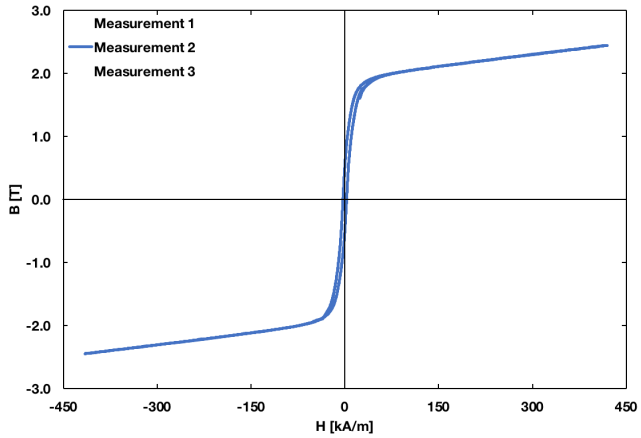

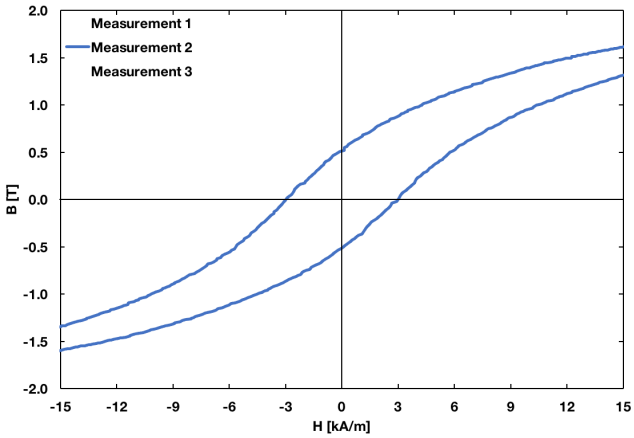

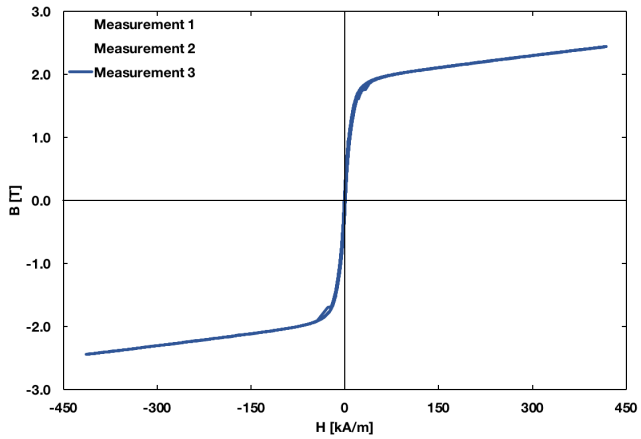

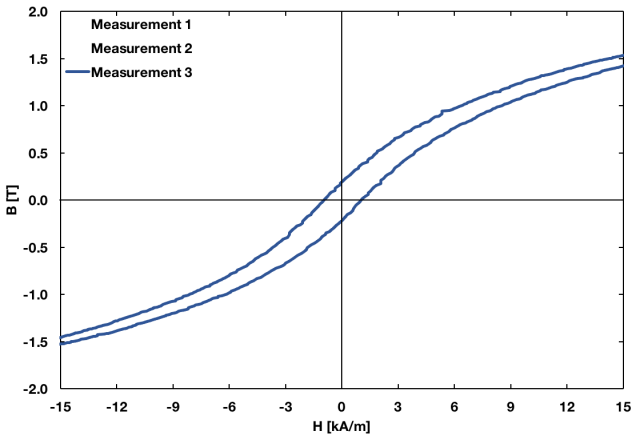

9.5.2. FeSi3.5wt% sample D

Hysteresis loops for three individual hystography measurements.

Zoomed-in view on the left B-H-diagram's center part.